Measurement of the Associated Production of a Z Boson with a J/psi Meson with the CMS Experiment at a Center-of-Mass Energy of 8 TeV

A THESIS
SUBMITTED TO THE FACULTY OF THE GRADUATE SCHOOL
OF THE UNIVERSITY OF MINNESOTA
BY

Jared Turkewitz

IN PARTIAL FULFILLMENT OF THE REQUIREMENTS
FOR THE DEGREE OF
DOCTORATE OF PHILOSOPHY

Yuichi Kubota

September, 2016

Acknowledgements

There are many people who I would like to thank for their help in finishing this thesis.

First and foremost, I would like to thank Yuichi Kubota, my adviser. Your physics intuition and advice were invaluable. Your compassion, support and guidance were essential to my successfully finishing this thesis.

Thanks to my parents, Hillary Turkewitz and Jonathan Ripley who raised me to be the man I am today. You both consistently led by example, and are truly kind-hearted people. Thanks to my brother, Josh Turkewitz, and my sister Rebecca Turkewitz for always supporting me.

Thanks to the University of Minnesota students, postdocs and professors who are or were part of the CMS collaboration, both past and present. Thanks to Seth Cooper for helping me get started as a graduate student. Thanks to Alexey Finkel and Joe Pastika for being good role models. Thanks to Alexander Gude who provided a solid analysis framework and is a nice person. Thanks to Zachary Lesko, lunch conversations with you were interesting. Thanks to Bryan Dahmes, Nicole Ruckstuhl and Giovanni Franzoni for their guidance and assistance. Thanks to Jeremiah Mans who is a truly brilliant and capable researcher. Thanks to Roger Rusack who gets things done. Thanks to Andrew Evans, Peter Hansen, Sean Kalufut, Tambe Norbert and Kelly Stifter.

Thanks to the graduate students at the University of Minnesota. Thanks to Tobias Gulden, Andy Julin, Mark Pepin, Tanner Prestegard, Dominick Rocco and everyone else who helped me on this journey.

Abstract

The associated production of a Z boson and a J/ψ meson provides information about the production mechanisms of quarkonium. A measurement of the associated production of a Z boson, which decays to leptons, and a J/ψ meson, which decays to muons, relative to the inclusive production of a Z boson, which decays to leptons, is presented. The measurement was made using the full 19.7 fb^{-1} of proton-proton collision data collected at a center-of-mass energy of $\sqrt{s} = 8\,\text{TeV}$ by the Compact Muon Solenoid detector at the Large Hadron Collider. The associated production is presented for both prompt and nonprompt J/ψ, as a function of the p_{T} of the J/ψ meson. The associated production cross sections of a Z (in $\mu^+\mu^-$ or e^+e^- decay modes) and a prompt or nonprompt J/ψ $\rightarrow\mu^+\mu^-$ relative to the inclusive production cross section of a Z (in $\mu^+\mu^-$ or e^+e^- decay modes) in the same fiducial volume is measured to be (41.5 $\pm$ 12.0 (stat) $\pm$ 1.8 (syst) $\pm$ 10.5 (pol)) $\times 10^{-7}$ and (93.0 $\pm$ 14.5 (stat) $\pm$ 2.5 (syst) $\pm$ 2.0 (pol)) $\times 10^{-7}$ respectively. The significance of observing associated production Z and prompt and nonprompt J/ψ meson was determined to be 3.8σ and 8.7σ respectively.

Contents

List of Tables

List of Figures

Chapter 1

Introduction

High energy particle physics offers a window into the smallest and most fundamental components of matter. The Large Hadron Collider (LHC) allows us to study high energy interactions at a higher rate than ever before. The huge amount of data produced provides a number of different channels from which we can attempt to search for new physics and precisely test the existing models.

This thesis probes the production mechanisms of quarkonium and heavy-flavor particles in association with a Z boson. The leptonic decays of the Z and the decay of the J/ψ to muons provide a clear signal which is relatively easy to distinguish from backgrounds. The clarity of the signal is important because the expected rate of production of this process is very low, even with the tremendous amount of interactions created by the LHC. The measurement is made for both prompt and nonprompt (from a b decay) J/ψ. This process also allows the study of multi-parton interactions.

The data used in this thesis were collected with the Compact Muon Solenoid (CMS) detector at a center-of-mass energy of 8 TeV. In total 19.7 fb^{-1} of integrated luminosity was recorded for proton-proton collisions.

The primary measurement made in this thesis is the probability of producing a prompt or nonprompt J/ψ $\rightarrow\mu^+\mu^-$ in association with a Z $\rightarrow\ell$ ℓ. This measurement is presented differentially in J/ψ transverse momentum. An additional overall ratio of associated production is also presented. The ratio is compared to theoretical predictions from different models of quarkonia production.

This thesis is organized as follows:

Chapter 2 presents the physics of the standard model and the motivation for the measurement.

Chapter 3 gives an overview of the LHC and CMS detector.

Chapter 4 explains the methods for selecting events and determining the efficiency of the selection criteria.

Chapter 5 presents the statistical techniques used to analyze events and determine the event yields from prompt and nonprompt J/ψ.

Chapter 6 presents how the backgrounds are determined for this measurement.

Chapter 7 discusses how systematic uncertainties are determined.

Chapter 8 presents the results for associated production of a Z and a J/ψ.

Chapter 9 presents conclusions and discusses interpretations of the results.

Chapter 2

Physics of Associated Production of the Z and the J/ψ

2.1 The Standard Model

The standard model (SM) of particle physics [25], describes our best current theoretical understanding of fundamental particles and their interactions, successfully predicting and explaining the results from experiments with diverse interactions at energies covering many orders of magnitude. For example, the SM successfully predicted the recent discovery of the Higgs Boson [26]. Furthermore, the SM correctly predicted the existence of the top quark [27], as well as the mass of the W and Z bosons [28]. In contrast, many theories that attempt to extend the SM make predictions that experimental results do not support [29]. However, the SM does not explain all observed experimental results. For example the SM assumes neutrinos to have zero mass, which is inconsistent with observed measurements of neutrino oscillations [30].

The SM classifies the fundamental particles by their spin and quantum numbers, as shown in Figure 2.1. Fermions, such as muons and electrons, obey the Pauli exclusion principle, while bosons can exist in the same state. In general, bosons mediate the interactions between fermions. At a low energy scale, there are four fundamental forces governing how particles interact: the strong force, the electromagnetic force, the weak force and gravity. The strong force is mediated by gluons, the weak force by the Z and W bosons, the electromagnetic force by photons and gravity is mediated by a

hypothetical particle known as the graviton. The relative strengths of these forces depend on the distance scale at which the interaction occurs and the energy-dependent coupling constants of the forces. Many theorists have posited that there exists a certain energy scale for which the four fundamental forces can be unified and described by one single force. However, SM predictions do not fully unify all of the forces. Theories that go beyond the standard model, such as Supersymmetry (SUSY), may be able to unify the fundamental forces, which is one of the reasons SUSY is a popular theory to explain physics that the SM does not. There are many detailed descriptions of the SM, for example: [31], [26], [32] and [33].

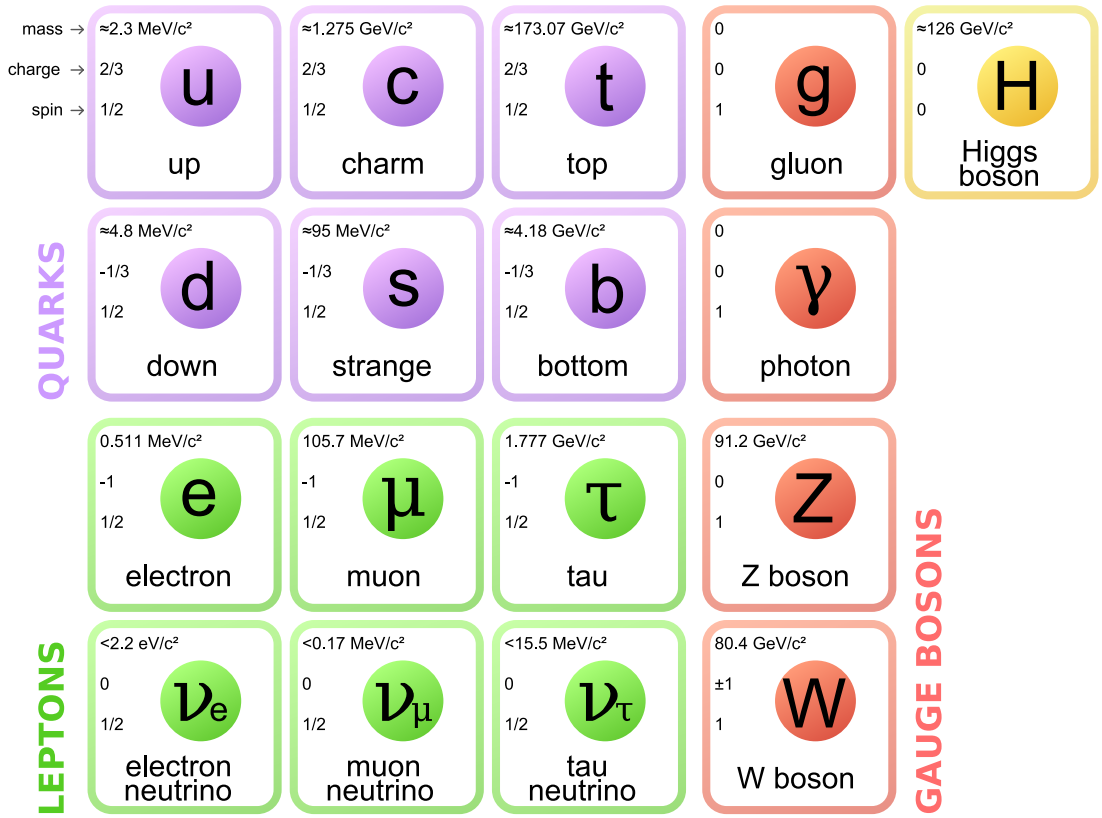

Figure 2.1: The fundamental particles of the SM.

2.2 Quantum Chromodynamics

Quantum chromodynamics (QCD) is the theory of strong interactions. QCD is a very complicated theory, and has been described in detail, for instance: [34], [35] and [36]. Following [36]: QCD is based on the gauge group $SU(3)$. One possible representation of the 8 independent generating matrices is the Gell-Mann matrices, shown in Fig. 2.2. The gauge transformation carried out by the gluons can be represented by the generating matrices. Analogous to electric charge, quarks and gluons have a property known as color charge. By convention these three options are named for the classic additive primary colors: red, blue, and green. Gluons are in color-octet states, e.g. $\frac{1}{\sqrt{2}}\left(\left|r\bar{b}\right\rangle + \left|b\bar{r}\right\rangle\right)$, while quarks are in color-triplet states, e.g. $|r\rangle$, and hadrons are in color-singlet states, e.g. $\frac{1}{\sqrt{3}}\left(\left|r\bar{r}\right\rangle + \left|g\bar{g}\right\rangle + \left|b\bar{b}\right\rangle\right)$. Neither quarks or gluons have been observed as free particles, but rather have always been observed confined in hadronic bound states. There is no analytical proof as to why QCD must have confinement, but current theories hypothesize confinement is due to the color charge of the gluon. The Lagrangian of QCD is:

$$\mathcal{L} = \bar{\psi}_q^i (i\gamma^\mu)(D_\mu)_{ij}\psi_q^j - m_q\bar{\psi}_q^i\psi_{qi} - \frac{1}{4}F_{\mu\nu}^a F^{a\mu\nu} \tag{2.1}$$

where ψ_q^i is a quark field with color index i, γ^μ is a Dirac matrix, m_q is the quark mass, $F_{\mu\nu}^a$ is the gluon field strength tensor for a gluon with color index a, and D_μ is the covariant derivative in QCD:

$$(D_\mu)_{ij} = \delta_{ij}\partial_\mu - ig_s t_{ij}^a A_\mu^a \ , \tag{2.2}$$

where g_s is the strong coupling, defined by $g_s^2 = 4\pi\alpha_s$ where α_s is the strong coupling constant, A_μ^a the gluon field with color index a and $t_{ij}^a = \frac{1}{2}\lambda_{ij}^a$ where λ^a is the Gell-Mann matrices.

To first approximation, the coupling constant α_s does not depend strongly on energy, for many energy scales. At the energy scale $Q^2 = M_Z^2$ where M_Z is the mass of the Z boson, the coupling constant is given by:

$$\alpha_s(Q^2) = \alpha_s(M_Z^2)\frac{1}{1 + b_0\alpha_s(M_Z^2)\ln\frac{Q^2}{M_Z^2} + \mathcal{O}(\alpha_s^2)} \ , \tag{2.3}$$

$$\lambda_1 = \begin{pmatrix} 0 & 1 & 0 \\ 1 & 0 & 0 \\ 0 & 0 & 0 \end{pmatrix},\ \lambda_2 = \begin{pmatrix} 0 & -i & 0 \\ i & 0 & 0 \\ 0 & 0 & 0 \end{pmatrix},\ \lambda_3 = \begin{pmatrix} 1 & 0 & 0 \\ 0 & -1 & 0 \\ 0 & 0 & 0 \end{pmatrix}$$

$$\lambda_4 = \begin{pmatrix} 0 & 0 & 1 \\ 0 & 0 & 0 \\ 1 & 0 & 0 \end{pmatrix},\ \lambda_5 = \begin{pmatrix} 0 & 0 & -i \\ 0 & 0 & 0 \\ i & 0 & 0 \end{pmatrix},\ \lambda_6 = \begin{pmatrix} 0 & 0 & 0 \\ 0 & 0 & 1 \\ 0 & 1 & 0 \end{pmatrix}$$

$$\lambda_7 = \begin{pmatrix} 0 & 0 & 0 \\ 0 & 0 & -i \\ 0 & i & 0 \end{pmatrix},\ \lambda_8 = \frac{1}{\sqrt{3}} \begin{pmatrix} 1 & 0 & 0 \\ 0 & 1 & 0 \\ 0 & 0 & -2 \end{pmatrix}$$

Figure 2.2: The Gell-Mann matrices. There are 8 independent gluon colors, described by $g_i = \begin{pmatrix} r & b & g \end{pmatrix} \lambda_i \begin{pmatrix} \bar{r} \\ \bar{b} \\ \bar{g} \end{pmatrix}$.

where $\mathcal{O}(\alpha_s^2)$ terms are available at [37], and b_0 is the first coefficient of the beta function:

$$\beta(\alpha_s) = \frac{\partial \alpha_s}{\partial \ln Q^2} = -\alpha_s^2(b_0 + b_1\alpha_s + b_2\alpha_s^2 + \ldots) \ , \tag{2.4}$$

where $\beta(\alpha_s)$ is the function driving the energy dependence or running of the coupling constant. As the energy increases, α_s decreases, known as asymptotic freedom. This implies that at higher energy scales perturbation theory is better behaved. Additionally, it suggests that at some energy scale α_s will become comparable to the coupling constants of the weak and electromagnetic force, which increase with energy. In contrast as energy decreases α_s increases:

$$\alpha_s(Q^2) = \frac{1}{b_0 \ln \frac{Q^2}{\Lambda^2}} \ , \tag{2.5}$$

where

$$\Lambda \sim 200\,\mathrm{MeV} \tag{2.6}$$

specifies the energy scale at which the perturbative coupling would become infinite. The distribution of α_s with energy scale is shown in Fig. 2.3. This implies that perturbative techniques are not applicable at low energy scales, and nonperturbative methods such as lattice QCD are needed [38]. To model nonperturbative processes we factorize these processes into process-independent nonperturbative factors and into perturbative

process-dependent factors. The nonperturbative factors must be determined experimentally, while the perturbative processes can be calculated theoretically [39]. In essence, the predictions of QCD are tested by utilizing global experimental results for low energy nonperturbative processes, and combining this with perturbative calculations done at high energy, for which α_s is small so the perturbative expansion is valid [40]. Predictions are then made through $\sigma_1 = a_{nonpert} * b1_{pert}$ and $\sigma_2 = a_{nonpert} * b2_{pert}$, such that $\frac{\sigma_1}{\sigma_2} = \frac{b1_{pert}}{b2_{pert}}$.

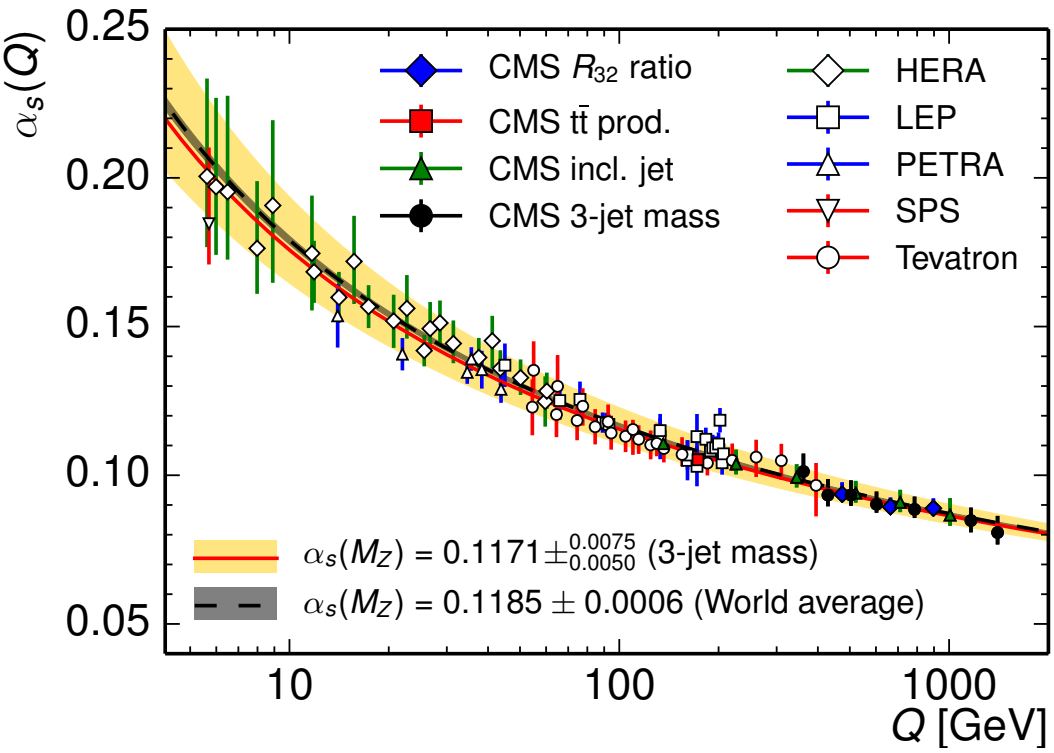

Figure 2.3: The running of α_s with energy scale Q as determined by [41]. The strength of the coupling constant decreases as the energy scale increases.

2.2.1 J/ψ

The discovery of the J/ψ sparked a revolution in particle physics. The November Revolution, named because the discovery of the J/ψ was announced on 11 November 1974,

showed a new method to understand the structure of matter, that all hadrons were composite particles made of quarks. The J/ψ, which has a particle content of $c\bar{c}$, has mass of 3.1 GeV, width of 92.9 keV, and decays to two muons 5.93% of the time [42]. The narrow width indicated the J/ψ contained a new flavor of quark which is conserved by the strong interaction. The charm quark was predicted to exist by Glashow, Iliopoulos and Maiani in order to explain the experimentally observed small decay rate of $K^0 \to \mu^+\mu^-$ via the Glashow-Ilopoulos-Maiani (GIM) mechanism. The GIM mechanism requires that there is a weak-isospin doublet partner to the strange quark, the charm quark. The discovery of the J/ψ helped confirm the existence of the charm quark.

The J/ψ is an important particle for exploring new physics, as it is experimentally easy to distinguish muons from other particles because muons have the distinctive property of being minimum ionizing particles (MIPs). Due to its low mass and narrow resonance, it is extensively studied with leptonic colliders. Measurements of J/ψ produced in association with other particles are not always well explained theoretically [8]. The high luminosity and energy of the LHC enables us to probe a hadronic channel of J/ψ production from leptonic colliders.

2.2.2 Color Models

The production of J/ψ was originally thought to be governed by the color-singlet model (CSM). The CSM describes the production and decay of quarkonium (a meson made up of a $q\bar{q}$ pair) with the correct spin, angular-momentum, color, and charge-conjugation quantum numbers. This production was factorized into a short distance part calculated in a perturbative series based on the strong coupling constant, and a long distance part which relied on the nonperturbative dynamics of the bound state [4]. The CSM describes perturbative creation of quarkonium that is on-shell, in a color-singlet state, and has a vanishing relative momentum. The J/ψ, is in color-singlet $^3S_1$ state. The nonperturbative binding of quarks is described by the Schrödinger wave function. In the CSM, the production rate is related to the magnitude of the color-singlet wave function and its derivatives evaluated at zero $q\bar{q}$ separation. Once these quantities are determined with measured quarkonium decay rates there are no free parameters in the CSM [8]. Recent studies have found that at high energies large corrections to the CSM appear at NLO and NNLO in α_s, suggesting, with a large theoretical uncertainty, that the CSM

could describe experimental data at these energies. Prior to these recent studies LO CSM underestimated cross sections at high energies. But there are some theoretical problems with the CSM: the magnitude of these corrections calls into question whether the series converges. Another theoretical challenge with the CSM is the presence of uncancelled infrared divergences in the production and decay of P-wave and higher orbital angular momentum quarkonium states [43].

When the cross section of J/ψ production was originally measured with a $p\bar{p}$ collider by the CDF collaboration, the cross section was much higher than originally predicted by the CSM at LO, especially at high p_{T}. The $\psi(2S)$ cross section was about a factor of 50 higher than predicted by LO CSM [8]. Additionally, $d\sigma/dp_{\mathrm{T}}$ was not described well by the CSM at LO, as shown by Fig. 2.4 and Fig. 2.5. Recently there has been discussion that the CSM predictions at NLO may describe the experimental results better [44].

Another theory of quarkonia production is the color-evaporation model (CEM). In the CEM, the appearance of color-singlet states depends only on the outcome of large-distance fluctuations of quarks and gluons [9]. The color-singlet state of the quarkonia is initially ignored in the CEM; in other words, the state can be produced by LO $q\bar{q}$-annihilation into $c\bar{c}$, equivalent to the Drell-Yan process. In the CEM, p_{T} distributions for all charmonium family members are identical, which implies that the production ratios should be independent of energy and p_{T} (up to a scale factor). The CEM claims that the ratios of quarkonium cross sections remain constant as a function of kinematics. The production cross section for quarkonia, with the process shown in Fig. 2.6, in the CEM is given by:

$$\sigma_{\mathrm{onium}} = \frac{1}{9}\int_{2m_c}^{2m_D} dm\ \frac{d\sigma_{c\bar{c}}}{dm}\ , \tag{2.7}$$

where the cross-section for producing quarkonia, $\sigma_{c\bar{c}}$ is calculated perturbatively [8]. The factor of $\frac{1}{9}$ arises due to the statistical probability that the charm pair is in a singlet state, with $\frac{8}{9}$ in an octet state [9]. In the CEM these states are treated equivalently; in the CSM only the color singlet state is relevant while in the color octet model discussed subsequently the color octet states and color singlet states contribute to the cross section at different rates. The CEM fit to experimental results from CDF for the cross section of J/ψ and $\psi(2S)$ has a χ^2 per degree of freedom between 2 and 4.5, which is not in good agreement with the data [8]. Another example of a prediction of CEM that is

not consistent with experimental results is the prediction that the inclusive production rates for quarkonium states should be process independent. This is inconsistent with experimental data that suggests the fraction of J/ψ indirectly produced from decays of χ_{c1} and χ_{c2} differs significantly between B decays and prompt production [45]. However, the CEM may not be applicable when the total hadronic energy is not sufficiently large [45].

While recently there has been discussion that higher order CSM could explain these discrepancies, many theorists advocate for a more nuanced theory of non-relativistic QCD (NRQCD) known as the color-octet model (COM). In the COM the quarkonia state can evolve into a J/ψ through emission of soft particles at later time scales. This evolution is shown in Fig. 2.7. Similar to the CSM, the COM relies on non-relativistic QCD (NRQCD) factorization into perturbative and nonperturbative regimes. Unlike in the CSM, the quarkonia state produced can have quantum numbers different from those of the physical quantum state. Feynman diagrams for the CSM and COM are shown in Fig. 2.8. The quarkonia would later radiate soft gluons to evolve into the quarkonia state with the correct quantum numbers. This means that a single gluon could form a quarkonia state. This process of radiation is governed by long distance matrix elements (LDME), which are process independent and are measured empirically. However, the LDME arise from nonperturbative QCD, and thus cannot be calculated theoretically. The COM can only increase the cross sections as predicted by the CSM, and at low orders in the velocity of the quarkonia, the COM reduces to the CSM. The cross section in the COM to produce a quarkonium state H is given by:

$$\sigma(H) = \sum_n \sigma_n(\Lambda)\langle \mathcal{O}_n^H(\Lambda)\rangle \,. \tag{2.8}$$

where Λ is the ultraviolet cutoff of the effective theory, the σ_n are expansions in powers of velocity v of the cross section to produce a quarkonia with the proper quantum numbers. The matrix elements $\langle \mathcal{O}_n^H(\Lambda)\rangle$ are vacuum-expectation values of operators in NRQCD. Because Eq. 2.8 can be ordered as an expansion in v, the NRQCD factorization is an expansion in powers of v and α_s. If the sum is truncated at LO in v for each quarkonium state, then the NRQCD reduces to the CSM. The Feynman diagrams with associated orders are shown in Fig. 2.9 [8].

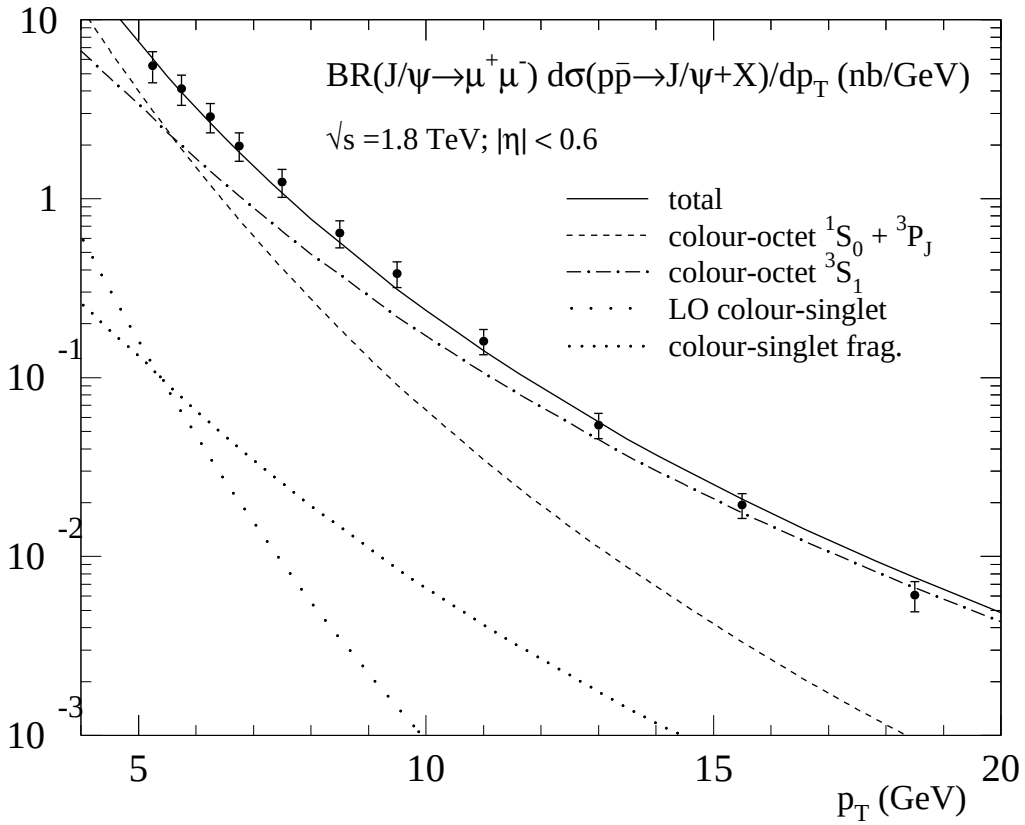

Figure 2.4: CSM LO prediction does not describe well $d\sigma(p\bar{p} \to \mathrm{J}/\psi + X)/dp_{\mathrm{T}}$, the differential cross-section of the J/ψ as a function of p_{T} produced at the Tevatron when compared to the COM [7].

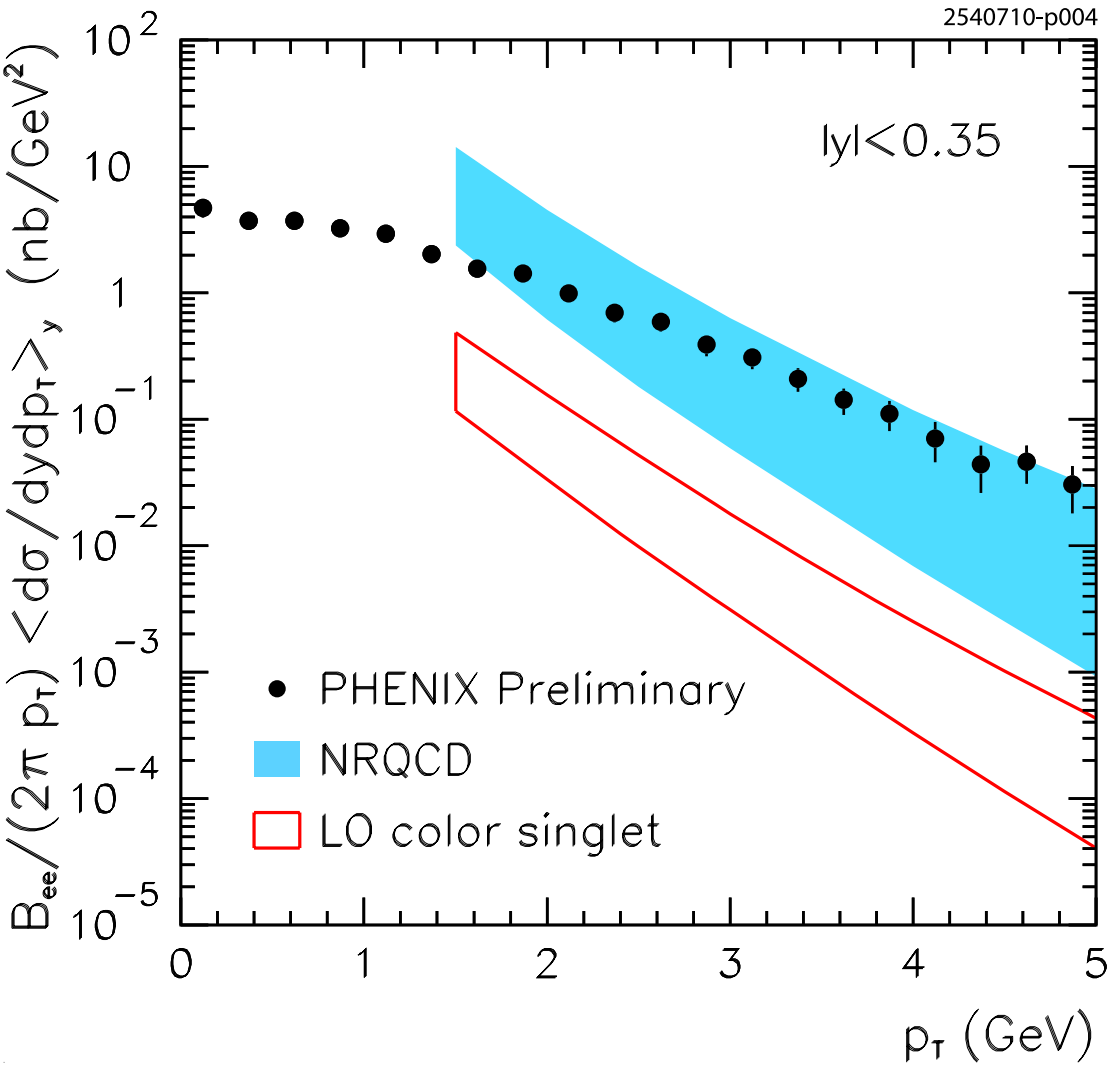

Figure 2.5: CSM LO prediction does not describe the p_{T} distribution of the J/ψ as shown from data from the PHENIX experiment at the Relativistic Heavy Ion Collider. NRQCD is an acronym for non-relativistic QCD and a synonym for the COM [8].

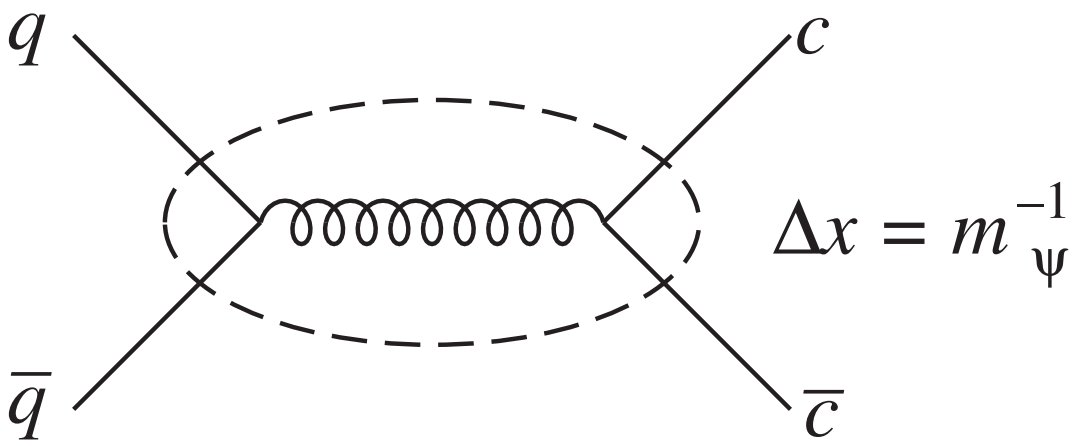

Figure 2.6: CEM Feynman diagram, calculated perturbatively with its dynamics determined by short-distance interactions of range $\Delta x = m_{\psi}^{-1}$. The color singlet property of the $c\bar{c}$ state is not enforced at short distances in the CEM because there is an infinite time for soft gluons to readjust the color of the $c\bar{c}$ pair before it forms into a quarkonium state [9].

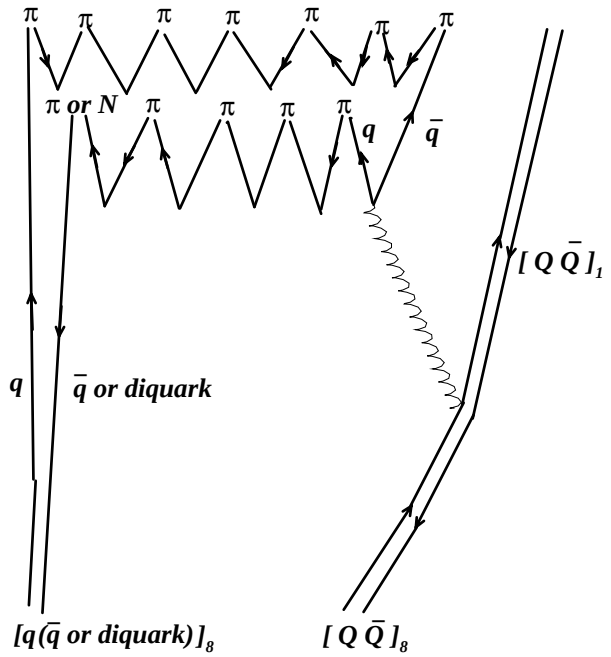

Figure 2.7: Schematic picture to show the evolution of a bound color-octet $[Q\bar{Q}]_8$ evolves into a color-singlet state. The emission of a soft gluon converts the color-octet state into a color-singlet state [10].

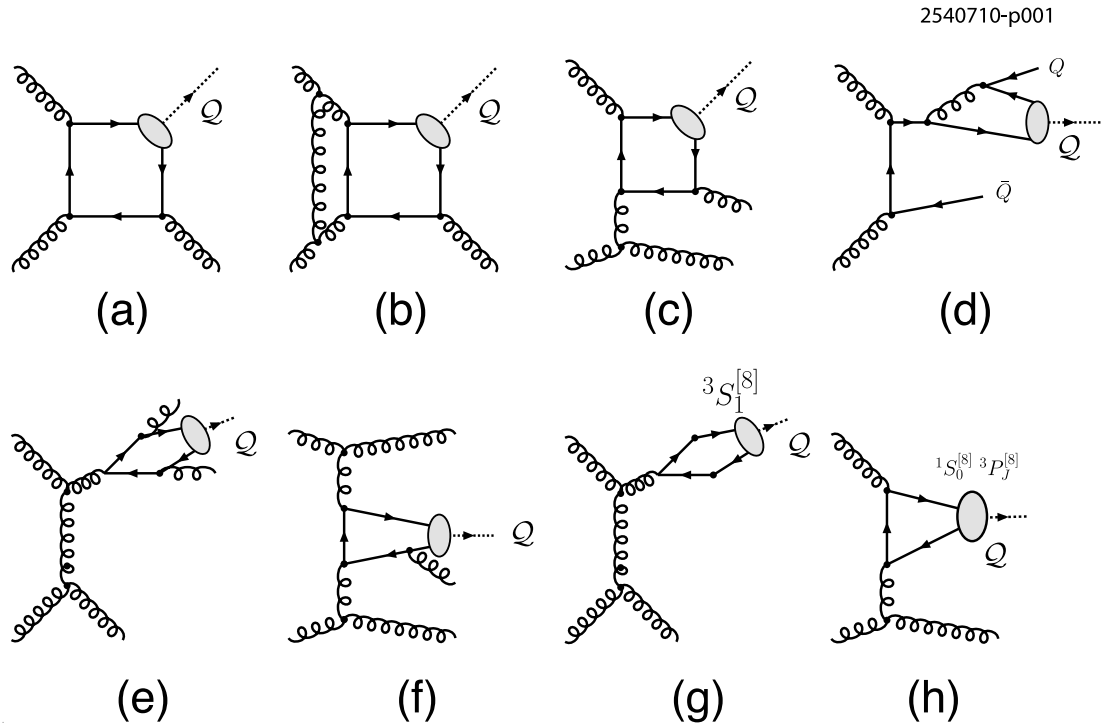

Figure 2.8: Feynman diagrams for production of a quarkonium state through a collision of two gluons. The diagrams a-f represent the leading order CSM, while g-h represent the COM [8].

(a) leading-order colour-singlet:
$g + g \to c\bar{c}[^3S_1^{(1)}] + g$

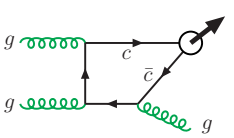

$+\ldots \quad \sim \alpha_s^3 \frac{(2m_c)^4}{p_t^8}$

(b) colour-singlet fragmentation:
$g + g \to [c\bar{c}[^3S_1^{(1)}] + gg] + g$

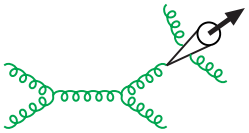

$+\ldots \quad \sim \alpha_s^5 \frac{1}{p_t^4}$

(c) colour-octet fragmentation:
$g + g \to c\bar{c}[^3S_1^{(8)}] + g$

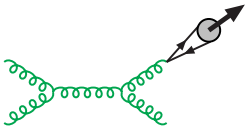

$+\ldots \quad \sim \alpha_s^3 \frac{1}{p_t^4} v^4$

(d) colour-octet fusion:
$g + g \to c\bar{c}[^1S_0^{(8)}, {}^3P_J^{(8)}] + g$

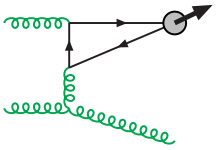

$+\ldots \quad \sim \alpha_s^3 \frac{(2m_c)^2}{p_t^6} v^4$

Figure 2.9: Feynman diagrams with associated orders in the strong coupling constant α_s included [7].

The COM is able to explain the unexpectedly large cross-section for J/ψ production at CDF. However, the COM has had difficulties explaining some experimental results. The polarization predicted by the COM is not in agreement with experimental measurements made by the CDF collaboration, as shown in Fig. 2.10. When the momentum of the gluon producing the quarkonia is large, the gluon is nearly on-shell and should have transverse polarization. Then, because of NRQCD spin symmetry, the quarkonia state would have the same polarization as the gluon. However, experimental observations of produced quarkonia have unpolarized quarkonia. This puzzle is known as the quarkonia polarization puzzle [8].

Studying the associated production cross section for a Z boson and a J/ψ could shed light on the COM and NRQCD factorization. The COM is expected to contribute significantly to this process, as shown by Fig. 2.11 and Fig. 2.12. This process could also provide additional information about the true universality of LDME; in other words, it could demonstrate whether or not the non-perturbative calculations apply similarly to disparate processes. The measurement of this process could illuminate how important higher order corrections are. Also, an anomalously large cross section could be seen as a potential sign of new physics, like a fermiophobic Higgs decaying to a J/ψ [13].

Associated production of a Z and a J/ψ can provide an experimentally unambiguous signal for high energy QCD because of the leptonic decays of the Z and J/ψ and the high mass of the Z [4, 46]. The interaction scale for this process is near to the mass of the Z boson. High p_{T} physics is important to study because the predicted p_{T} distribution differs based on the CSM or the COM approach. The theoretical calculations needed to predict this process are quite complicated, and there are different theoretical predictions about the cross section of this process [4, 13, 46]. While NRQCD is generally considered more accurate than CSM, these models rely on assumptions about the universality of LDME to estimate nonperturbative contributions to this process. For example, the ATLAS collaboration measured a similar process of associated production of a W boson and a J/ψ [47] and found a cross section that was in disagreement with the predictions of the theory, although revisions of the theories may explain this discrepancy [44].

This process is important because it can provide information about QCD for a high energy process. Many processes need to be measured in order to verify the factorization approach to QCD. There is not a clear theoretical consensus on the importance

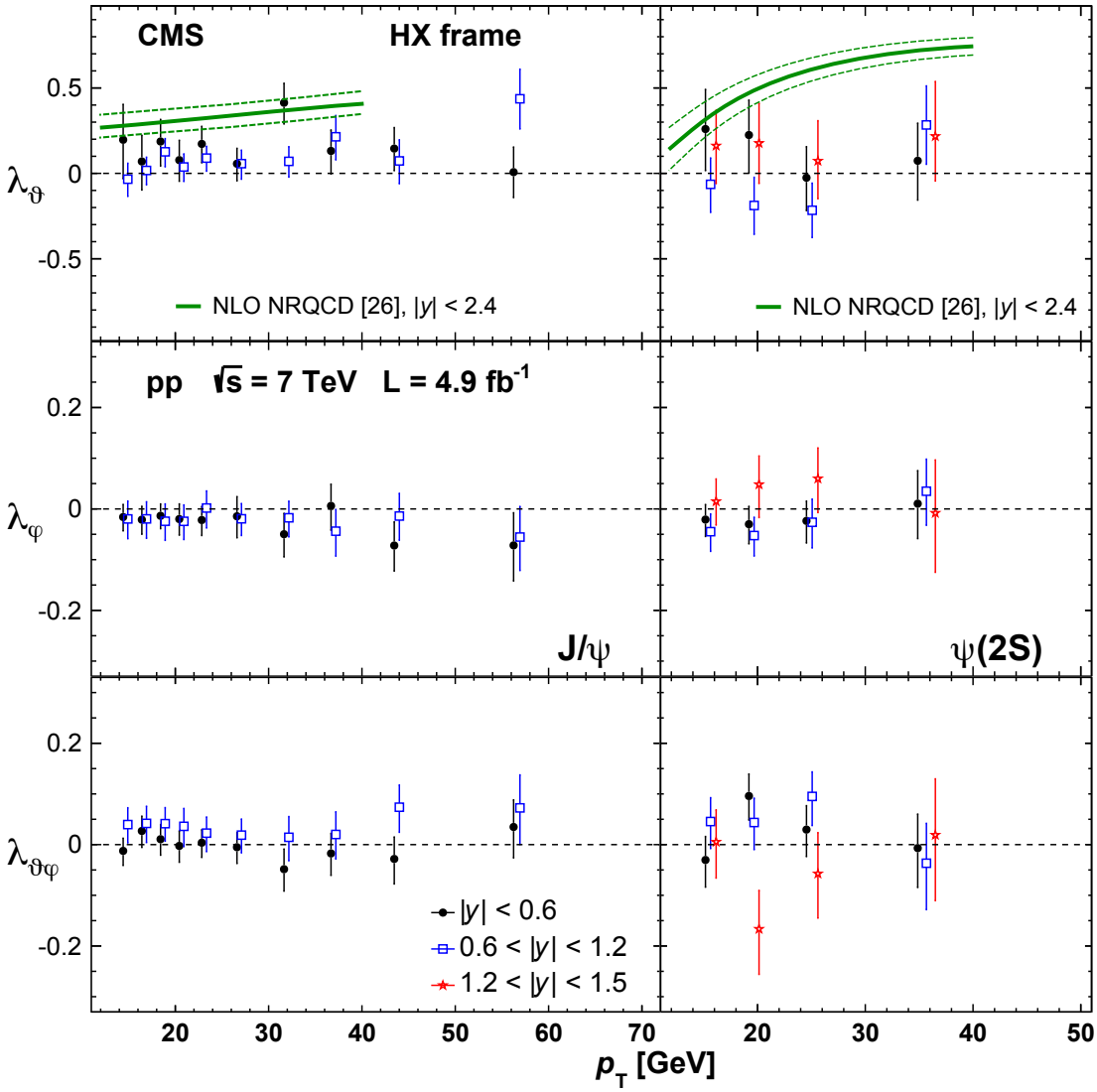

Figure 2.10: The COM [11] does not well explain observed polarization of the J/ψ and $\psi(2S)$ measured by CMS at high p_{T} [12].

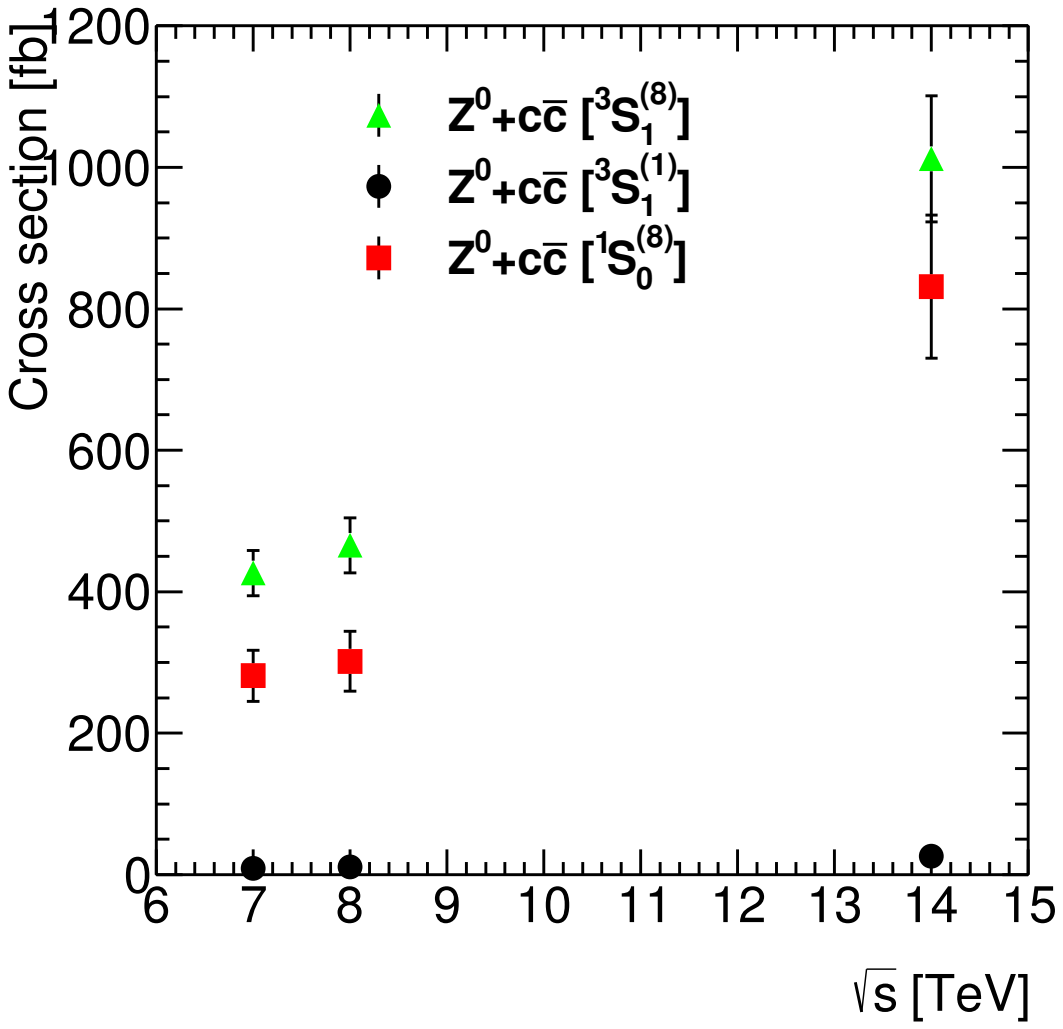

Figure 2.11: Prediction of $Z + \mathrm{J}/\psi$ at the LHC as a function of center-of-mass energy, $\sqrt{s}$. The cross-section is roughly proportional to the center-of-mass energy. The COM is expected to contribute significantly to this process at leading-order [13].

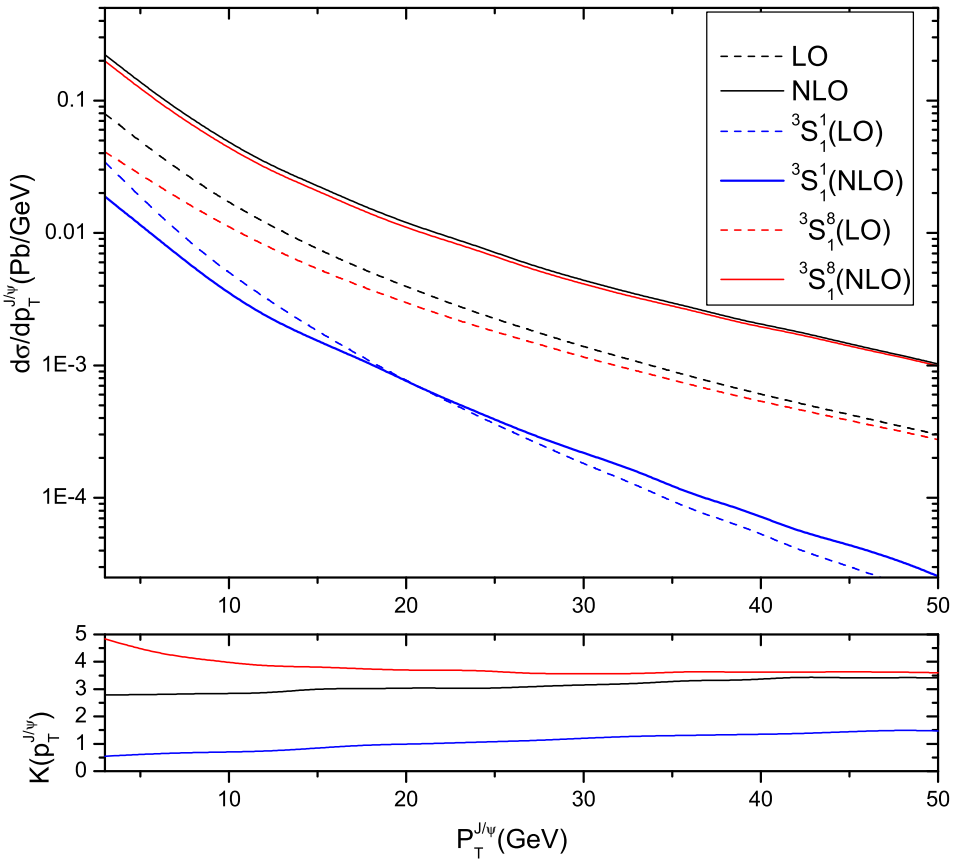

Figure 2.12: Theoretical prediction of associated production of a Z and a J/ψ at the LHC at a center-of-mass energy of 14 TeV. The COM is expected to contribute significantly this process at NLO [4].

of color-octet and of higher order corrections for this process. Additionally, an exceptionally large or small cross section could be a sign of new physics. A measurement in good agreement with theory could provide information about how well this process is understood, giving a glimpse into the complicated world of NRQCD. There is a long history of the J/ψ particle resulting in revised notions of physics.

Chapter 3

The CMS Experiment

3.1 The Large Hadron Collider

The LHC is a proton-proton collider that encircles the border between France and Switzerland. It is the highest energy particle collider ever constructed, with a center-of-mass energy of 8 TeV in 2012 and of 13 TeV in 2015. It is located in a tunnel between 100 and 150 meters underground. The tunnel has a circumference of 27 km and a cross-sectional diameter of 4 meters. The circumference of the tunnel is important because it allows a greater beam energy for a given magnet strength as the radius of curvature is larger. The LHC collides protons at four interaction points, with a detector built to study the results of the collisions at each of these points. There are two general purpose detectors; CMS and ATLAS, designed to explore and study a wide range of high energy physics. There are two more specialized detectors: LHCb is designed primarily to study b quark physics, and ALICE is designed to study heavy-ion collisions which occur for a short period each year instead of pp collisions.

There are many technical challenges that complicate the task of accelerating protons to such a high energy. For example, more powerful magnets are needed to keep the beams circulating as the energy of the protons increases. Additionally, charged particles continually radiate energy as they are accelerated, so this energy must continually be returned to the protons. Furthermore, powerful magnets are needed to keep the protons circulating in the beam path. The LHC is designed to overcome these complications by accelerating the protons through a series of steps, as shown in Fig. 3.1. The protons

originate in a container of hydrogen gas; an electric field strips the electrons from the hydrogen. Then Linac 2 is used to accelerate the protons to an energy of 50 MeV. This beam is then injected into the Proton Synchrotron Booster (PSB) which accelerates the protons to 1.4 GeV. Next is the Proton Synchrotron (PS), which accelerates the beam to 25 GeV. Protons are then sent to the Super Proton Synchrotron (SPS) which accelerates the protons to 450 GeV. Only then are the protons brought into the beam pipes of the LHC, circulating in opposite directions around the tunnel. The protons then reached an energy of 4 TeV in 2012 and 6.5 TeV in 2015 while circulating in the LHC tunnel [48]. Because the LHC is a circular collider where both protons are accelerated to equal energies, in opposite directions, the center-of-mass energy of the collision is the sum of the energy of the protons.

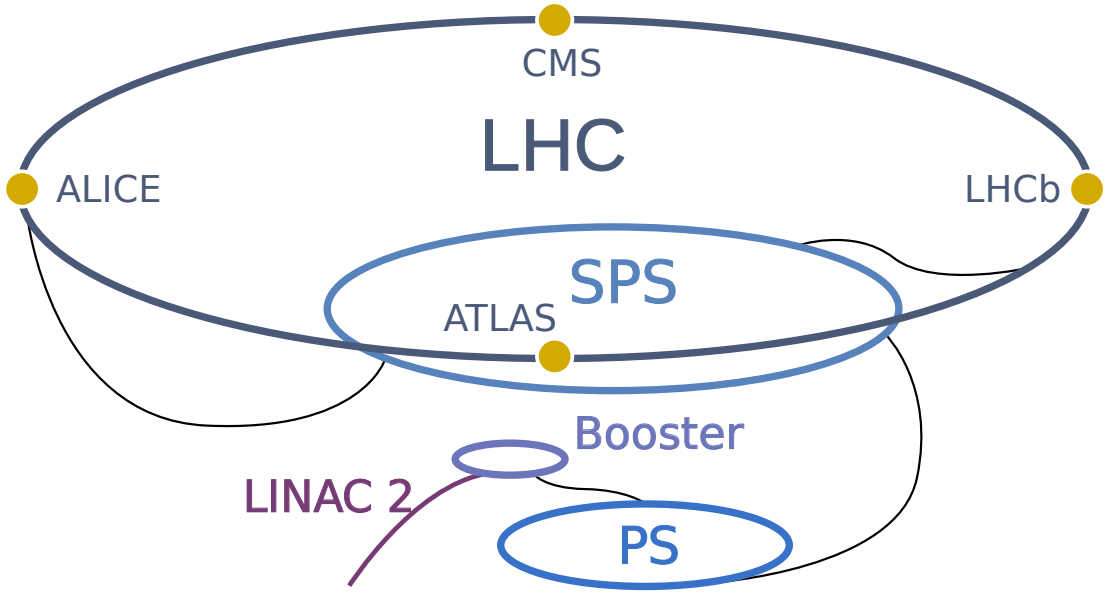

Figure 3.1: A schematic showing the facilities used to accelerate protons at the LHC. Also shown are the locations of the detectors at the four interaction points at which the protons collide. Adapted from [14].

The LHC uses almost 1232 dipole magnets to keep the protons circulating at a high energy in the beam pipes. The magnetic field of these magnets peaks at 8.3T at nominal energy, which requires superconducting magnets. Additionally, there are 392

quadrupole magnets which focus the beams at the 4 interaction points, and ensure the protons do not leave the beam pipes around the circumference. There are 8 RF cavities per beam to accelerate the protons to 4 TeV and to counter-balance energy losses due to radiation. Finally, any collisions with dust or other objects in the beam pipe must be avoided. To minimize these collisions the LHC beam pipes maintain a vacuum more pure than the atmosphere on the moon.

3.2 The CMS Detector

The CMS detector is one of the two general-purpose detectors at the LHC; for an in-depth reference check [49]. The CMS detector was designed to find and measure the properties of the Higgs boson, search for particles predicted by theories beyond the SM, and to expand and refine the SM. A global collaboration of approximately 4300 active physicists and engineers collects and analyzes data with the CMS detector. The CMS detector is composed of a number of subdetectors as shown in Fig. 3.2. These subdetectors will be described in detail in the following sections.

The CMS detector distinguishes between different particles primarily by determining the particle's charge, momentum, energy and rate of energy lost as the particle passes through matter. The charge and momentum of the particle are determined by measuring its trajectory through a strong magnetic field of 3.8 T. For uncharged particles, the track is determined by where in the detector the energy is deposited. The energy of the particle is determined by measuring the amount of energy it deposits as it transverses through matter in the calorimeters. Muons are the only type of charged particle that is likely to reach the muon chambers. Muons are distinguished by their property of minimizing ionizing particles (MIPs), which means the amount of energy they deposit is almost independent of the muon's energy, for muons with sufficient energy. Fig. 3.3 shows typical trajectories of different types of particles through a transverse slice of the CMS detector. It is important to have wide coverage in order to measure if an event has missing transverse energy (MET) carried out by particles which have a small probability of interacting with matter, such as neutrinos or dark matter candidates.

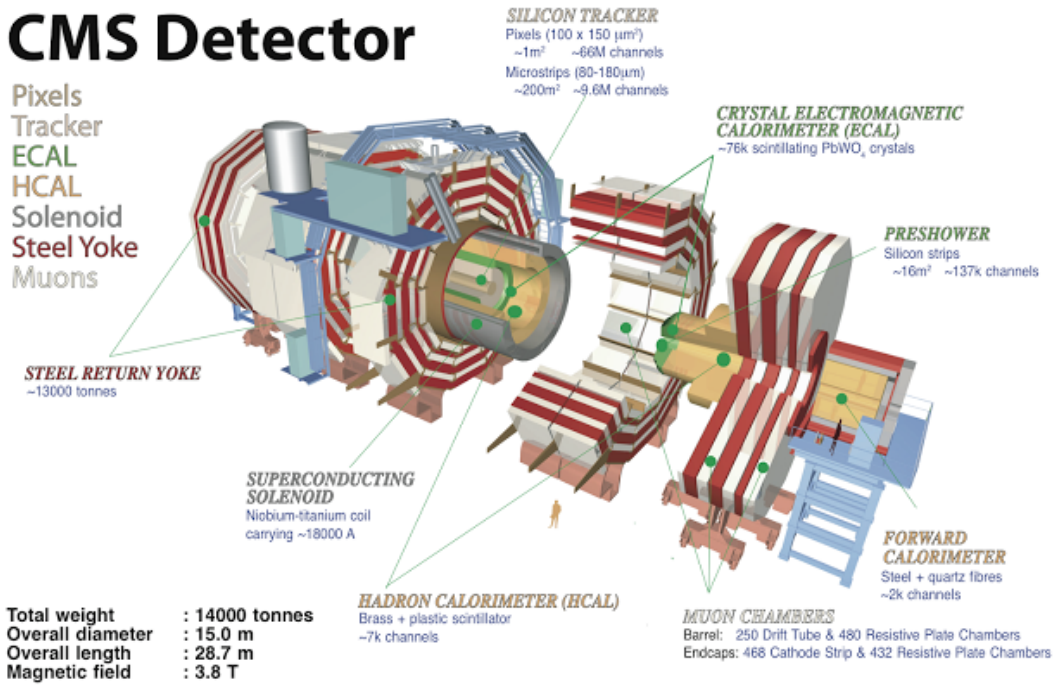

Figure 3.2: A cut-out view of the CMS detector showing the subdetector components. Each subdetector provides information about the momentum and energy of the particles produced in the LHC collision.

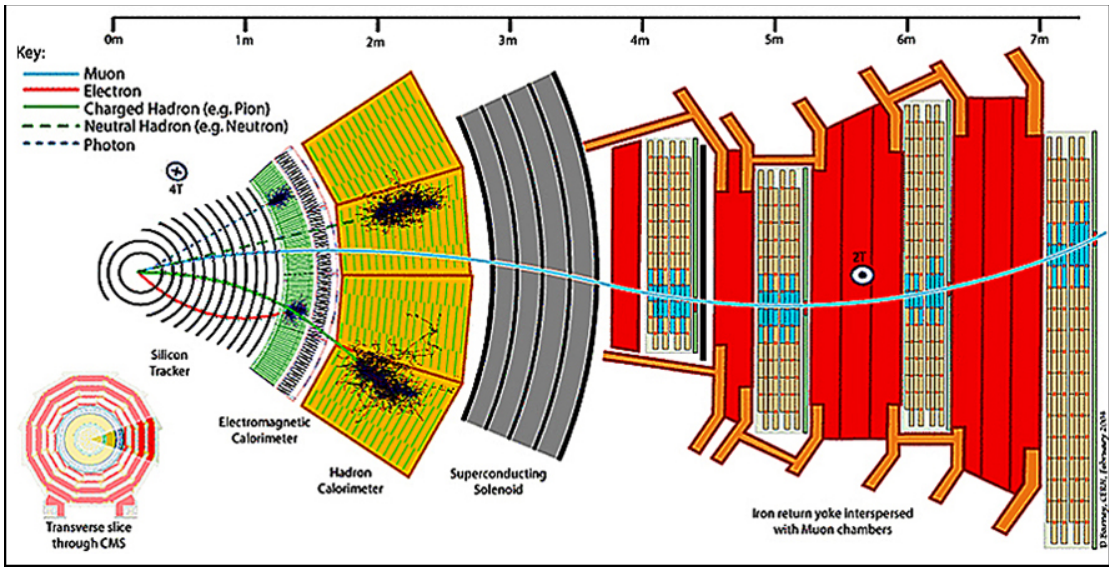

Figure 3.3: A transverse slice of the CMS detector. This diagram shows different possible trajectories common SM particles take as they pass through the CMS detector.

3.2.1 The Tracker

The tracker is the subdetector closest to the Interaction Point (IP), the point at which the protons collide. The tracker measures the trajectory of charged particles as they pass through a magnetic field, allowing us to determine the particle's momentum. The tracker is made up of silicon, a semiconductor which is dense enough to provide good resolution, while also being resistant to radiation damage. The tracker is divided into an inner tracker which is composed of about 66 million pixels and an outer tracker which is composed of about 10 million strips. The pixels have a better resolution than the strips because the strips are 100 μm by 150 μm while the strips are either 10 cm by 180 μm or 25 cm x 180 μm. Both the inner and the outer tracker are made entirely of silicon. The vertex position resolution is 10 (30) μm in the transverse (longitudinal) impact parameters [50]. The Tracker is particularly important for the analysis of associated production of Z bosons and J/ψ because of its ability to distinguish between different vertices in the same event. This is useful both in distinguishing prompt from nonprompt J/ψ and also in determining if the Z and J/ψ come from the same vertex. In addition, the tracker is instrumental in reconstructing the J/$\psi \rightarrow \mu^+\mu^-$ [49].

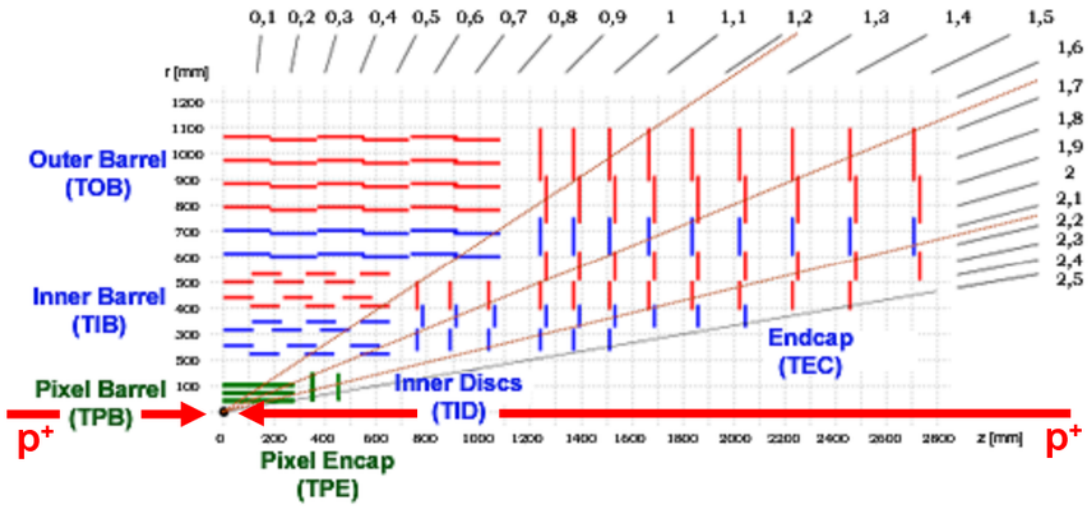

Figure 3.4: The CMS tracker is made of silicon as the active material. The innermost layer consists of 66 million 100 μm $\times$ 150 μm pixels. The next four layers are made of 10 cm $\times$ 180 μm silicon strips, followed by six layers of 25 cm $\times$ 180 μm strips. In total there are 9.6 million strip channels. Charge sharing calculations allow the resolution of the tracker to be better than the size of the individual components, as additional information is gained from the ratio of the charge deposited in adjacent channels.

3.2.2 The Electromagnetic Calorimeter

The electromagnetic calorimeter (ECAL), shown in Fig. 3.5 is the second inner-most subdetector [51]. The ECAL is designed to measure the energy and position of electromagnetic particles, specifically photons and electrons. ECAL is made up of almost 76,000 lead tungstate crystals, in order to be radiation hard and to have good energy resolution. Electrons and photons will deposit the majority of their energy into the ECAL. The ECAL barrel (EB) uses avalanche photo-diodes (APDs) to detect the scintillation light of the crystals. Scintillation light is emitted as the transparent crystals are exposed to radiation. The ECAL Endcap (EE) electronics use vacuum photo-triodes (VPTs). The ECAL is particularly useful for the Z + J/ψ analysis for detecting the $Z \rightarrow e^+e^-$ decay. The di-electron mass spectrum is shown in Fig. 3.6. The energy resolution of ECAL for electrons from decays of the Z is better than 2% in the central region of EB and varies between 2% and 5% elsewhere [15]. Because the ECAL needs to convert an electronic response to an energy measurement, calibration is essential for the ECAL. The absolute calibration was determined by exposure to high-energy electron beams prior to installation in CMS. After installation, the $Z \rightarrow e^+e^-$ decay is used to validate the energy correction for electrons by using the Z mass constraint [51]. Additionally, the response changes as a function of radiation damage to the crystals, so changes in the response need to be continuously monitored. The ECAL monitoring and calibration are accomplished primarily with a 440 nm blue laser which emits light near the peak of the scintillation light wavelength; and, a red laser at 800 nm provides information about the stability of the system and is useful for systematic cross-checks. This response is continually monitored because it changes over time due to radiation exposure and recovery as shown in Fig. 3.7.

While the primary purpose of the ECAL is to measure the energy and position of electromagnetic showers, it also measures the time it takes the particle to reach ECAL after the proton-proton collision. The timing information is important in some searches for new physics and also to distinguish anomalous energy deposits, known as spikes [52], from interesting physics events. Spikes arise when neutrons or other slow moving hadrons directly impact the EB APDs, creating signals similar to those created by very high energy particles. These spikes are caused by direct ionization of the silicon. These particles have a different pulse shape than scintillation light produced in the crystals, so

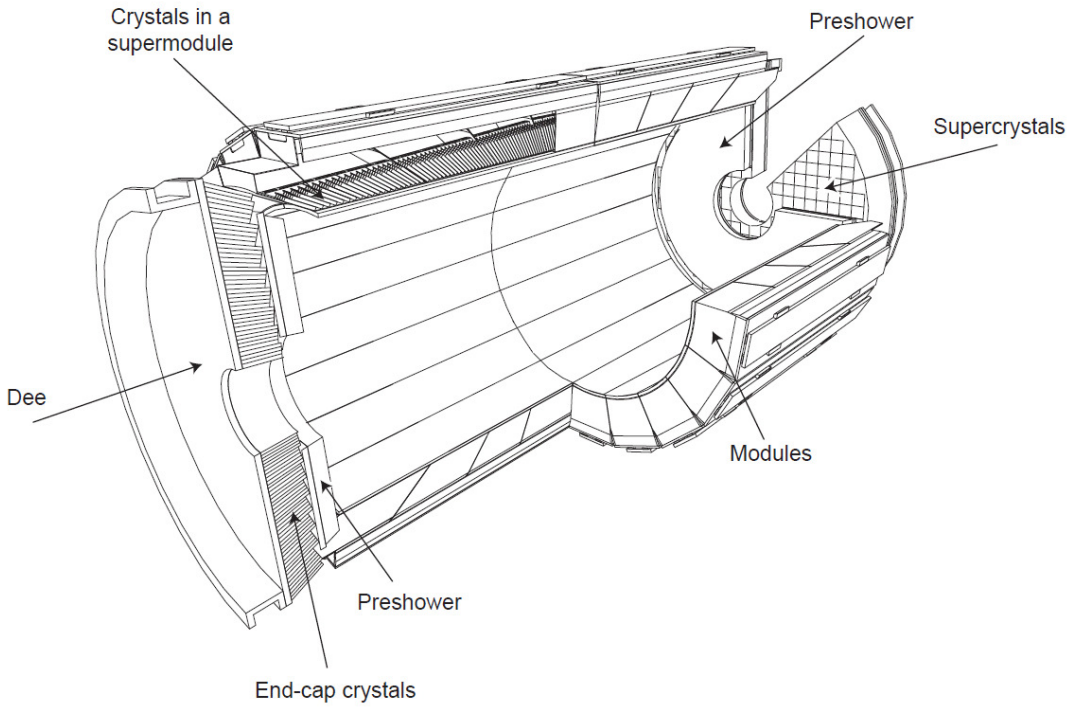

Figure 3.5: Schematic showing a quarter slice of the ECAL [15]. The ECAL measures the energy of electromagnetic particles such as electrons and photons, which deposit the majority if not all of their energy in the ECAL.

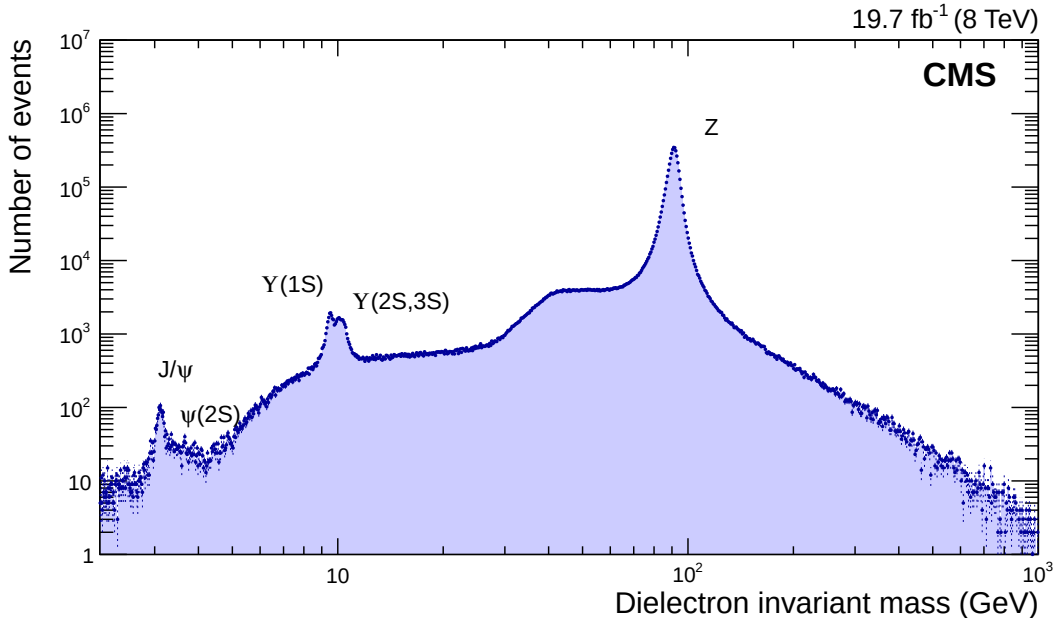

Figure 3.6: The di-electron mass spectrum with all di-electron triggers [16].

timing is helpful in discriminating against them, as shown in Fig. 3.8 and Fig. 3.9. The Minnesota group is responsible for monitoring and recalibrating the time calibration of each ECAL crystal to ensure that all crystals would read out the same value if the time the particle took to reach the crystal was the same. The process to do this involved determining the average time for each of the 75848 crystals and adding a constant to center the average at zero. This means that even if hardware changes affect the time of the crystals relative to the reference time, the timing measurement is such that a time reading of zero corresponds to the arrival of the proton beam collisions. I was responsible for this process during the 2011 and 2012 runs.

The timing of the ECAL is determined by the shape of its pulse, shown in Fig. 3.10. The time of the hit is determined by the shape of this pulse; however, due to radiation effects this shape can change. Because the ECAL is continuously being exposed to radiation, this means that it is necessary to continually monitor the timing, as shown in Fig. 3.11. Additionally, hardware changes could cause the ECAL timing to become unaligned. Calibrating the ECAL timing can adjust for these problems, such that there is a common reference point to compare different events equivalently.

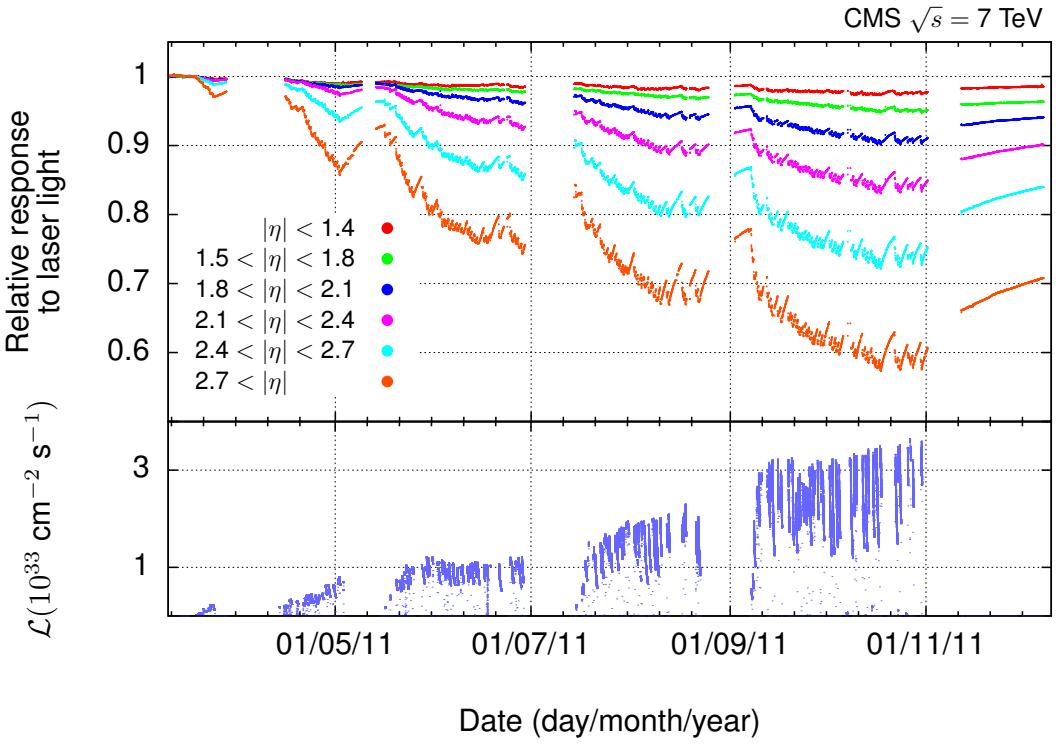

Figure 3.7: Exposure to radiation causes a change in relative response to laser light. The different colors represent different η rings. The bottom plot shows the instantaneous luminosity as a function of time. As crystals are exposed to radiation the crystals lose transparency and less scintillation light or in this plot laser light reaches the photodetector. Crystals slowly recover transparency in the absence of exposure to radiation [51].

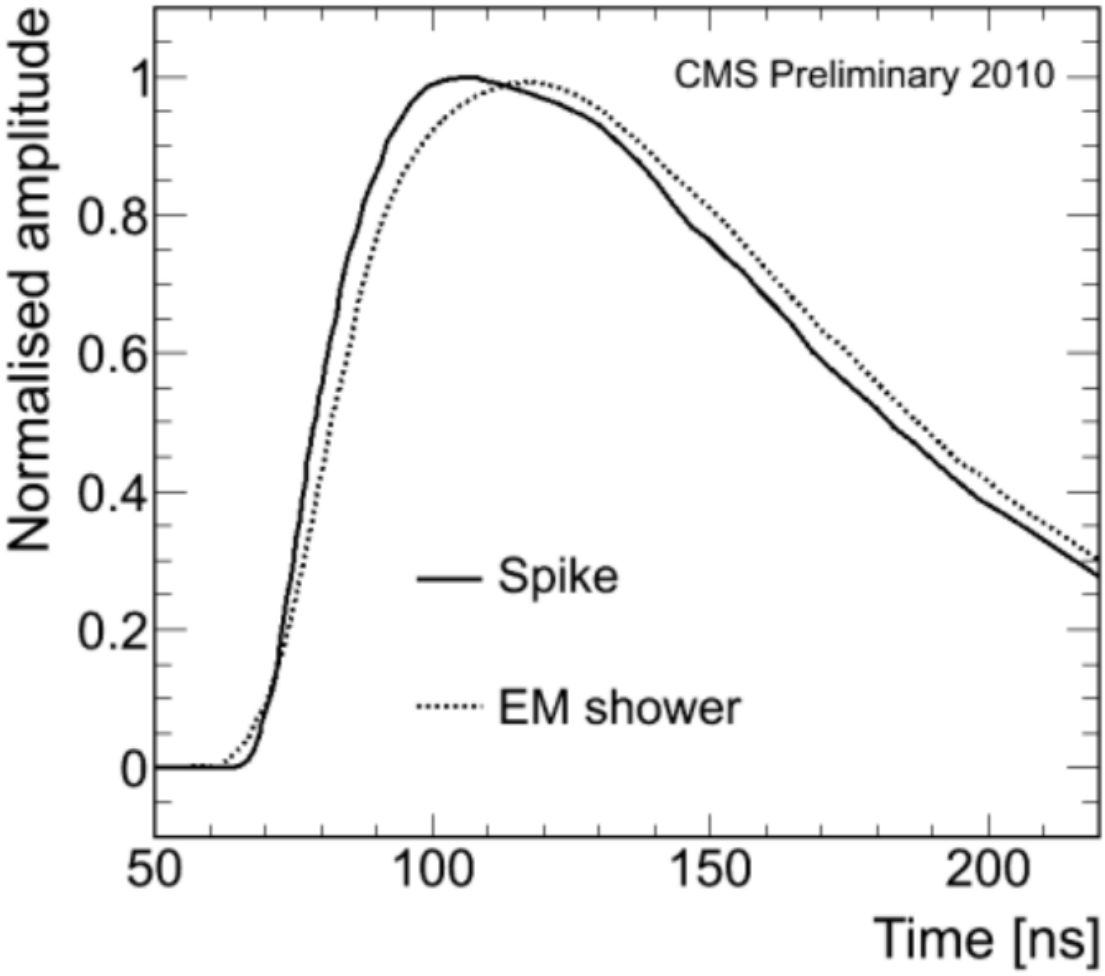

Figure 3.8: The spike pulse shape has a sharper average rise, because it directly ionizes the APD as opposed to a normal particle which produces scintillating light in the crystals [52].

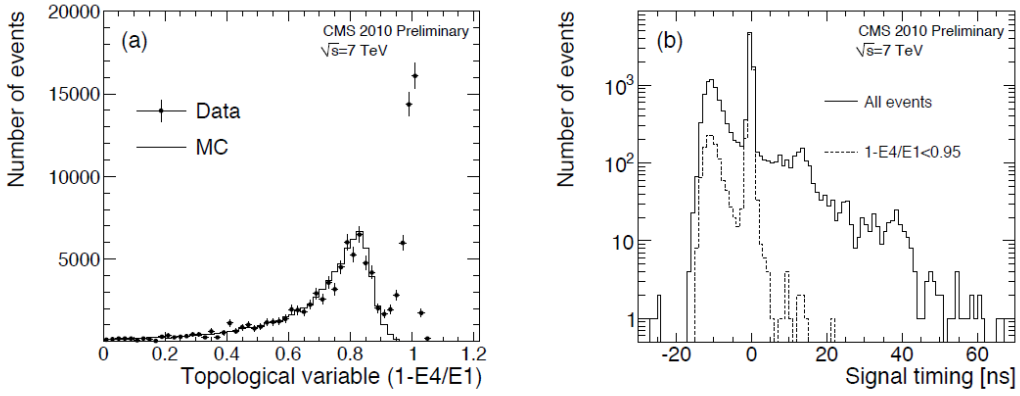

Figure 3.9: The average timing of spikes is more negative than the average timing of normal events. Spikes deposit most of their energy in a single crystal while normal events spread the energy into surrounding crystals, so we can use this property to select a subset of events which is predominantly spikes, as shown by the left subplot. After performing this selection criteria, events with negative timing below 3 ns are much more likely to be from spikes than events with timing around 0 ns [53].

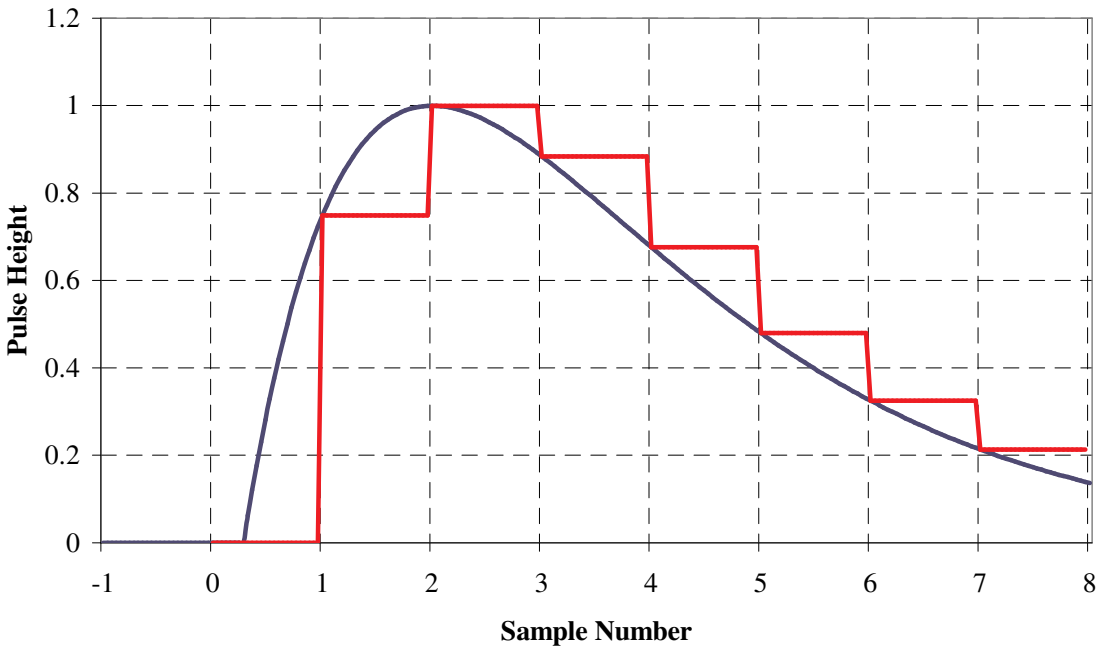

Figure 3.10: ECAL electronics pulse shape [17].

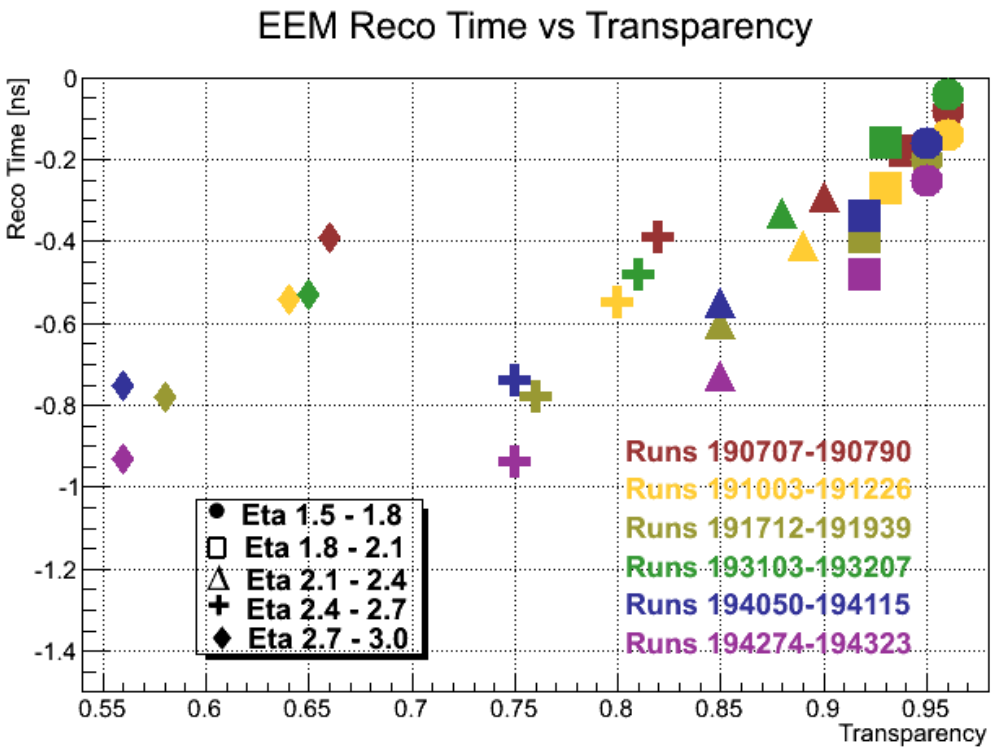

Figure 3.11: The change in timing is proportional to the transparency loss. This is shown by the difference in average timing before and after a technical stop, during which the beam is off and the crystals have time to recover from radiation damage. Crystals in higher η regions are exposed to more radiation, so the rate of transparency loss is expected to be higher.

3.2.3 The Hadronic Calorimeter

The CMS hadronic calorimeter (HCAL) is sandwiched between the ECAL and the magnet (described in Section 3.2.4). The HCAL is designed to measure the energy of hadrons. The HCAL also provides an indirect measurement of the energy of undetectable particles such as neutrinos by providing comprehensive coverage of transverse energy over an η range of $|\eta| < 5$ when including the forward HCAL (HF). The HCAL is a sampling calorimeter made up of alternating layers of active material and passive absorber. The active material is scintillator, while the absorber is brass. HCAL is much larger in size than ECAL because hadrons deposit a lower percentage of their energy as they pass through matter than electromagnetic particles do. HCAL is organized into barrel (HB and HO), endcap (HE) and forward (HF) sections. The HF is exposed to the most radiation, so it is made up of radiation hard elements of embedded quartz fibers. For the analysis of associated production of the Z and the J/ψ, the HCAL is used to help distinguish between hadrons, electrons and muons.

3.2.4 The Magnet

The CMS magnet is located between the HCAL and the muon detector. While the magnet does not directly provide any information, a strong magnetic field enables the subdetectors which measure the trajectory of charged particles (the tracker, and the muon detector described in Section 3.2.5), to also measure the charge and momentum of these charged particles. The magnetic field strength is 3.8T. The magnet is 13 m long and 6 m wide, the largest such magnet of its type. It is a solenoidal magnet made of niobium-titanium and is superconducting. The muon detectors are interspersed with an iron structure that surrounds the magnet coils. This "return yoke" has a 14 meter diameter and acts to prevent strongly interacting particles from reaching the muon detector. The magnet also provides structural support to hold CMS together [48].

3.2.5 The Muon Detector

The muon system is designed to measure the trajectory of muons as they are bent by the magnetic field in the return yoke, a 12-sided iron structure that surrounds the magnet and guides the field. It also measures muons' charge and momentum [54]. As noted

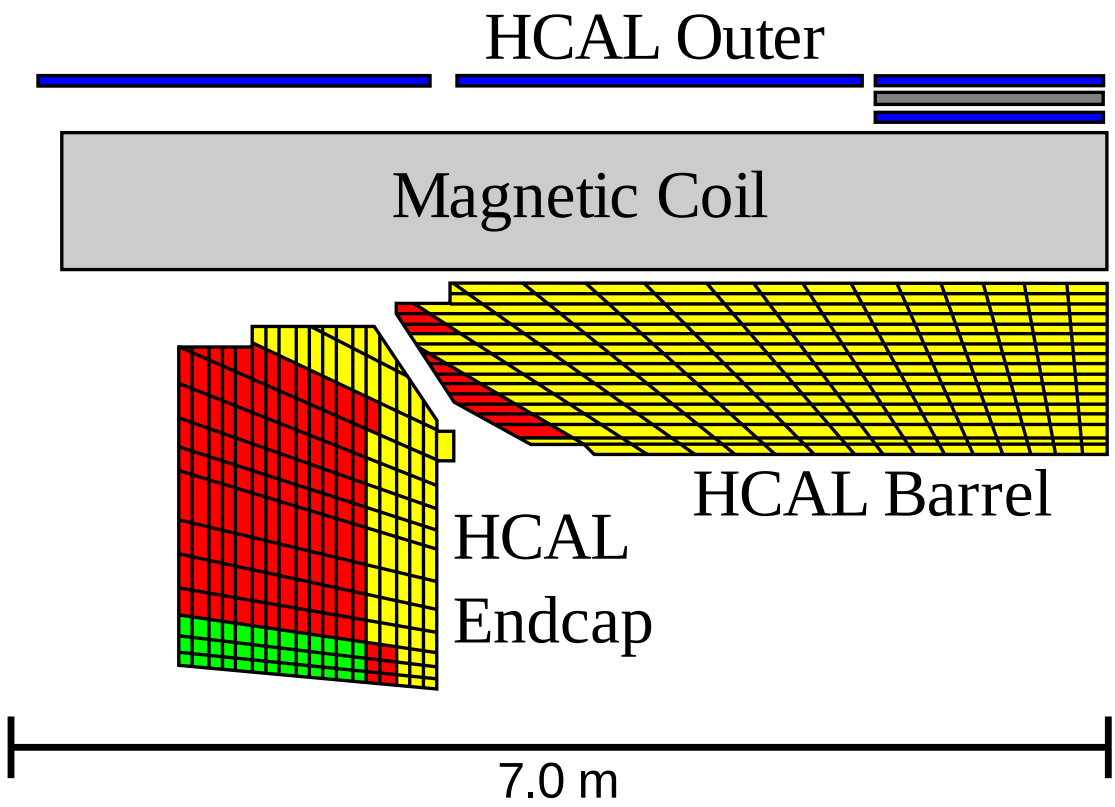

Figure 3.12: Schematic of CMS HCAL. The HCAL measures the energy of hadronic particles such as pions.

above, muons are MIPs, which deposit only a small fraction of energy per unit length traversed through matter. Most SM particles lose all or almost all of their energy before passing through the muon system. The muon system uses different electronics based on the amount of radiation that will impact the detector. The muon system uses drift tubes (DT), resistive plate chambers (RPCs), and cathode strip chambers (CSC). The CMS detector can reliably detect muons with momentum above around 3 GeV. The resolution of the CMS detector in determining muon momentum is better than 10% of the muon's momentum up to about muon momentum of 1,000 GeV/c, and about 1% up to muon momentum of 100 GeV/c. The muon system is vital to this analysis because it allows for the reconstruction of the decays of the Z and the J/ψ to muons, as seen by the sharp peaks in Fig. 3.13.

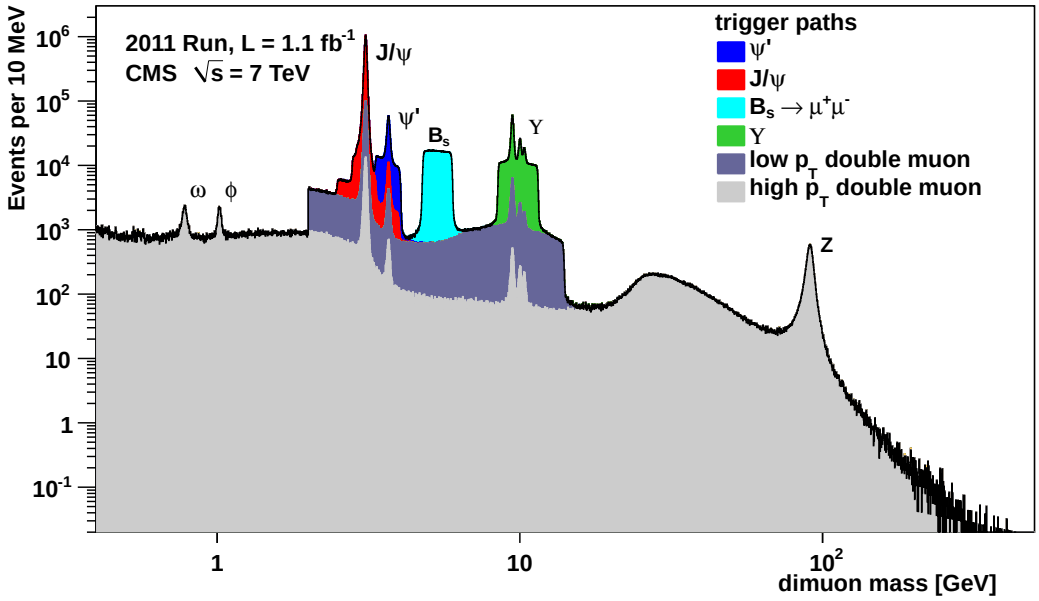

Figure 3.13: Dimuon mass spectrum seen with the CMS detector. This analysis uses muons to reconstruct the Z boson and the J/ψ.

The central region of the muon detector, $|\eta| < 1.2$ is covered with DT, the traditional low occupancy technology that allows for precise trajectory reconstruction. The drift tubes are each 4-cm wide and contain a stretched wire within a gas volume. When a charged particle passes through the gas it knocks out electrons which follow the electric

field to the positively charged wire.

Muons are very important to CMS precisely because the misidentification rate of muons is so low. Especially when considering a massive particle like the Z boson, which decays to 2 oppositely charged muons, the misidentification rate of a muon will be very small. For the case of the J/ψ the misidentification rate is somewhat higher, simply because at low momentum the muon traverses less of the muon detectors so there is less information to distinguish it from for instance a pion. There are also many more low momentum muon candidates which could potentially form into a J/ψ and the cross section to produce lower momentum muons from Drell-Yan production or B decays is higher than for higher momentum muons. However, the misidentification rate for muons is well below 1%. It is measured using hadrons such as the Kaon, which decay into two pions, and then measuring the rate at which one of the two pions with a common decay vertex, and which reconstruct to the resonant mass, is misidentified as a muon [54]. The process is similar to the tag-and-probe technique described in Section 4.4.

3.2.6 The Trigger

The LHC collides protons at a very high rate, of 40 MHz, and at a bunch spacing of 50 ns. Most collisions produce events that do not contain interesting physics, and there is too much data produced to store information about every collision. The rate at which interesting events are produced is orders of magnitude smaller than these uninteresting collisions. This necessitates using triggers to reduce the rate of incoming information or the amount of data the computers must process. The CMS trigger relies on a two stage process, with each filter needing to be passed in steps. The Level-1, or L1, trigger is the initial trigger, which reduces the rate to 100 kHz [55]. The L1 trigger is composed of custom electronics that process data from ECAL, HCAL and the muon detectors. Finally the high level trigger (HLT) reduces the rate to around 300 Hz. The HLT is a multi-processor farm composed of more than 10,000 cores. The HLT criteria are implemented by software running on a processor farm, as opposed to the L1 trigger criteria, which is implemented by custom hardware. A small portion of all events are retained to monitor the performance of HLT, but the bulk of the events which do not pass HLT are not written to tape [56].

The analysis of associated production of Z and J/ψ uses triggers based on the leptonic

decays of the Z. The leptonic decay of the Z boson provides a clean signal that does not need to be reduced due to computing resource constraints and is highly efficient.

Chapter 4

Event Selection

This chapter describes the criteria used to select the events used in this analysis. Events were selected which had a $Z \to \mu^+\mu^-$ or a $Z \to e^+e^-$ and in addition a $J/\psi \to \mu^+\mu^-$ that passed all of our selection criteria, which will be described in Section 4.2. These events must have at least four leptons in the final state, with at least one pair of oppositely charged muons which reconstruct to have a mass near that of the J/ψ and a pair of oppositely charged muons or electrons which reconstruct to have a mass near that of the Z boson. Events were collected with the full $19.7\,\mathrm{fb}^{-1}$ at a center-of-mass energy of 8 TeV recorded with the CMS detector over the year of 2012, as described in Section 4.1.

4.1 The Data

The dataset is collected through the 4 running periods of 2012. The datasets used were DoubleMuParked2012(ABCD) and DoubleElectron2012(ABCD), where the (ABCD) represents the time of year at which the run was taken, while the DoubleMuParked2012 represents that the dataset contains two muons; likewise DoubleElectron2012 represents the dataset contains two electrons. This dataset was determined to have $19.7\,\mathrm{fb}^{-1}$ with an uncertainty of 2.5% by two methods, one using signals from the Forward HCAL Calorimeter (HF) and the other using the Pixel detector [57]. Both methods rely on counting the amount of radiation passing through the detector relative to a known amount of radiation used for calibration. The HF method relies on specialised electronics that can read out signals at a very high rate; it is used to monitor the luminosity

even for unstable beams, but has a larger uncertainty than the Pixel detector for stable beam conditions. The Pixel detector has a low occupancy of less than 0.1% on average, so it has a linear detector response with increasing luminosity. Luminosity is determined from the number of pixel clusters in a zero-bias event. The absolute calibration is determined with Van der Meer scans [57]. The beam intensity is determined from the beam current, measured with Fast Beam Current Transformers (FBCT). The Van der Meer scan then determines the size and shape of the interaction region by displacing the beams in steps in the x and y directions. The peak instantaneous luminosity over time is shown in Fig. 4.1.

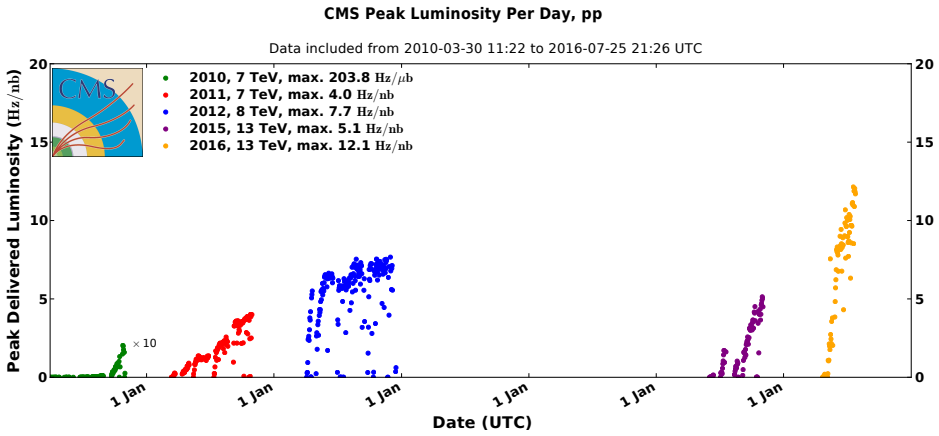

Figure 4.1: The peak luminosity as a function of time for different run conditions of the LHC. The data used in this thesis was collected at a center-of-mass energy of 8 TeV during 2012. Each point represents a single beam fill.

The triggers used in this analysis for the associated production of a Z boson and a J/ψ relied on triggering on the leptons from the Z. The triggers used were the double electron and the double muon triggers, requiring one electron (muon) with p_{T} greater than 17 GeV/c and one with p_{T} greater than 8 GeV/c. Additionally, an inclusive J/ψ trigger requiring a J/ψ with p_{T} greater than 8 GeV/c in a mass range between 2.85 and 3.35 GeV was used to determine the fit template for the shape of the J/ψ. The inclusive J/ψ sample contains over 150,000 events selected from a subset of Run2012B. This dataset is collected with a dimuon trigger that requires an object with a p_{T} above 8 GeV and a reconstructed invariant mass of between 2.85 and 3.35 GeV.

4.2 Selection Criteria

I use the selection criteria which match the official CMS guidelines whenever possible. I use the Golden JSON file for 22Jan2013 to determine which lumi sections to use. A lumi section is a subset of a run during which the instantaneous luminosity is unchanging, while a run is a subset of a fill during which the CMS detector is unchanging. Each fill is a new injection of protons in the beam. This file is produced by the CMS collaboration and indicates that all sub-detectors were working well during the luminosity section of the run. The leptons (muons or electrons) from the Z boson are required to have $p_{\mathrm{T}} > 20\,\mathrm{GeV}$ and to have opposite charges. Only the two highest p_{T} oppositely charged leptons in the event are considered. The probability that the two leptons come from the same vertex, vertex compatibility, must be $> 0.5\%$. Vertex compatibility is determined by a least squares fit using the Kalman vertex fitting algorithm. The leptons from the Z must match with the leptons that triggered the event, the difference between the η and ϕ positions of the lepton has to be less than 0.3. Additionally, muons from the Z are required to pass the `Tight Id` selection criteria which include a requirement relative to the primary (highest p_{T}) vertex, as defined in Ref. [54]. The `Tight Id` requirements are summarized in Table 4.1.

Electrons from the Z are required to pass the `Medium Id` requirement, which has various quality cuts as defined in Ref. [2] and shown in Table 4.2. The $|\Delta\eta| = |\eta_{SC} - \eta_{in}^{\mathrm{extrap}}|$, with η_{SC} the super cluster (SC) energy-weighted position in η, and $\eta_{in}^{\mathrm{extrap}}$ the track η extrapolated from the innermost track position to the position of closest approach to the SC ensures compatibility between the track of the electron as determined with the tracker and the ECAL position, to reduce the misidentification probability. The $|\Delta\phi|$ requirement follows the same principles as the $|\Delta\eta|$. The H/E_{SC} selection, where H is the sum of the HCAL tower energies within a cone of $\Delta R = \sqrt{(\Delta\eta)^2 + (\Delta\phi)^2} = 0.15$ around the electron direction, and E_{SC} is the energy of the SC. This requirement distinguishes between electrons and hadrons, as electrons deposit a higher fraction of their energy in ECAL. The lateral extension of the shower along the η direction is given by:

$$\sigma_{\eta\eta}^2 = [\sum(\eta_i - \bar{\eta})^2 w_i] / \sum w_i \tag{4.1}$$

where the sum runs over the 5×5 matrix of crystals surrounding the highest transverse energy crystal of the SC, and w_i is a weight that depends logarithmically on the contained energy; the η_i are expressed in units of crystals. The impact parameters, the distance to the vertex at the point of closest approach in the transverse plane, in the transverse and longitudinal directions, d_0 and d_z respectively, are used to reject secondary electrons. A missing hit occurs when the detector predicts a hit based on the trajectory determined with the tracker hits but there is no hit measured. This is known as a ghost hit, with the additional requirement that the ghost hit is not due to known conditions such as if a detector module is turned off. The requirement that $|1/E_{SC} - 1/p|$, where p is the track momentum at the point of closest approach to the vertex, is small, which further limits the misidentification rate of electrons. The particle flow (PF) isolation is defined as:

$$\mathrm{Iso}_{PF} = \sum p_{\mathrm{T}}^{\mathrm{charged}} + \max[0, \sum p_{\mathrm{T}}^{\mathrm{neutralhadron}} + \sum p_{\mathrm{T}}^{\gamma} - p_{\mathrm{T}}^{\mathrm{pileup}}] \tag{4.2}$$

where the sums range over the charged PF candidates, neutral hadrons and photons, within a chosen ΔR cone around the electron direction. The charged candidates are required to come from the vertex of interest, and $p_{\mathrm{T}}^{\mathrm{pileup}}$ is a correction related to pileup. As photons pass through detector material there is a chance that the photon converts into an electron and positron pair; this degrades the resolution of the photon because the magnetic field affects the charged particles. About 27% of photons convert in the center of EB, and 62% convert at the edge of EE [58]. If the probability of the electron from a fit to the track reconstruction is too high the electron is rejected as coming from a photon conversion. Electrons are subject to energy regression corrections. These regression corrections have a negligible impact on this measurement, and are described in [59]. The reconstructed Z mass must be between 80 and 100 GeV.

All muon candidates are paired together to form J/ψ candidates with the exception of events which contain a $\mathrm{Z} \to \mu^+\mu^-$, in which case the muons from the Z are not considered in reconstructing candidate J/ψ. There are only 3 events which contain both a Z and two possible J/ψ candidates passing all selection criteria; in these rare cases we keep the J/ψ candidate with the most compatible vertex as determined by a least squares Kalman fit. The J/ψ is required to have mass between 2.85 and 3.35 GeV, and

Table 4.1: Tight ID requirements for muon from Z [1].

Requirement
Reconstructed as a global muon
Track transverse impact parameter $d_{xy} < 0.2$ cm from the primary vertex
The longitudinal distance of the track from the primary vertex $d_z < 0.5$ cm
The $\chi^2/ndof$ of the global muon track fit is < 10
At least one muon chamber hit included in the global-muon track fit
Muon segments in at least two muon stations
At least one pixel hit
At least 6 tracker layers with hits

Table 4.2: Electron from `ZMedium ID` requirements [2].

Variable	Upper value, Barrel	Upper value, Endcaps
$\lvert\Delta\eta\rvert$	0.004	0.007
$\lvert\Delta\phi\rvert$	0.06	0.03
$\sigma_{\eta\eta}$	0.01	0.03
H/E	0.12	0.10
$\lvert d_0\rvert$	0.02 cm	0.02 cm
$\lvert d_z\rvert$	0.1 cm	0.1 cm
$\lvert 1/E_{SC} - 1/p\rvert$	0.05 GeV^{-1}	0.05 GeV^{-1}
$Iso_{PF}(\Delta R = 0.3)/p_{\text{T}}$	0.15	0.15
Conversion-fit probability	10^{-6}	10^{-6}
Missing hits	1	1

also to have J/ψ rapidity $|y| < 2.1$. The muons from a J/ψ are required to pass the `Soft Id` relative to the primary vertex, as defined in Ref. [54]. The `Soft Id` requires loose transverse and longitudinal impact parameter cuts, $d_{xy} < 0.3\,\text{cm}$ and $d_z < 20\,\text{cm}$ with respect to the primary vertex, and various quality cuts: track matched with at least one muon segment, at least 6 tracker layers hits, at least one pixel layer, and the track is high-purity (has a high probability of being an interesting track, which passes the criteria defined in [60]). The muon p_{T} of the leading p_{T} muon is required to be > 3.5 GeV. When the muon has $|\eta| < 1.2$ the sub-leading muon also has to have p_{T} $> 3.5\,\text{GeV}$. When the sub-leading muon has $|\eta| > 1.2$ the sub-leading muon p_{T} has to be $> 2.5\,\text{GeV}$. Both muons are required to have $|\eta| < 2.1$. The tracks of the muons are paired together and traced back to create a common vertex. This vertex must have a vertex compatibility $> 0.5\%$. In addition, the J/ψ is required to be within 0.5 cm in the z-direction (along the beam-line) of the Z boson's reconstructed vertex. This selection criteria reduces the amount of pile-up, or events which contain a Z and a J/ψ from two separate pp collisions in the same bunch crossing. The lifetime of the J/ψ in the transverse plane must be between -1 and 5 ps. The lifetime in the transverse plane is given by:

$$t_{xy} = (m^{\text{J}/\psi}/p_{\text{T}}^{\text{J}/\psi}) \cdot L_{xy}^{\text{J}/\psi} \tag{4.3}$$

where $L_{xy}^{\text{J}/\psi} = (\vec{r}_T \cdot \vec{p}_T^{\,\text{J}/\psi})/|\vec{p}_T^{\,\text{J}/\psi}|$, and $\vec{r}_T$ is the transverse distance between the reconstructed Z boson position and J/ψ vertex position. Because $m^{\text{J}/\psi}/p_{\text{T}}^{\text{J}/\psi}$ is an approximation of m^B/p_{T}^B, this transverse lifetime distribution will not necessarily agree perfectly with the expected lifetime of the b-hadron of about 1.3 ps even when the J/ψ is from the decay of a b-hadron (nonprompt).

4.3 Monte Carlo

This analysis uses MC to determine the efficiency times acceptance (henceforth referred to as efficiency) of the J/ψ. Over a million inclusive J/ψ MC events were generated with Pythia6. The presence of a Z boson will not change the efficiency of a J/ψ of a given p_{T} and rapidity and polarization, but the distribution of J/ψ p_{T} can change, so the efficiency determined with this MC is applied on a per event basis. Although the analysis measures the rate of associated production given the inclusive production of a

Z, there could be a difference in efficiency between inclusive Z and associated Z due to the higher average p_{T} of the Z for associated production. This efficiency difference is determined with Drell-Yan plus Jets to $\ell^+\ell^-$ Madgraph MC [61].

4.4 Efficiency

The J/ψ efficiency is determined in 20 bins of p_{T} and 7 bins of rapidity, by measuring the fraction of generated events which pass all selection criteria. The efficiency map for unpolarized J/ψ is shown in Fig. 4.2. Efficiencies are corrected by scale factors. Scale factors are used to ensure that the muon efficiency in MC matches that in data. These scale factors are determined using the tag-and-probe method in [62]. The tag-and-probe method determines the efficiency by utilizing resonances such as the J/ψ or the Z. One of the muons from the J/ψ is required to pass a tight identification (the tag), and the other muon is probed based on the cuts for the identification we want to measure the efficiency of. We next fit the mass distribution of the tag and passing probe, and of the tag and failing probe, with a signal and background model. The efficiency is determined by the ratio of the signal yields from tag and passing probe as compared to all probes, or $\epsilon = P_{pass}/P_{all}$ where P_{pass} is the number of passing probes and P_{all} is the total number of probes counted using the resonance [63]. The scale factor is determined as the ratio of efficiency in data and MC.

The spin polarization could be different between inclusive J/ψ production and associated production. This difference could lead to large changes in efficiency, because of the requirement that both muons from the J/ψ are above a p_{T} threshold and in a central η region. The more balanced in p_{T} and η the muons are from the J/ψ, the higher the efficiency. The effect of polarization is determined by weighting the events by:

$$\frac{\mathrm{d}N}{\mathrm{d}\cos\theta^\star} \propto 1 + \lambda_\theta \cos^2\theta^\star \tag{4.4}$$

where λ_θ varies from -1 (longitudinal) to 0 (unpolarized) to 1 (transverse) and $\theta^\star$ is the angle between the direction of the positive muon's momentum in the J/ψ decay frame and the direction of the J/ψ trajectory, shown in Fig. 4.3. The efficiency is highest when λ_θ is -1, because the efficiency is highest when $\cos\theta^\star$ is near 0 as shown in Fig. 4.4.

The efficiency for the three polarization scenarios considered for the 20 p_{T} used in

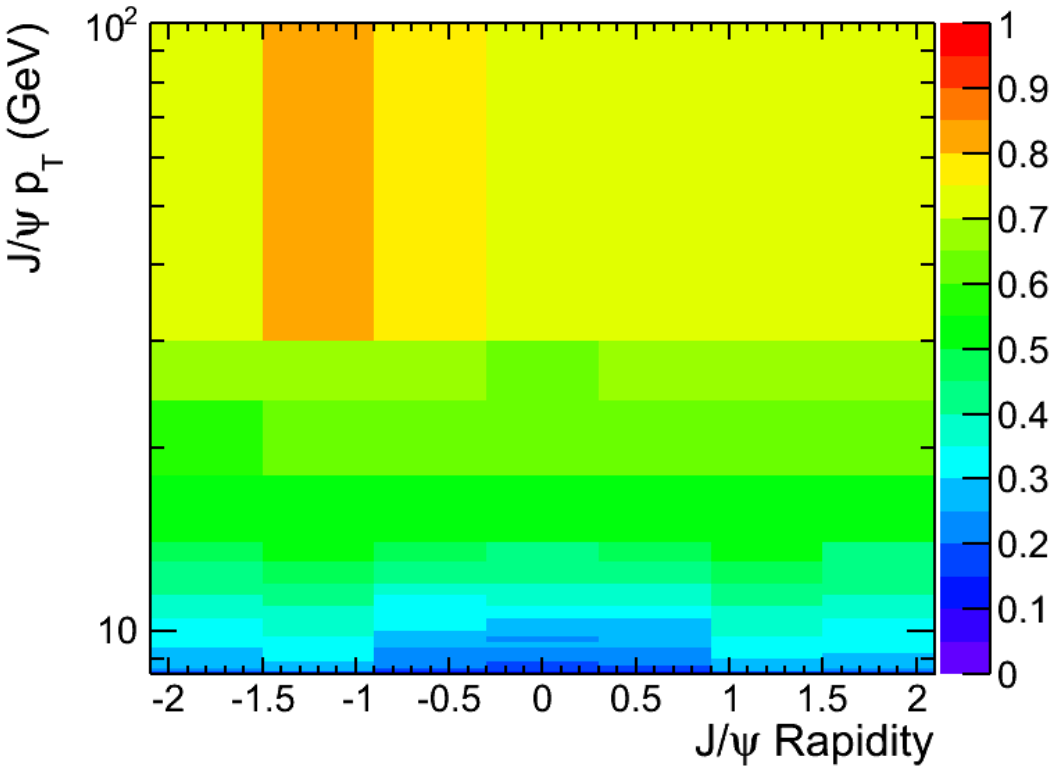

Figure 4.2: The efficiency of the J/ψ assuming unpolarized production.

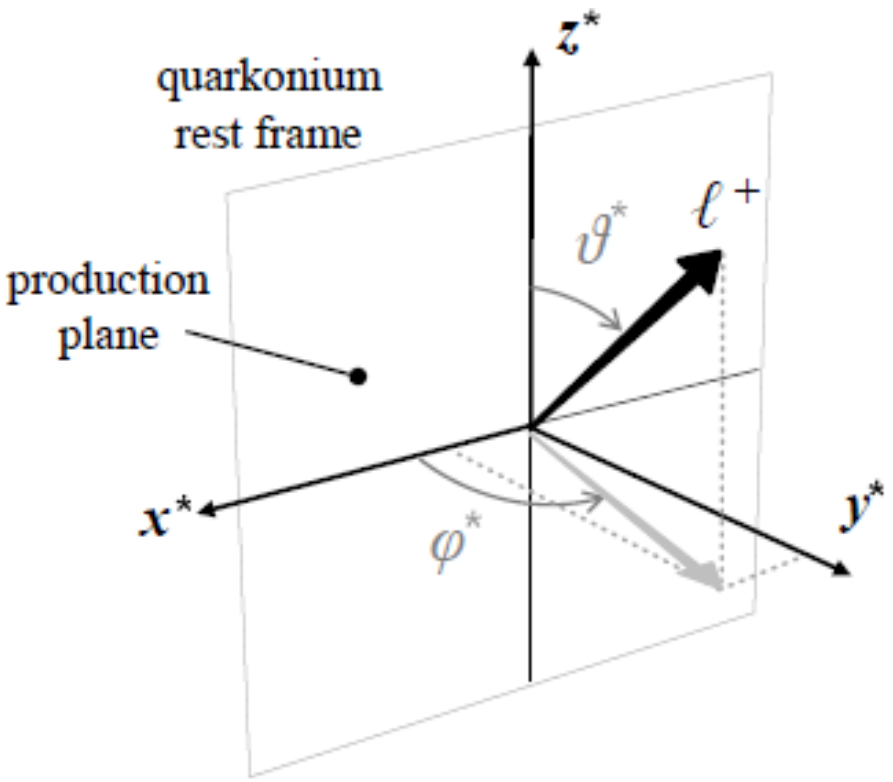

Figure 4.3: The angle $\theta^{\star}$ between the positive muon in the J/ψ decay frame and the J/ψ path in the lab frame [18].

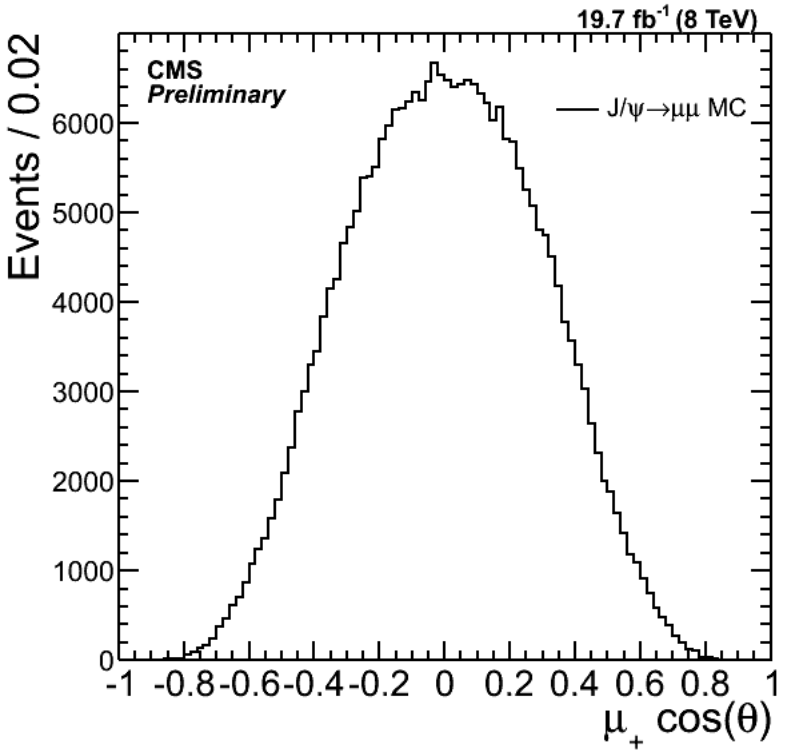

Figure 4.4: Reconstructed MC J/ψ $\cos\theta^{\star}$. While the MC is generated with the assumption of unpolarized J/ψ, which implies a flat distribution in $\cos\theta^{\star}$ the efficiency is highest for muons with a value of $\cos\theta^{\star}$ near zero which causes the reco distribution to peak near zero.

Table 4.3: Polarization effect on efficiency

$p_{\mathrm{T}}^{\mathrm{J}/\psi}$ GeV	Unpolarized ($\lambda = 0$)	Longitudinal ($\lambda = -1$)	Transverse ($\lambda = 1$)
8.5-8.6	0.162427	0.231529	0.127861
8.6-8.7	0.218914	0.311432	0.172679
8.7-8.8	0.233989	0.33266	0.184707
8.8-8.9	0.247642	0.349704	0.196332
8.9-9.0	0.25075	0.356668	0.197946
9.0-9.2	0.261912	0.370641	0.207586
9.2-9.4	0.269966	0.381604	0.214203
9.4-9.6	0.292085	0.410632	0.232548
9.6-9.8	0.298457	0.420339	0.237629
9.8-10.0	0.308939	0.433265	0.246828
10.0-10.5	0.329096	0.459421	0.263843
10.5-11.0	0.348838	0.48574	0.280775
11.0-11.5	0.374853	0.517461	0.303593
11.5-12.0	0.399478	0.548396	0.325273
12.0-13.0	0.427339	0.580044	0.350886
13.0-14.0	0.468212	0.626419	0.388681
14.0-18.0	0.519382	0.681003	0.438396
18.0-24.0	0.609773	0.766497	0.53117
24.0-30.0	0.671175	0.813408	0.60019
30.0-100.0	0.739417	0.84838	0.684296
8.5-100	0.342249	0.469344	0.278689

this analysis is shown in Table 4.3. Figures 4.5, 4.6, 4.7 show the efficiency maps for the different polarization scenarios.

The efficiency of the pile-up cut which requires the J/ψ vertex to be within 0.5 cm of the Z vertex is not estimated with inclusive J/ψ MC because inclusive J/ψ does not include a Z vertex. However, this cut is found to expected to kepp virtually all of the prompt signal as shown in Figure 4.8. I verify that this cut is 100% efficient for prompt signal and measure its efficiency for nonpropmt signal with a data-driven approach. For prompt signal I create a sample of inclusive J/ψ data which has a transverse lifetime of less than 0.3 ps (which contains over 99% of prompt J/ψ), and examine the vertex displacement in the z-direction relative to the primary vertex, as shown in Figure 4.9. A similar procedure is done for nonprompt, except creating a sample with transverse

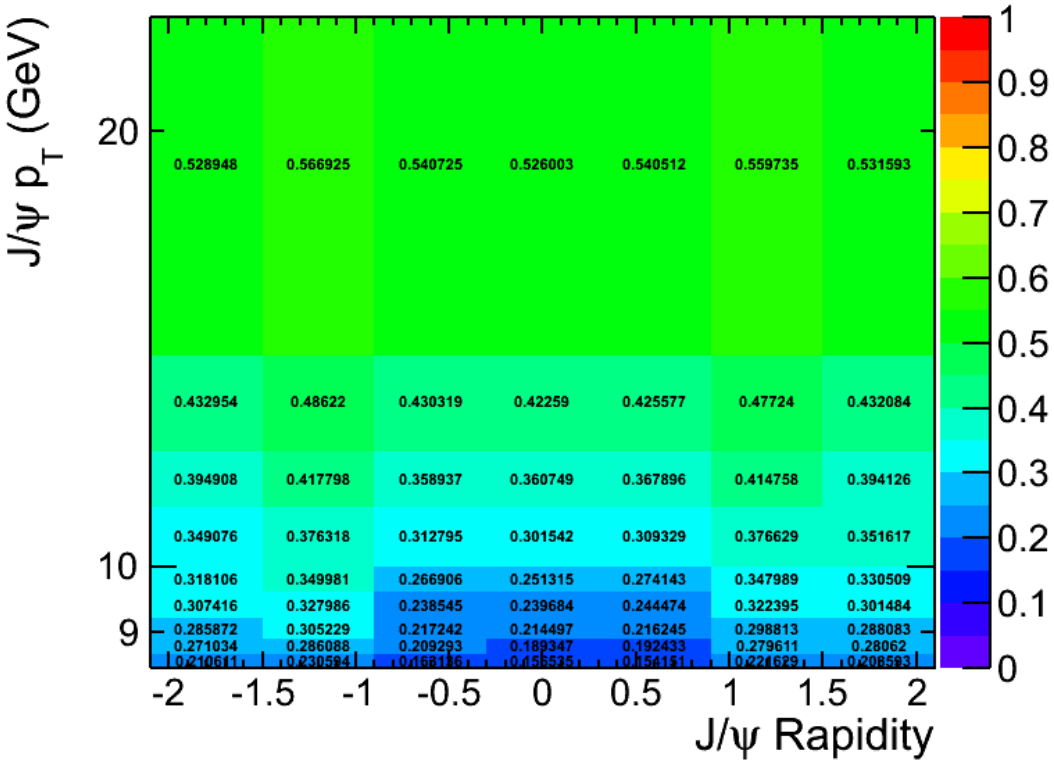

Figure 4.5: The efficiency map for unpolarized J/ψ.

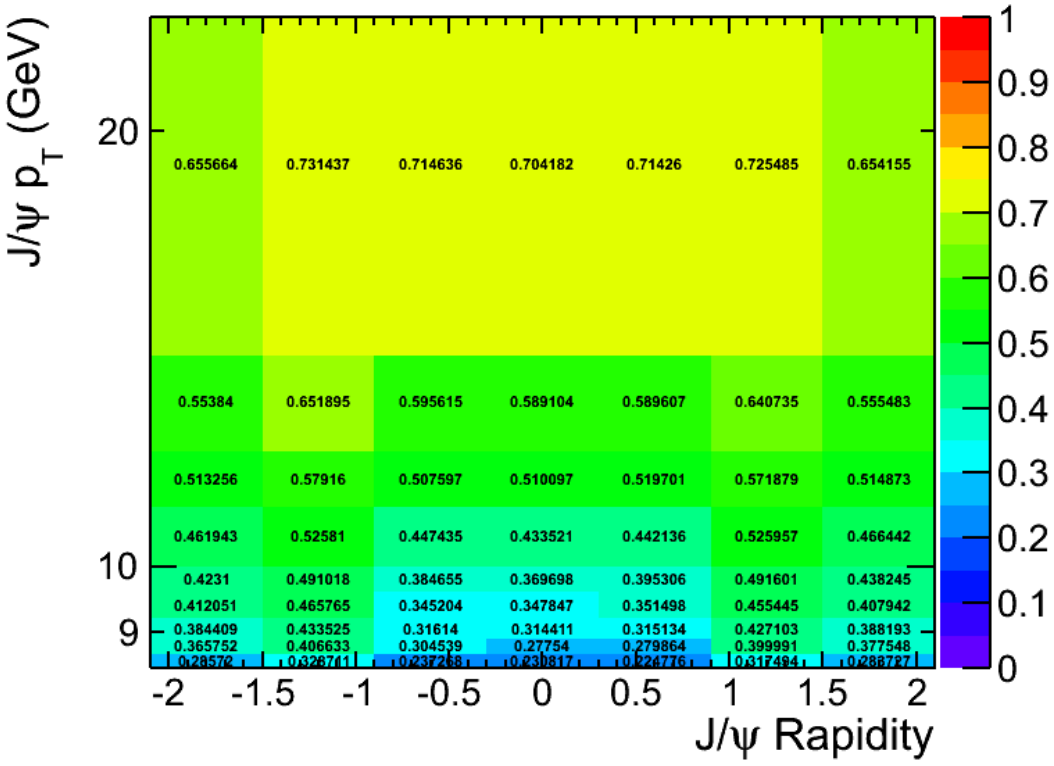

Figure 4.6: The efficiency map for longitudinally polarized J/ψ.

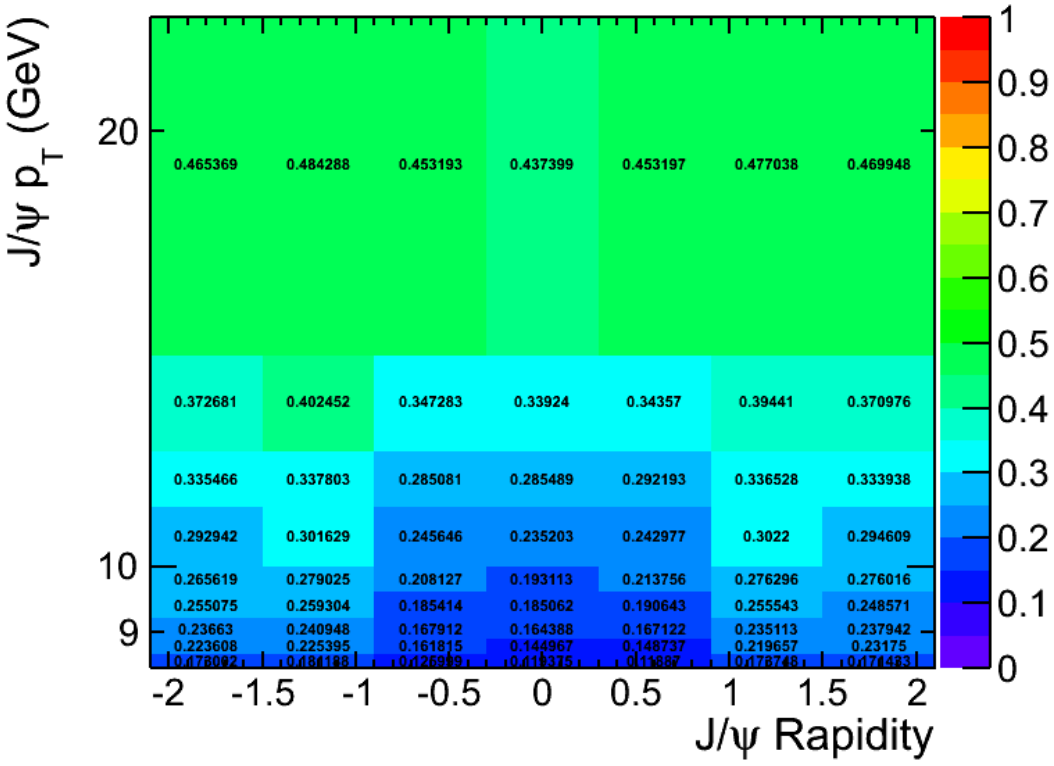

Figure 4.7: The efficiency map for transverse polarized J/ψ.

lifetime above 0.3 ps, as shown in Figure 4.10.

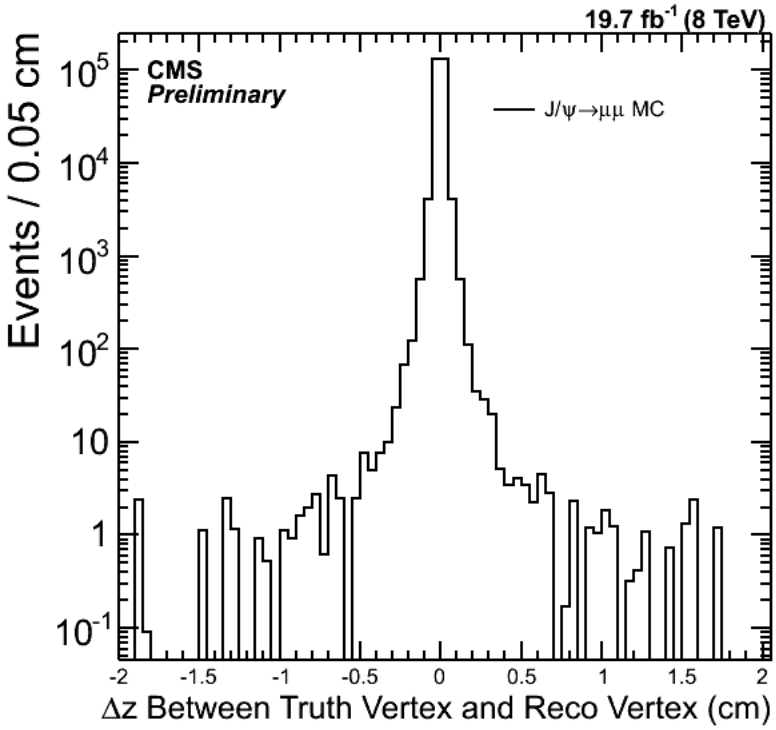

Figure 4.8: Difference in vertex position between truth MC J/ψ and reconstructed MC J/ψ. Note that a negligible number of events have a reconstructed vertex more than 0.5 cm from the position of the truth vertex.

In order to evaluate the efficiency of this cut, I interpolate the number of events expected due to pileup between 0.5 and 3.0 cm. This interpolation is then compared to the actual number of events in this range, and the efficiency is taken as the ratio of remaining events after pileup subtraction relative to the number of events in the signal region of -0.5 to 0.5 cm. This process is described as:

$$\epsilon = N_0/(N_0 + (N_1 - N_2 * SF)) \tag{4.5}$$

where ϵ is the efficiency, N_1 is the number of events with $0.5 < |z| \leq 3$, N_2 is the number of events with $3 < |z| <= 20$ and N_0 is the number of events with $|z| < 0.5$, and SF is a scale factor determined by a Gaussian fit to the pileup region and used to interpolate

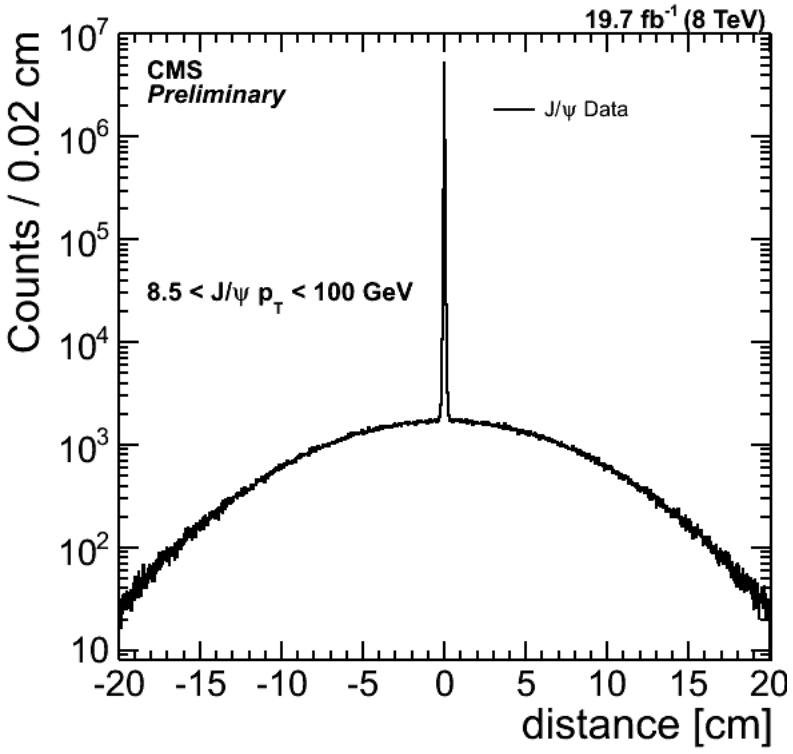

Figure 4.9: Difference in vertex position between reconstructed J/ψ and primary vertex, for events with a transverse lifetime less than 0.3 ps. The sharp peak is due to prompt J/ψ, while the wider Gaussian is due to pileup.

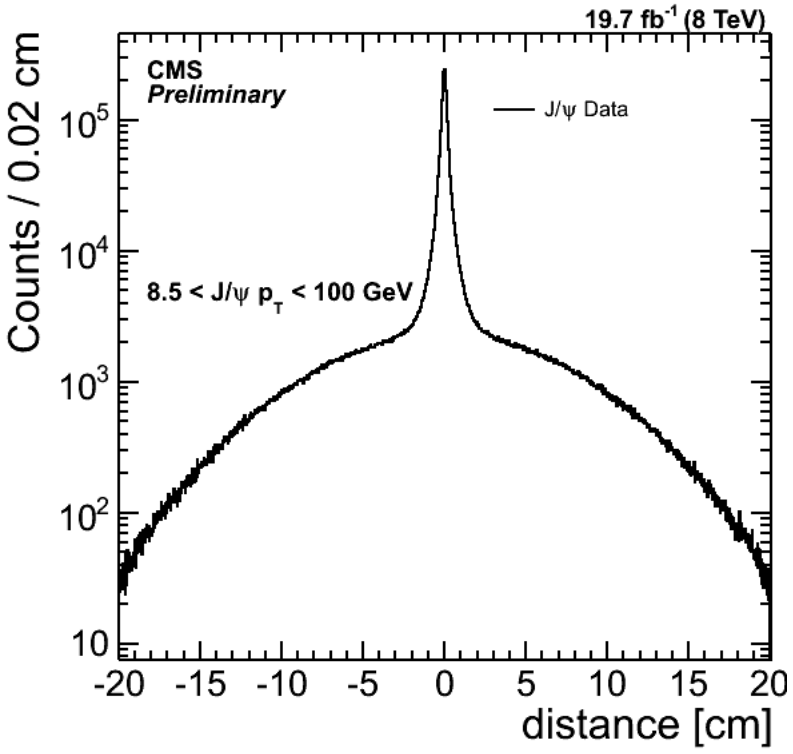

Figure 4.10: Difference in vertex position between reconstructed J/ψ and primary vertex, for events with a transverse lifetime greater than 0.3 ps. The sharp peak is due to prompt J/ψ, while the wider Gaussian is due to pileup.

Table 4.4: Efficiency of the nonprompt pileup cut as a function of J/ψ p_{T}.

$p_{\mathrm{T}}^{\mathrm{J}/\psi}$ GeV	Nonprompt Efficiency
8.5-10	0.94
10-14	0.93
14-18	0.91
18-30	0.86
30-100	0.77
8.5-100	0.91

the amount of pileup between $0.5 < |z| <= 3$. This efficiency is found to be consistent with 1 for prompt J/ψ. For nonprompt J/ψ a similar procedure is followed, with the addition of dividing N_0 by the fraction of nonprompt events with $|z| < 0.5$ and lifetime less than 0.3 ps (about 70% depending on the J/ψ p_{T}). The resulting efficiency is shown in Table 4.4.

Chapter 5

Analysis

The main focus of this analysis is determining the cross section for associated production of a J/ψ and a Z in a pp collision. In order to control for systematic uncertainties such as luminosity uncertainty or the uncertainty on the efficiency to reconstruct a Z, I measure the ratio of associated production to inclusive Z production. I express this as $P(\mathrm{Z} \to \ell\ell + \mathrm{J}/\psi \to \mu^+\mu^- | \mathrm{Z} \to \ell\ell)$, or $R_{\mathrm{J}/\psi}$. This was expected to be a rare process, and the total rate of backgrounds was expected to approximately equal the rate of signal. I use a two-dimensional fit in J/ψ transverse pseudo-lifetime and mass in order to distinguish the signal from Drell-Yan production and J/ψ from the decay of a b hadron (nonprompt). I use a subset of inclusive J/ψ data in order to determine the template shape of J/ψ prompt and nonprompt signal with high precision. This chapter will describe how the signal yield of $P(\mathrm{Z} + \mathrm{J}/\psi \to \mu^+\mu^- | \mathrm{Z})$ for prompt and nonprompt J/ψ is determined.

5.1 Analysis Procedure

There are four main components which I distinguish from each other by utilizing a fitting procedure which will be described in Sec. 5.2. These components are: prompt J/ψ, nonprompt J/ψ, prompt dimuon continuum and nonprompt dimuon continuum. Prompt J/ψ is the primary signal we are interested about in this analysis; it is a J/ψ produced in association with a Z boson or from feed-down from an excited charmonium state. The J/ψ decay to hadronic particles is suppressed by the OZI rule, so it decays

to two muons 5.93% of the time. The hadronic decay suppression also causes the J/ψ to have a relatively long lifetime (though still small at 7.2×10^{-21} seconds) and narrow mass width of 92.9 keV. The J/ψ mass is 3.097 GeV [42]. The J/ψ mass distribution is modeled by the sum of two Gaussians with a common mean but different resolutions. The J/ψ prompt lifetime is similarly the sum of two Gaussians with a common mean. The nonprompt J/ψ is a J/ψ which results from a b hadron. The probability of a b hadron decay containing a J/ψ is 1.09% [42]. A b hadron decay contains at least one muon 10.74% of the time. The lifetime of a b hadron is about 1.3 ps, which is substantially higher than a J/ψ and is long enough that I can use it to distinguish prompt and nonprompt J/ψ. The nonprompt J/ψ has the same template shape as the prompt J/ψ in the mass distribution, and in the lifetime distribution it is modeled by an exponential decay with a double Gaussian smear function. The prompt dimuon continuum is modeled by an exponentially falling function in the mass distribution and by the same shape as the prompt J/ψ in the lifetime distribution. The nonprompt continuum background is modeled by an exponentially falling function in the mass region and an exponential decay convoluted with a double Gaussian smear function in the lifetime distribution.

5.2 Fitting function

The fit technique used is a two-dimensional unbinned extended maximum likelihood fit, in lifetime and mass. An extended maximum likelihood fit is similar to a maximum likelihood fit, except the normalization is free to float [64], which will allow me to determine the yield of the fit. Following [64], the likelihood is defined as:

$$\mathcal{L} = \prod_{i=1}^{N} f(x_i : p_1 ... p_m) \tag{5.1}$$

where $\mathcal{L}$ is the likelihood, $p_1 ... p_m$ are parameters which are free to float in order to maximize the likelihood, and $f(x_i : p_1 ... p_m$ is the probability density for the event x. In a likelihood fit:

$$\int f(x_i : p_1 ... p_m) dx = 1 \tag{5.2}$$

but this constraint is changed in an extended likelihood fit such that:

$$\int f_{ext}(x_i : p_1...p_m)dx = N_{exp} \tag{5.3}$$

where f_{ext} describes both the shape and size of the distribution, and N_{exp} is the total number of expected events [64]. In contrast to f, the normalization of f_{ext} is not constrained. The extended likelihood incorporates information not only from each event, but also from the total number of events. The extended likelihood incorporates information about the total number of events N, such as places where the events were not observed. We can divide the range of x into narrow bins of width Δx small enough that the probability of a bin containing more than a single event is negligible. The probabilities are given by Poisson statistics, $P_0(x) = e^{-\Delta x f_{ext}(x)}$ where $P_0(x)$ is the probability to observe 0 events in range Δx and $P_1(x) = \Delta x f_{ext}(x) e^{-\Delta x f_{ext}(x)}$, where $P_1(x)$ is the probability to observe 1 event in range Δx. Thus the extended likelihood function is given by:

$$\mathcal{L}_{ext} = \prod_{i=1} \Delta x f_{ext}(x_i) \prod_{j=1} e^{-\Delta x f_{ext}(x_j} \tag{5.4}$$

where the first product is over all bins containing an event, and the second product is over all bins. In the limit where the size of the bins goes to 0, the unbinned extended likelihood function is given by:

$$\mathcal{L}_{ext} = [\prod_{i=1}^{N} f_{ext}(x_i : p_1...p_m)] e^{-N_{exp}} \tag{5.5}$$

where $\mathcal{L}_{ext}$ is the extended likelihood function. We maximize the natural log of this function because the calculations are easier and the result is the same. The fitting errors are computed by the second derivatives of the likelihood function (from the inverse of the Hessian matrix).

The distributions being fit are shown in Fig. 5.1 for inclusive J/ψ and Fig. 5.2 for associated J/ψ. The lifetime and mass are determined as described in Sec. 4.2. Each event is weighted according to its efficiency as determined by Sec. 4.4. The extracted yield of the fit gives the amount for each of the four components of the fit, with the most important components being the prompt and nonprompt J/ψ yields. The overall

fit is:

$$f_{ext}(m,t) = N_{ps} \cdot M_s(m) * T_p(t) + N_{ns} \cdot M_s(m) * T_{ns}(t) + N_{pb} \cdot M_{pb}(m) * T_p(t) + N_{nb} \cdot M_{nb}(m) * T_{nb}(t) \quad (5.6)$$

where N_{ps} is the number of prompt J/ψ signal events, N_{ns} is the number of nonprompt J/ψ signal events, N_{pb} is the number of prompt dimuon continuum background events, and N_{nb} is the number of nonprompt dimuon continuum background events, $M_s(m)$ is the J/ψ signal template, $M_{pb}(m)$ and $M_{pb}(m)$ are the mass continuum templates for prompt and non-prompt backgrounds, $T_p(t)$ is the prompt lifetime template and $T_{ns}(t)$ and $T_{nb}(t)$ are the lifetime nonprompt signal and background templates. The templates ($M_s(m)$, $T_s(t)$ and $T_{nb}(t)$) are fixed from the fit to the inclusive J/ψ sample with 150,000 events, (which is a sufficient number of events such that the statistical error on the inclusive shape parameters is negligible), while (N_{ps}, N_{ns}, N_{pb} and N_{nb}) are free to float when fitting the Z + J/ψ associated production. Whenever the statistics of the associated production data allows—there are three or more events with mass outside of 3.0 to 3.2 GeV—the slope of the continuum exponential background is allowed to float differently from the slope as determined by the inclusive J/ψ template. The fit templates are determined and applied in 5 bins of J/ψ p_{T}: 8.5-10, 10-14, 14-18. 18-30 and 30-100 GeV/c. The shape parameters do depend on J/ψ p_{T}, as shown in Figures 5.3, 5.4, 5.5, 5.6, and 5.7. The higher J/ψ p_{T} events have sharper time resolutions. It is important to bin the templates in J/ψ p_{T} because the distribution of p_{T} in inclusive and associated J/ψ can be different. Table 5.1 shows the shape parameters obtained from the fit to the inclusive J/ψ sample.

The numbers of events corrected for efficiency (weights) from the prompt J/ψ production are computed from the fit fractions and the total weights of overall candidate events. The yield for prompt J/ψ, accounting for statistical uncertainty and summing over the 5 p_{T} bins, for (Z $\rightarrow\mu^+\mu^-$) + (J/ψ $\rightarrow\mu^+\mu^-$) is 44.2 $\pm$ 15.1, and the nonprompt yield is 68.4 $\pm$ 14.5. For (Z $\rightarrow$e$^+$e$^-$) + (J/ψ $\rightarrow\mu^+\mu^-$) the total weights of prompt events is 11.1 $\pm$ 7.3 and it is 45.3 $\pm$ 12.9 for nonprompt events.

The results of signal for each p_{T} bin are shown in Table 5.3.

Once the fit shape parameters are determined with an inclusive J/ψ sample, these

parameters and fit template are fixed in the fit of associated J/ψ data, with the yields of the signal and background free to float. The fit results for associated production (integrated over the entire p_{T} range) are shown in Table 5.2 and in Figures 5.8 and 5.9.

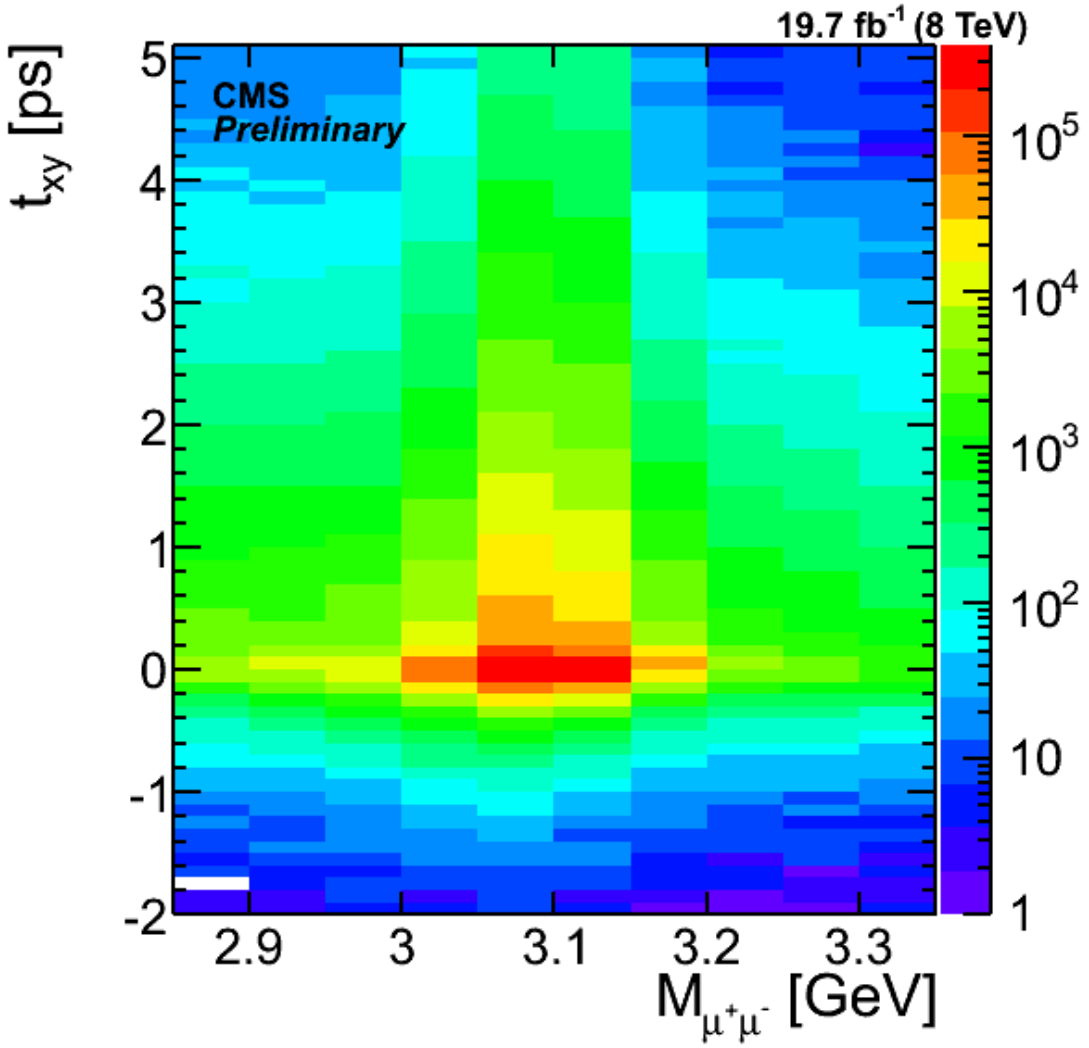

Figure 5.1: The dimuon lifetime vs mass for inclusive J/ψ.

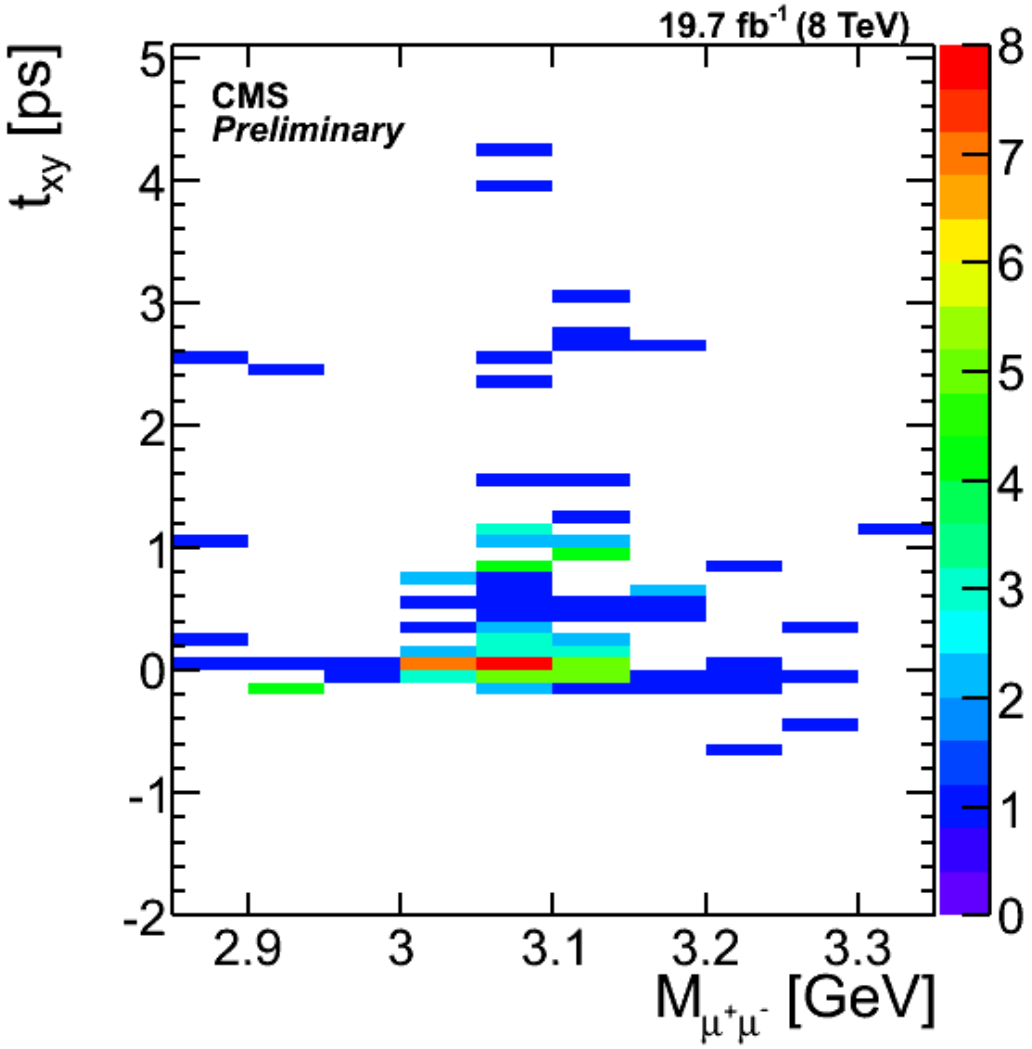

Figure 5.2: The dimuon lifetime vs mass for associated J/ψ.

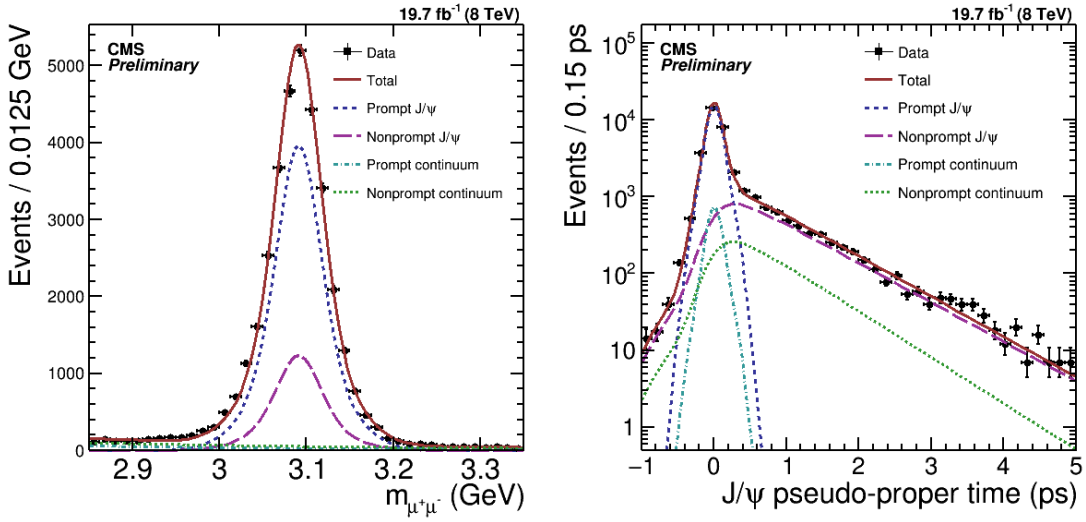

Figure 5.3: The inclusive fit for J/ψ p_{T} between 8.5 and 10 GeV/c.

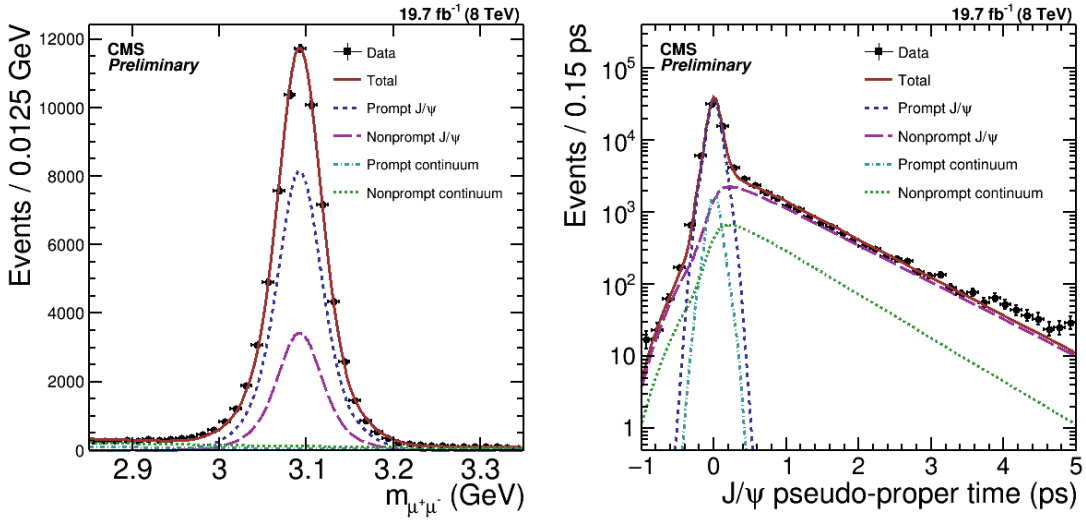

Figure 5.4: The inclusive fit for J/ψ p_{T} between 10 and 14 GeV/c.

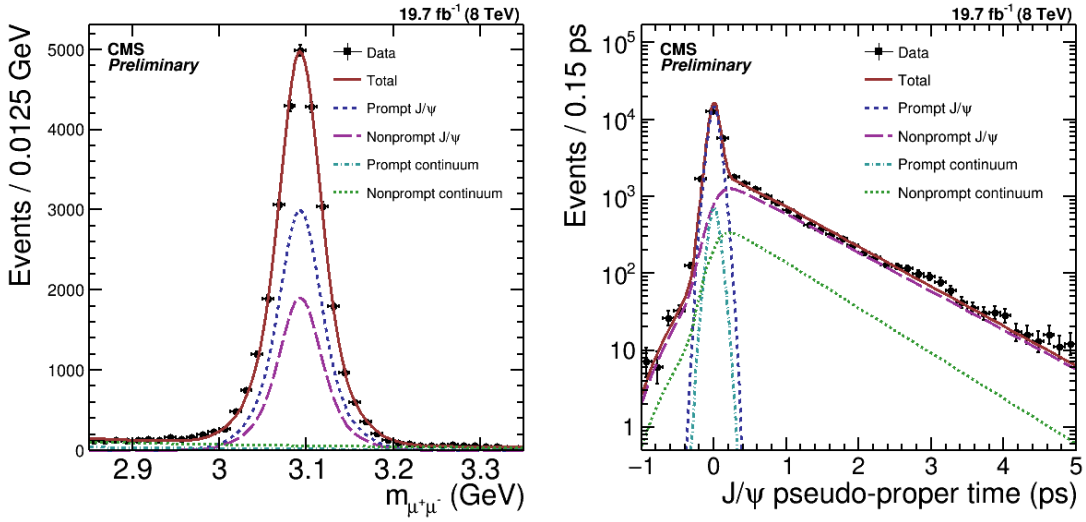

Figure 5.5: The inclusive fit for J/ψ p_{T} between 14 and 18 GeV/c.

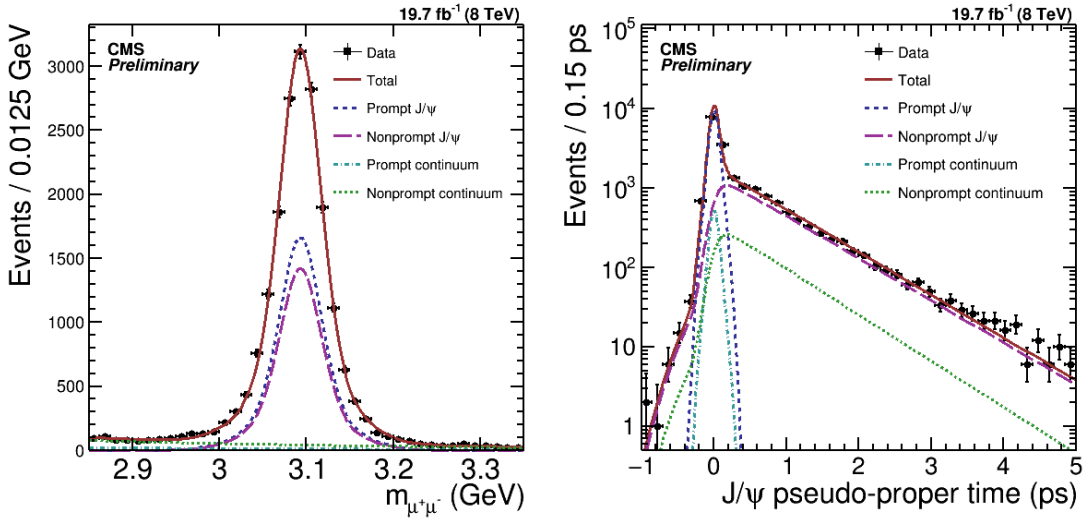

Figure 5.6: The inclusive fit for J/ψ p_{T} between 18 and 30 GeV/c.

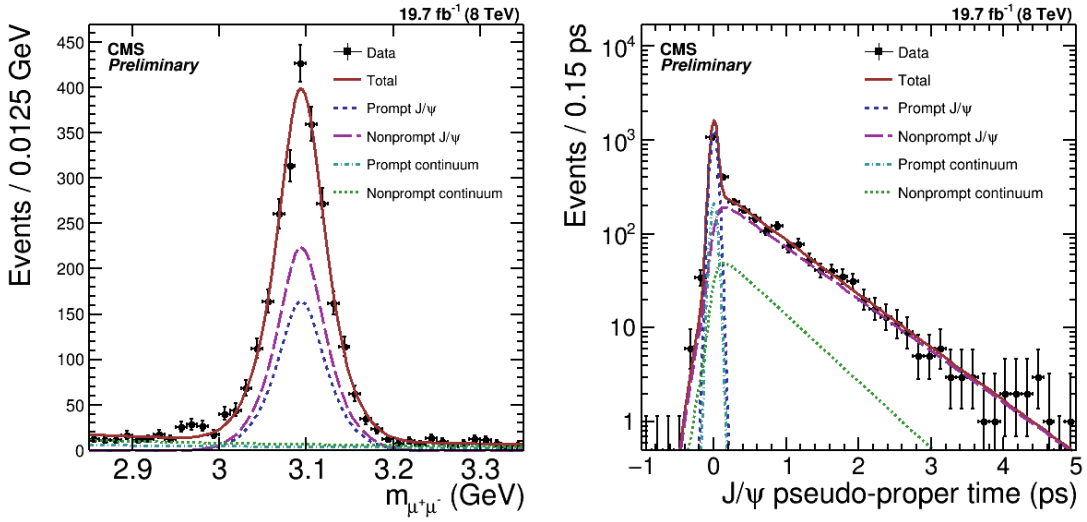

Figure 5.7: The inclusive fit for J/ψ p_{T} between 30 and 100 GeV/c.

Table 5.1: Fit shape parameters integrated over all p_{T} for inclusive J/ψ.

Floating Parameter	Value
J/ψ mass	3.0919 ± 0.0001
σ_{mass-1}	0.0226 ± 0.0003
σ_{mass-2}	0.0488 ± 0.0005
fraction in narrower mass Gaussian	0.54 ± 0.02
Continuum prompt bg slope	-2.9825 ± 0.152
Continuum nonprompt bg slope	-2.493 ± 0.082
Prompt mean time	0.0027 ± 0.0004
σ_{time-1}	0.066 ± 0.001
σ_{time-2}	0.129 ± 0.004
fraction in narrower timing Gaussian	0.607 ± 0.03
Nonprompt J/ψ effective decay lifetime	0.844 ± 0.006
Continuum bg decay lifetime	0.73 ± 0.01
t bg smear gauss σ_{mass-1}	0.394 ± 0.02
t bg smear gauss σ_{mass-2}	0.122 ± 0.004
fraction in narrower smear Gaussian	0.6954 ± 0.04

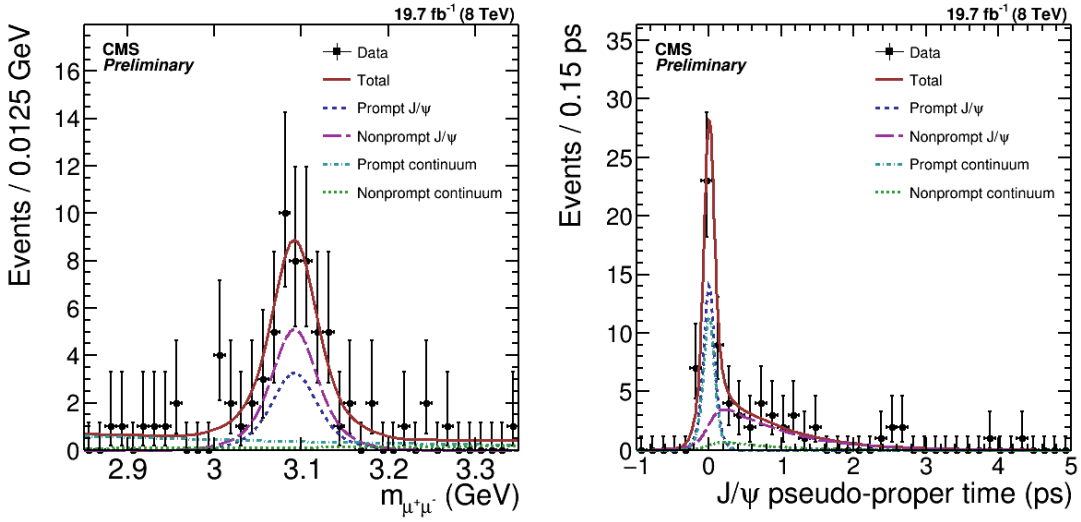

Figure 5.8: $Z \to \mu^+\mu^-$ and J/ψ mass and J/ψ lifetime distributions.

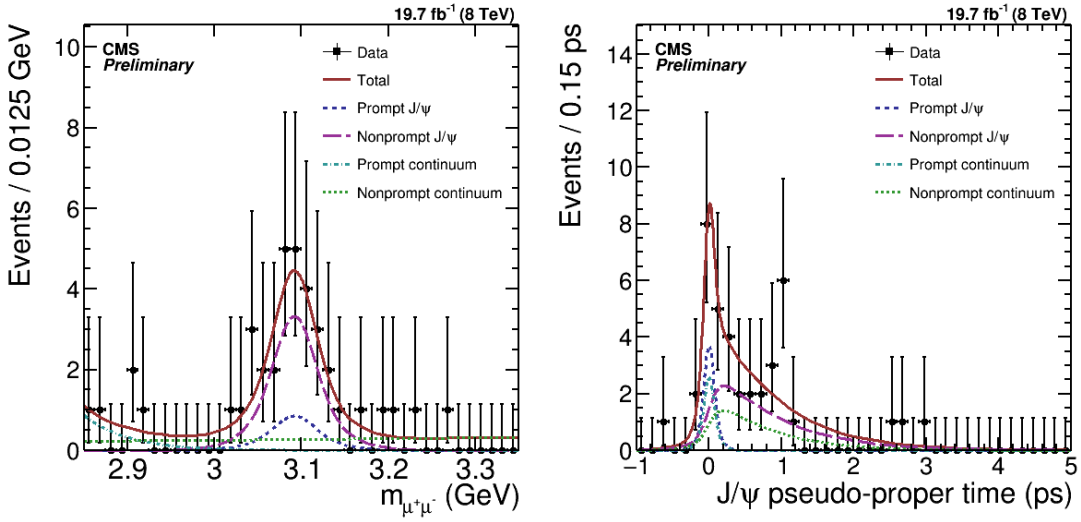

Figure 5.9: $Z \to e^+e^-$ and J/ψ mass and J/ψ lifetime distributions.

Table 5.2: Number of signal and background events of the fit for $Z + J/\psi$ and for the fit to the inclusive J/ψ sample.

	Efficiency Corrected Events (other than pileup cut)		
	$Z \to \mu^+\mu^-$	$Z \to e^+e^-$	Inclusive Sample
prompt J/ψ	45.3 ± 12.9	11.1 ± 7.3	260710 ± 1100
nonprompt J/ψ	68.4 ± 14.5	45.3 ± 12.9	114316 ± 859
prompt continuum	34.1 ± 11.1	12.3 ± 7.8	12747 ± 418
nonprompt continuum	9.6 ± 6.3	21.1 ± 12.3	29974 ± 470

Table 5.3: Signal events of $Z + J/\psi$. Uncertainty is statistical uncertainty on the overall number of events in each p_T bin combined with the error on the fraction of signal events from the fit.

	Prompt Yield		Non prompt Yield	
$p_T^{J/\psi}$ GeV	$Z \to \mu^+\mu^- + J/\psi$	$Z \to e^+e^- + J/\psi$	$Z \to \mu^+\mu^- + J/\psi$	$Z \to e^+e^- + J/\psi$
8.5-10	20.55 ± 10.2	0 ± 3.99	14.92 ± 8.83	11.53 ± 8.59
10-14	19.62 ± 8.2	5.56 ± 4.21	22.04 ± 8.19	10.67 ± 6.39
14-18	0.38 ± 6.67	0.88 ± 2.05	15.26 ± 6.07	6.95 ± 4.41
18-30	0 ± 1.14	4.68 ± 3.89	14.71 ± 5.07	15.15 ± 5.4
30-100	3.65 ± 3.31	0 ± 0.68	1.46 ± 1.9	1.05 ± 1.43

Chapter 6

Backgrounds

The primary backgrounds to this analysis are: dimuon continuum backgrounds, pileup, Z backgrounds, and DPS. I will discuss these backgrounds other than dimuon continuum backgrounds which were described in chapter 5, along with the negligible background of $Z \to \ell\ell J/\psi$. I use data-driven techniques to determine the pileup and Z background rate, while the estimation of DPS is based on experimental measurements from other analyses. The Z background effect is only relevant insofar as it differs from inclusive Z and associated Z production.

6.1 Pileup

There were on average 1.6×10^{11} protons per bunch in the machine. Increasing the number of protons per bunch increases the probability of interesting physics but at the cost of the chance that multiple proton collisions occur in the same bunch crossing. The number of pileup interactions per bunch crossing is shown in Fig. 6.1. Vertices are reconstructed by extrapolating the trajectories of particles based on information primarily from the tracker.

The pileup background for associated production is when a J/ψ and a Z boson come from different vertices in the same event. This background is reduced by the requirement that the Z vertex and J/ψ vertex must be within 0.5 cm in the z-direction, because unlike in associated production there is no correlation between the vertex positions of a pileup J/ψ. I determine the efficiency of this cut at rejecting pileup by examining the z-vertex

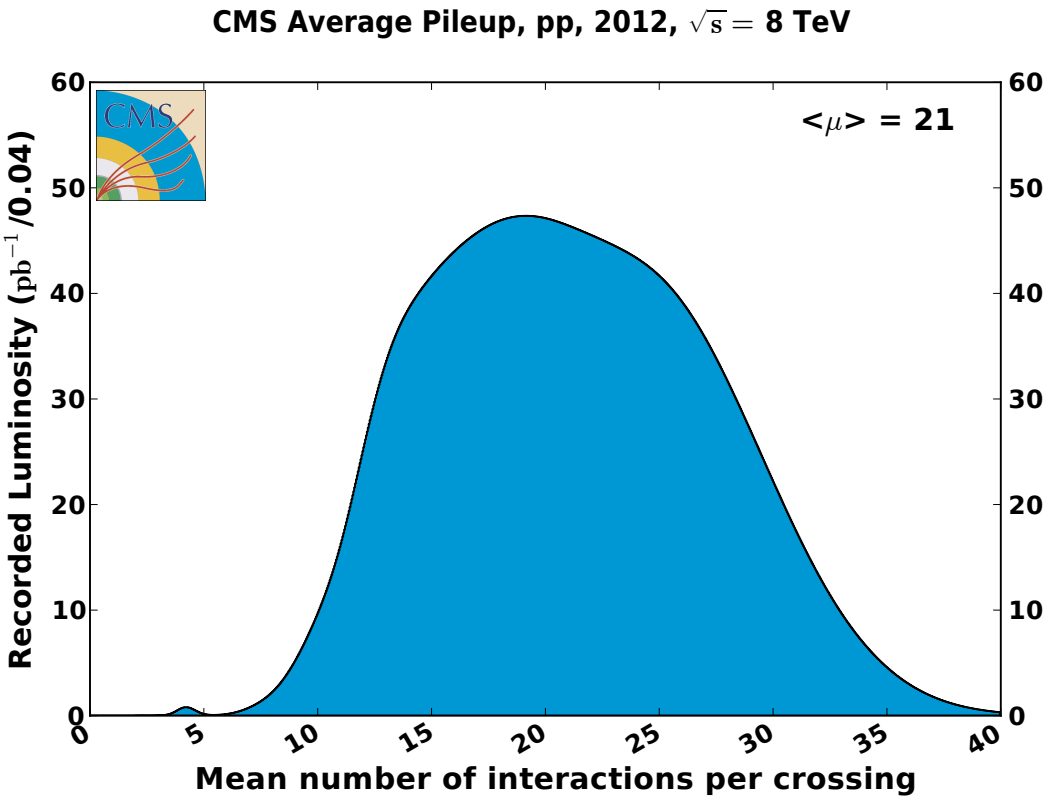

Figure 6.1: The average number of vertices in an event. There were on average 21 interactions per bunch crossing.

Table 6.1: Events with both a candidate Z and a candidate J/ψ from a region where the pileup cut was inverted such that the distance in the z-direction between the Z and J/ψ is greater than 3 cm. Uncertainty is statistical uncertainty on the overall number of events in each p_{T} bin combined with the error on the fraction of signal events from the fit. To determine the number of pileup events in the signal region we multiply these events by the scale factor of 8.77×10^{-2}.

	Prompt Yield		Nonprompt Yield	
$p_{\mathrm{T}}^{\mathrm{J}/\psi}$ GeV	$\mathrm{Z} \rightarrow \mu^+\mu^- +$ J/ψ	$\mathrm{Z} \rightarrow \mathrm{e}^+\mathrm{e}^- +$ J/ψ	$\mathrm{Z} \rightarrow \mu^+\mu^- +$ J/ψ	$\mathrm{Z} \rightarrow \mathrm{e}^+\mathrm{e}^- +$ J/ψ
8.5-10	19.49 ± 8.89	2.94 ± 4.67	0 ± 24.3	13.79 ± 8.85
10-14	13.49 ± 7.74	1.48 ± 4.29	19.11 ± 8.36	6.72 ± 5.24
14-18	1.88 ± 1.94	1.26 ± 2.09	0 ± 3.38	2.64 ± 2.65
18-30	0 ± 0.82	1.63 ± 1.64	1.64 ± 1.64	0 ± 1.06
30-100	0 ± 0	0 ± 0	0 ± 0	0 ± 0

distribution of inclusive J/ψ data relative to the primary vertex. The z-vertex position follows a Gaussian distribution with a standard deviation of 4.99 cm. To determine the probability that two vertices randomly sampled from a Gaussian with a standard deviation of σ_1 are within 0.5 cm of each other we could calculate the probability that the probability that a randomly chosen point is within 0.5 cm of the mean of a Gaussian with standard deviation $\sigma_2 = \sigma_1 * \sqrt{2}$. This procedure is applied to determine that only 5.78% of pileup J/ψ is kept after requiring the vertex position of the primary vertex (or equivalently the Z vertex) and J/ψ vertex to be within 0.5 cm, as shown in Fig. 6.2.

I determine the pileup background by requiring the J/ψ and the Z to be more than 3.0 cm away from each other in the z-direction to select a sample dominated by pileup. From this sample I estimate the number of pileup events in the signal region by scaling from the background region. The fraction of pileup events that are still included by the vertex position in the z-direction of less than 0.5 cm is 5.78% while the fraction with more than 3 cm is 66.0%, as shown in Fig. 6.2. The resulting scaling factor is 8.77×10^{-2}. The yield of associated production in the region where the z-position of the Z and J/ψ vertex is greater than 3 cm apart is determined by a 2D fit as described in Section 5.2, and is shown in Table 6.1, and in Fig. 6.3.

It is also possible to determine the expected pileup contribution theoretically [47].

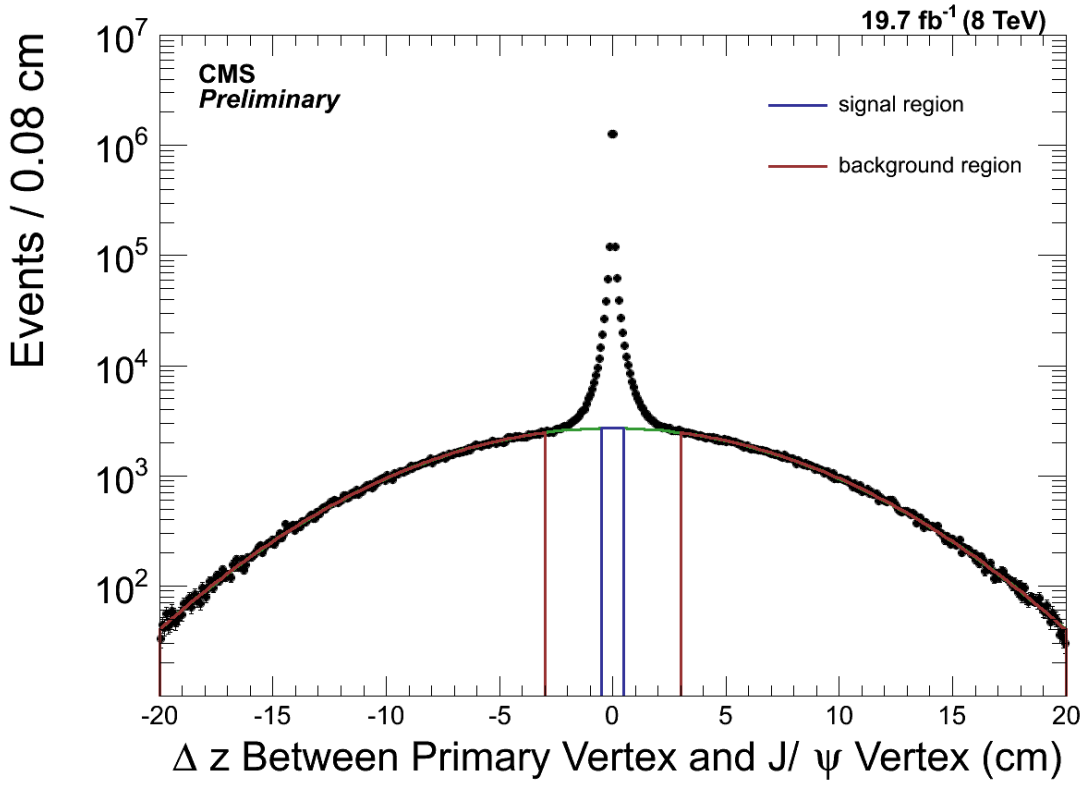

Figure 6.2: Difference between J/ψ vertex position in the z-direction and the z position of the primary vertex. The sharp peak at zero arises when a prompt J/ψ is from the primary vertex of the event. A Gaussian fit is performed in the region excluding ± 3 cm from the primary vertex to fit the distribution in Δz for pileup J/ψ. The Gaussian fit is centered at zero and has a standard deviation of 6.87 cm. This standard deviation is consistent with $\sqrt{2}\sigma_z$, where σ_z is the standard deviation of the distribution of primary vertex z-position which is about 5 cm. By extrapolating this fit into the signal region of ± 0.5 cm we find that only 5.78% of J/ψ from pileup are within 0.5 cm of the primary vertex.

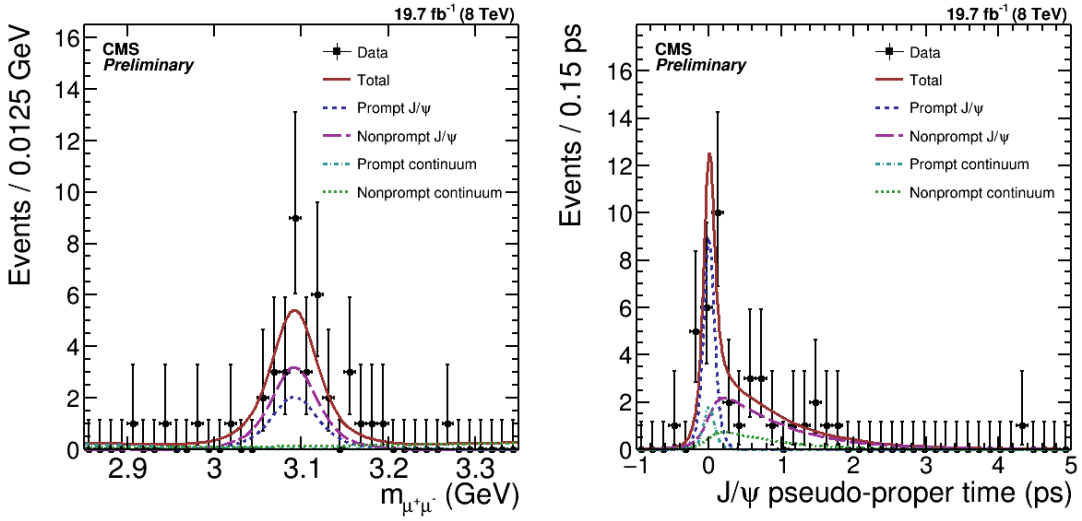

Figure 6.3: The 2D fit to the sample created by requiring the Z and J/ψ vertex positions to be greater than 3 cm apart. This fit is shown integrated over p_{T} and for $\mathrm{Z} \to \mathrm{e}^{+}\mathrm{e}^{-}$ and $\mathrm{Z} \to \mu^{+}\mu^{-}$ combined.

The probability that a J/ψ is produced in a given pp interaction is defined by:

$$P_{\mathrm{J}/\psi} = \frac{\sigma_{\mathrm{J}/\psi}}{\sigma_{\mathrm{inel}}} \tag{6.1}$$

where $P_{\mathrm{J}/\psi}$ is the probability of a J/ψ being produced in an interaction, $\sigma_{\mathrm{J}/\psi}$ is the J/ψ cross section and σ_{inel} is the inelastic cross section for pp interactions, determined to be (74.7 ± 1.7) mb by [65]. To find the probability of a pileup J/ψ given a Z I then use:

$$\mathrm{Prob}(\mathrm{J}/\psi_{\mathrm{pileup}}) = P_{\mathrm{J}/\psi}\langle\mu\rangle SF \tag{6.2}$$

where $\langle\mu\rangle$ is the average number of pileup vertices per bunch crossing, which was 21 for 8 TeV data, and SF is the scale factor for a vertex to survive the pileup cut, determined to be 5.78%. A comparison between the theoretical calculation and the data driven method is shown in Table 6.2.

Table 6.2: A comparison between two methods of determining the amount of pileup associated production in our data per Z. I use the data-driven method to determine the pileup contribution but present the theoretical calculation as a cross-check. This background is small compared to the signal in either case.

	Prompt $R_{J/\psi} \times 10^{-7}$		Nonprompt $R_{J/\psi} \times 10^{-7}$	
$p_T^{J/\psi}$ GeV	Data-driven	Calculation	Data-driven	Calculation
8.5-10	1.7 ± 0.8	1.93 ± 0.19	1.04 ± 2.0	0.83 ± 0.08
10-14	1.1 ± 0.7	1.44 ± 0.12	1.96 ± 0.75	0.80 ± 0.07
14-18	0.24 ± 0.2	0.28 ± 0.02	0.20 ± 0.33	0.34 ± 0.02
18-30	0.12 ± 0.14	0.12 ± 0.0087	0.12 ± 0.14	0.14 ± 0.01
30-100	0 ± 0	0.012 ± 0.001	0 ± 0	0.02 ± 0.002

6.2 Double Parton Scattering

Double parton scattering (DPS) describes the process in which multiple distinct partons interact in the same pp collision. This process depends on the size of the proton and transverse parton correlations, but it is assumed to be independent of the scattering process [47, 66].

The Prob(Z + J/ψ|Z) due to DPS is calculated by:

$$\text{Prob}(\text{Z} + \text{J}/\psi|\text{Z}) = m\frac{\sigma_{\text{J}/\psi}}{\sigma_{eff}}, \tag{6.3}$$

where $\sigma_{J/\psi}$ is the inclusive J/ψ cross section and $\sigma_{eff} = 20.7 \pm 0.8$ (stat.) ± 6.6 (syst.) mb is the effective cross section for DPS, determined by [3], and m is the symmetry factor, equal to 1 if the processes are distinct and $\frac{1}{2}$ if the processes are identical. The effective cross section was determined by analyzing p p $\rightarrow$W +2-jet events where the vector sum of the p_T of the 2 jets for events arising from DPS is zero, while this is not true for the Single Parton Scattering (SPS) events. Note that a similar analysis by ATLAS yields a smaller value of $\sigma_{eff} = 15 \pm 3$ (stat.) $^{+5}_{-3}$ (syst.) mb [19]. While using double J/ψ or J/ψ +Υ final states, much lower values of $\sigma_{eff} = 2 - 5$ mb have been obtained, for $p\bar{p}$ collisions at lower energies [67, 68]. Figure 6.4 shows the dependence of σ_{eff} on energy and its values determined using many different final states.

We determine the prompt $\sigma_{J/\psi}$ for our selection criteria to be 23 nb [69] and 12 nb for

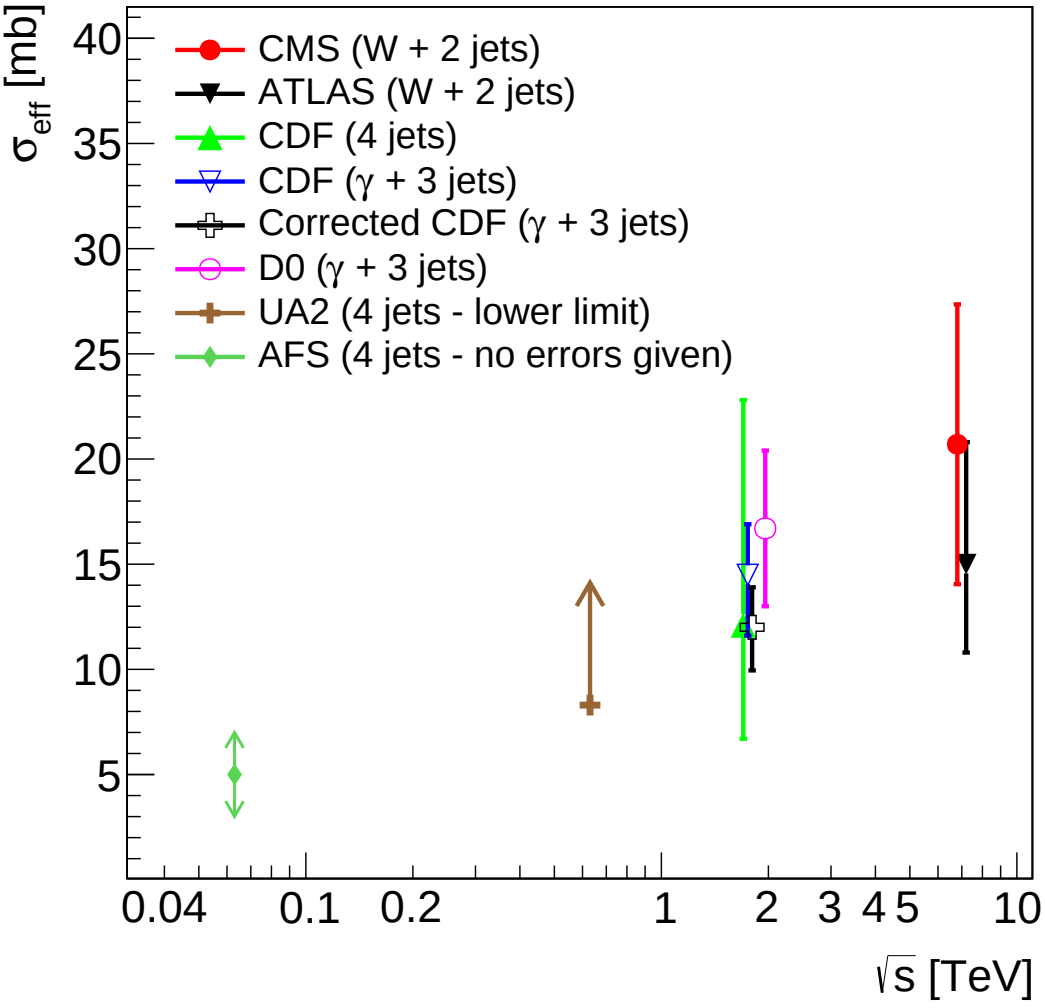

Figure 6.4: A comparison of σ_{eff} at different center-of-mass energies using different methods to extract the effective cross section [3]. Data are taken from Refs. [19–24].

Table 6.3: The DPS contribution to the Prob(Z + J/ψ $\rightarrow$ $\mu^+\mu^-$|Z) for each p_{T} bin. Uncertainty is from the uncertainty in σ_{eff} = 20.7 $\pm$ 0.8 (stat.) $\pm$6.6 (syst.) mb Ref. [3].

$p_{\mathrm{T}}^{\mathrm{J}/\psi}$ GeV	Prompt DPS Ratio	Nonprompt DPS Ratio
8.5-10	5.7 ± 1.9	2.5 ± 0.8
10-14	4.3 ± 1.4	2.4 ± 0.8
14-18	0.8 ± 0.3	1.0 ± 0.3
18-30	0.4 ± 0.1	0.4 ± 0.1
30-100	0.04 ± 0.01	0.07 ± 0.02

nonprompt J/ψ. Since the 8 TeV results in Ref. [69] exclude a part of the rapidity range our measurements require, we complement them with the 7 TeV results which cover the entire rapidity range we need. We apply a small correction to the 7 TeV results using the prescription in Ref. [70], where $f(\sqrt{s}) = A \cdot (\sqrt{s/s_0})^b$ where $A = 124 \pm 9$ nb, $b = 0.60 \pm 0.06$ and $\sqrt{s_0} = 1$ TeV. Resulting background due to DPS in the prompt Prob(Z + J/ψ $\rightarrow$ $\mu^+\mu^-$|Z) is $(11.2 \pm 3.6) \times 10^{-7}$ and for nonprompt, $(6.0 \pm 1.9) \times 10^{-7}$. The DPS background in bins of p_{T} is shown in Table 6.3.

6.3 Z Background

The Z is a high mass object, and our selection requirements reconstruct it from the clean decays of Z $\rightarrow$ $\mu^+\mu^-$ and Z $\rightarrow$ e^+e^-. The background under the Z mass peak due primarily to Drell-Yan processes (which we do not consider part of our signal) is small. Additionally, unless the background rate differs between associated and inclusive production we expect this background rate to cancel in the ratio.

The dilepton mass distributions shown in Figure 6.5 indicate that the background under the Z peak is about 1% of the signal. I estimate its effect on our measurements using a data-driven technique that measures the background in the Z sideband regions and interpolates into the Z mass signal region. The high sideband is when the dilepton mass of a Z candidate is greater than 150 GeV and less than 300 GeV. The low sideband is when the mass is between 40 and 50 GeV (40 and 45 GeV) for a di-electron (di-muon) pair. The difference in the low sideband is chosen because the efficiency of

low p_{T} muons and electrons differs. The signal region is defined to be between 80 and 100 GeV. Assuming that the J/ψ production rate by these background events stays the same for different background Z candidate masses, we can calculate the scale factors between the numbers of J/ψ's due to the background in the signal and sideband regions from the inclusive Z yields in the same Z candidate mass ranges. In order to find the scale factors, we fit the inclusive di-electron and di-muon Z candidate mass distributions with an analytical function of the form,

$$F(m_{\ell\ell}) = \mathrm{erf}\left(\frac{\alpha - m_{\ell\ell}}{\delta}\right)\exp(-\gamma m_{\ell\ell}), \tag{6.4}$$

where $m_{\ell\ell}$ is the mass of the Z candidates, α represents the 50% point in the turn-on curve, δ determines how quickly the turn on happens, and γ is the exponential slope of the fall of the background.

Figure 6.5 shows these distributions and the fitting functions. The fits match the numbers of events within 10% for various mass intervals, which is sufficiently accurate for calculating the scaling factors, even though they don't match the data points within the statistical precision of the inclusive Z data we use. The scale factors are the ratios of the integrals of the fitted functions in the appropriate mass regions, and are 1.38 (1.45) for the low (high) electron pairs and 2.43 (1.66) for the low (high) muon pairs.

Figure 6.6 shows the J/ψ candidate mass and their lifetime distributions for the Z sideband events. Using the same 2D fit that we use for the Z signal samples, we obtain the J/ψ yield in the Z sideband. The figure also shows the projection of the fitted yields of the prompt and nonprompt J/ψ as well as the continuum backgrounds. The resulting numbers of J/ψ's in the signal and sideband regions, estimates of the background contributions in the signal region, and the fraction of the background in the signal region, are presented in Table 6.4.

6.4 Four Lepton Mass Background

Another potential source of background comes from $\mathrm{Z} \to 4\ell$ decays, whose branching ratio has been measured to be $(3.30\pm0.31)\times10^{-6}$ [42]. Since the two results on which this PDG listing is based exclude the phase space of this decay where the lighter dilepton

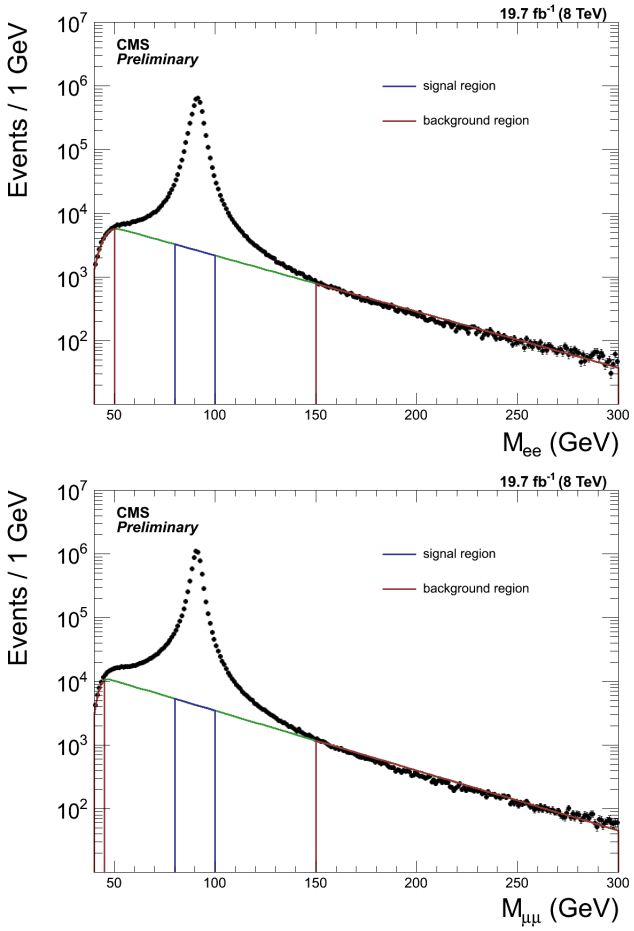

Figure 6.5: Inclusive Z candidate mass distribution when (a) $Z \to e^+e^-$ and (b) $Z \to \mu^+\mu^-$. The curves in the plots are the results of the fit described in the text.

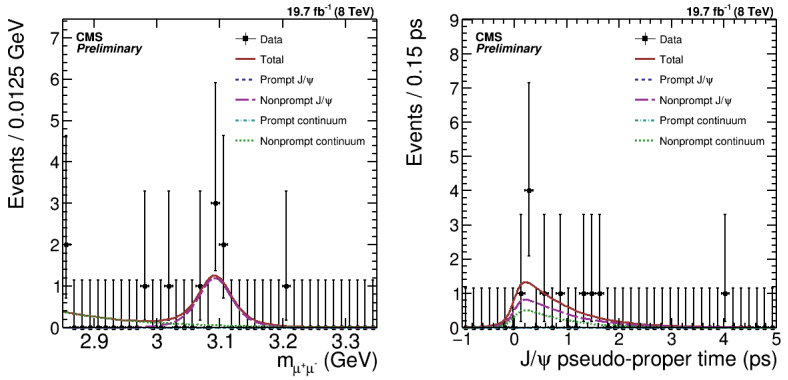

Figure 6.6: The distributions of the J/ψ candidate mass (left) and their lifetime (right) for both low and high mass Z sideband events.

Table 6.4: J/ψ yields from Z sidebands.

	Low Sideband	High Sideband	Signal Region	Background Estimate	Background fraction (%)
Z $\rightarrow e^+e^-$					
Inclusive	4.065×10^4	3.526×10^4	4.637×10^6	5.366×10^4	1.16
+ Prompt J/ψ	1.55±1.55	0.0±1.83	11.12±7.31	1.07±2.40	9.64
+ Nonprompt J/ψ	0.0±0.96	6.29±3.78	45.34±12.86	4.56±3.41	10.1
Z $\rightarrow \mu^+\mu^-$					
Inclusive	3.934×10^4	4.845×10^4	6.935×10^6	8.81×10^4	1.27
+ Prompt J/ψ	0.0±0.69	0±1.15	44.20±15.12	0±1.79	0.0
+ Nonprompt J/ψ	0.0±0.74	1.55±1.93	68.40±14.52	1.29±2.5	1.89

pairs have masses less than 4 or 5 GeV, this ratio does not have a direct implication on the background in our sample.

The Z $\rightarrow \ell\ell$J/ψ reconstructed mass is expected to peak at the Z mass peak of 91.2 GeV [42]. I determine if this occurs for our selection criteria, except with the requirement that the Z mass is between 40 and 300 GeV as opposed to 80 and 100 GeV. There is no evidence of a Z mass peak in the 4 lepton mass distribution with our selection criteria, as shown in Figures 6.7 and 6.8.

Figure 6.9 shows the mass and lifetime distributions of the J/ψ candidate when the mass of the Z decay candidate falls between 80 and 100 GeV and the mass of all 4

leptons also falls in this interval. This sample contains all the events in our signal sample which are consistent with the Z $\rightarrow \ell\ell$J/ψ decay. The result of the 2D fit is consistent with no prompt J/ψ with an error of 5.8 efficiency corrected events for the Z $\rightarrow \mu^+\mu^-$ case and 1.1 events for the Z $\rightarrow$e$^+$e$^-$ case. It is important to note that this fit is an overestimate of the potential 4 lepton background because it assumes that all events which pass the selection criteria are from Z $\rightarrow \ell\ell$J/ψ but this assumption is inconsistent with Figures 6.7 and 6.8. Consequently, I consider this background to be negligible.

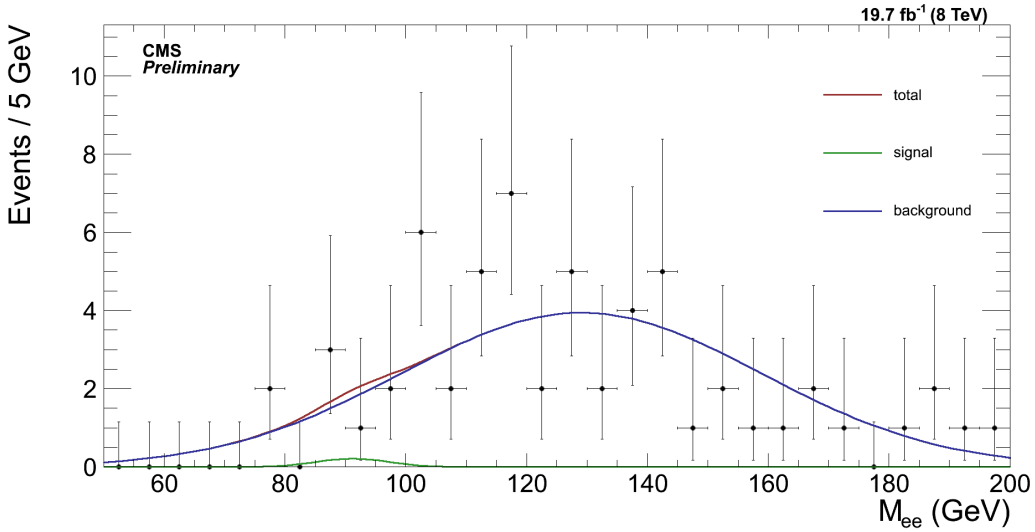

Figure 6.7: The four-lepton mass for Z $\rightarrow$ e$^+$e$^-$ with our selection criteria except a Z mass requirement of 40 to 300 GeV. Only 0.57 events are consistent with a $M_{\ell\ell J/\psi}$ from the Z. This is determined from fitting the distribution with two Gaussians, with the mean and width of one Gaussian constrained to be near the inclusive Z mass and width.

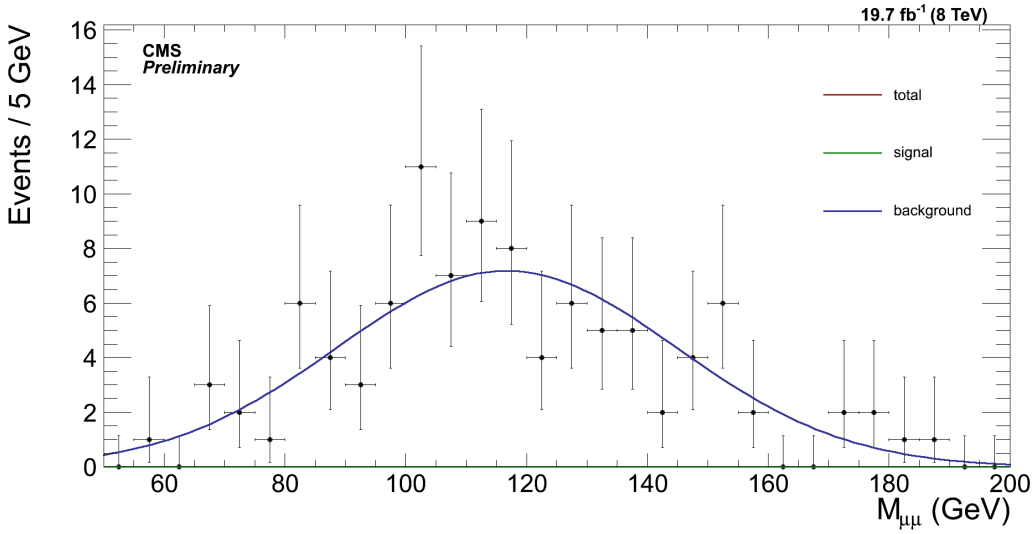

Figure 6.8: The four-lepton mass for Z $\rightarrow \mu^+\mu^-$ with our selection criteria except a Z mass requirement of 40 to 300 GeV. Zero events are consistent with a $M_{\ell\ell J/\psi}$ from the Z. This is determined from fitting the distribution with two Gaussians, with the mean and width of one Gaussian constrained to be near the inclusive Z mass and width.

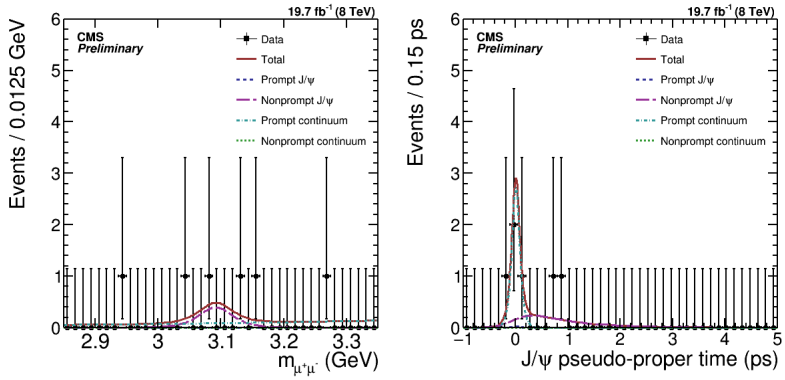

Figure 6.9: The distributions of the four-lepton mass for our signal candidate events.

Chapter 7

Systematic Uncertainties

The three dominant sources of systematic uncertainty for this measurement are: the unknown polarization of the J/ψ in associated production; the potential differences between inclusive and associated J/ψ shapes; the uncertainty in determining the differences in efficiency between associated and inclusive Z production. The polarization uncertainty is the largest uncertainty, as differences in J/ψ polarization can have a large effect on the efficiency in the reconstruction of the J/ψ. Overall this measurement is dominated by statistical uncertainty.

7.1 Polarization Uncertainty

The differences in efficiency between the different polarization scenarios is discussed in Section 4.4. I evaluate this uncertainty by repeating the analysis procedure but assuming the different efficiencies found with the differing polarization extremes. For nonprompt J/ψ, the b hadron is a spin 0 particle, so its polarization will have a diluted effect on the J/ψ polarization in the lab frame. Since the polarization measurement of nonprompt inclusive J/ψ is consistent with zero [71], we constrain the polarization of the nonprompt J/ψ to be within 10% of the unpolarized value, following the procedure used in Ref. [6]. The resulting differences in yields for associated production are shown in Tables 7.1 and 7.2.

Table 7.1: Signal events of associated prompt J/ψ under different polarization extremes.

	Prompt Yield			Uncertainty (%)
$p_{\mathrm{T}}^{\mathrm{J}/\psi}$ GeV	Unpolarized $\lambda = 0$	Longitudinal $\lambda = -1$	Transverse $\lambda = 1$	Polarized / Unpolarized
8.5-10	20.6	14.5	26.0	$\pm^{26.4}_{29.3}$
10-14	25.2	18.7	30.6	$\pm^{21.4}_{25.7}$
14-18	1.26	1.05	1.40	$\pm^{11.1}_{17.0}$
18-30	4.70	3.9	5.22	$\pm^{11.7}_{16.8}$
30-100	3.65	3.2	3.96	$\pm^{8.6}_{13.5}$
8.5-100	55.3	41.3	67.1	$\pm^{21.3}_{25.3}$

Table 7.2: Signal events of associated nonprompt J/ψ under different polarization extremes.

	Nonprompt Yield			Uncertainty (%)
$p_{\mathrm{T}}^{\mathrm{J}/\psi}$ GeV	Unpolarized $\lambda = 0$	Longitudinal $\lambda = -0.1$	Transverse $\lambda = 0.1$	Polarized / Unpolarized
8.5-10	26.5	25.7	27.1	$^{+2.4}_{-2.8}$
10-14	32.7	31.9	33.5	$^{+2.3}_{-2.5}$
14-18	22.2	21.7	22.6	$^{+1.8}_{-2.3}$
18-30	29.9	29.3	30.3	$^{+1.5}_{-1.8}$
30-100	2.5	2.5	2.5	$^{+1.2}_{-1.2}$
8.5-100	113.7	113.1	116.1	$^{+2.0}_{-2.3}$

7.2 Fit Uncertainty

I rely on the inclusive J/ψ sample in order to determine the shape of the signal for associated J/ψ. This assumes that the shape does not change between associated or inclusive production for a given bin of J/ψ p_{T}. However, because the J/ψ polarization could be different between associated and inclusive production, the shapes could be slightly different. We evaluate the difference by determining the shape parameters assuming different extreme polarization scenarios. This study indicated that the maximum change in resolution parameters due to differing polarizations was about 10%. I repeated the analysis with the resolution parameters for associated production increased by 10%, which led to a change of 4% for prompt production and 2% for nonprompt production yield. The difference in resolution for the primary vertex between associated production and inclusive J/ψ production has a negligible impact on this measurement, in part because for inclusive J/ψ production the resolution on the primary vertex is better than the resolution for the dimuon vertex for nonprompt J/ψ, and also because the resolution on the primary vertex for inclusive Z production and for associated Z production is negligibly different for our measurement.

7.3 Z Efficiency Uncertainty

The efficiency could be different between inclusive Z production and associated Z production because the p_{T} spectrum of the Z is harder for associated production. I determine the efficiency as a function of Z p_{T} with Drell-Yan plus Jets to $\ell^+\ell^-$ Madgraph MC [61]. Figure 7.1 shows the dependence of the Z detection efficiency on the p_{T} of the Z candidate. The efficiency is the smallest at zero Z p_{T}. When this is convolved with the p_{T} dependence of the Z production in the associated production of Z and J/ψ and inclusive Z production, I find that the efficiency is higher for the associated production for the Z $\rightarrow$e$^+$e$^-$ and Z $\rightarrow \mu^+\mu^-$ channels where the uncertainty is due to the statistical uncertainties in the associated production data. This is due to the higher p_{T} of the Z in associated production.

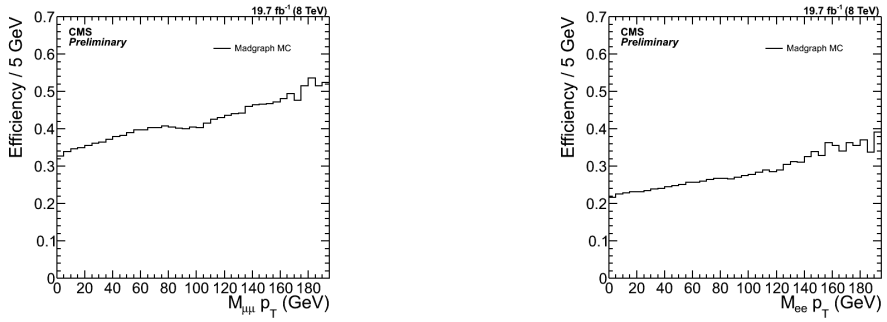

Figure 7.1: Dependence of the Z $\rightarrow \ell\ \ell$ detection efficiency on p_{T}.

The average efficiency of the Z summed over p_{T} is given by:

$$\epsilon = N \sum_{i=0}^{N_{\mathrm{bins}}} \epsilon_i / N_i \tag{7.1}$$

where ϵ is the overall efficiency of the Z weighted by its p_{T} distribution, ϵ_i is the efficiency as determined from MC ($\frac{N_{\mathrm{reco}}}{N_{\mathrm{gen}}}$), N_i is the number of data events in the given p_{T} bin, and N is the total number of events. I then calculate the ratio of $\epsilon_{\mathrm{associated}}$ and $\epsilon_{\mathrm{inclusive}}$. By propagating the uncertainty, we find that:

$$\sigma^2 = \sum_{i=0}^{N_{\mathrm{bins}}} [(Y - \frac{N_{\mathrm{associated}}}{\epsilon_i}) \frac{\sigma_i}{Y^2}]^2 \tag{7.2}$$

where σ^2 is the squared uncertainty on $\epsilon_{\mathrm{associated}}$, $N_{\mathrm{associated}}$ is the number of associated events, σ_i is the statistical uncertainty for a given p_{T} bin, and Y is the yield of the data, $\sum N_i/\epsilon_i$. I correct our measurements for this effect and assign the uncertainties as the systematic uncertainties from this source. The ratios of the efficiencies and their uncertainties are shown in Table 7.3.

7.4 J/ψ Efficiency Uncertainty

I generated about a million inclusive J/ψ MC events, so the uncertainty due to MC statistics is negligible. Because the fit is to an unbinned dataset whereby the efficiency is applied to each associated J/ψ event, there is no systematic uncertainty associated

Table 7.3: The ratio of efficiency for Z in associated production with a J/ψ as opposed to inclusive Z. Uncertainties are determined by propagating the statistical uncertainty in each bin of Z p_{T} for associated production.

$p_{\mathrm{T}}^{\mathrm{J}/\psi}$ GeV	Z $\rightarrow \mu^+\mu^-$	Z $\rightarrow$e$^+$e$^-$
8.5-10	1.055±0.019	1.066±0.043
10-14	1.039±0.013	1.079±0.037
14-18	1.100±0.016	1.057±0.035
18-30	1.103±0.019	1.138±0.044
30-100	1.188±0.089	1.208±0.083

with the harder p_{T} spectrum for associated J/ψ as opposed to inclusive J/ψ. There is a 1.5% uncertainty associated with measuring the scale factor with the tag-and-probe method described in Section 4.4, as recommended by the CMS Muon group [72].

Chapter 8

Results

In this chapter I present the results of our measurement of associated production of Z and J/ψ with 19.7 fb^{-1} of 8 TeV data collected with the CMS detector at the LHC. I compare our measurement to the similar measurement made by the ATLAS collaboration and the theoretical predictions. I also present the statistical significance of our observation.

8.1 Results

There were 6.94 million inclusive Z $\rightarrow\mu^+\mu^-$ and 4.64 million inclusive Z $\rightarrow$e$^+$e$^-$ events that passed our selection criteria. If we subtract the backgrounds from the pileup and Z background, and correct for the differences in efficiency between the associated and inclusive Z, the measured Prob(Z $\rightarrow\mu^+\mu^-$ + Prompt J/ψ $\rightarrow$ $\mu^+\mu^-$|Z $\rightarrow\mu^+\mu^-$) is (56.8 $\pm$ 20.9) $\times$10^{-7}, and for nonprompt J/ψ, it is (97.9 $\pm$ 22.3) $\times$10^{-7}. The Prob(Z $\rightarrow$e$^+$e$^-$ + Prompt J/ψ $\rightarrow$ $\mu^+\mu^-$|Z $\rightarrow$e$^+$e$^-$) is (19.2 $\pm$ 15.3) $\times$10^{-7}, and for nonprompt J/ψ is (85.8 $\pm$ 29.3) $\times$10^{-7}. The difference between Z $\rightarrow$e$^+$e$^-$ and Z $\rightarrow\mu^+\mu^-$ is about 1.5σ. Although this difference is not all that unlikely, we examined potential explanations for it. The resolution and average position of the Z vertex for the electron and muon decays is negligibly different, and there are not significantly more associated Z $\rightarrow$e$^+$e$^-$ events which fail the z-direction pileup selection criteria, so this does not explain the discrepancy. The only difference in analysis procedure in terms of the J/ψ between Z $\rightarrow$e$^+$e$^-$ and Z $\rightarrow\mu^+\mu^-$ events is the exclusion of the muons which form the Z $\rightarrow\mu^+\mu^-$ candidate from potential J/ψ candidate muons. However, this is a negligible effect and

Table 8.1: Rates for associated production of a Z and J/ψ relative to a Z ($\times 10^{-7}$) for both prompt and nonprompt J/ψ. Uncertainties are statistical.

	Prompt		Nonprompt	
$p_{\mathrm{T}}^{\mathrm{J}/\psi}$ GeV	Z $\to\mu^+\mu^-$	Z $\to$e$^+$e$^-$	Z $\to\mu^+\mu^-$	Z $\to$e$^+$e$^-$
8.5-10	26.1±14.2	0±8.2	22.0±13.4	22.5±18.9
10-14	25.9±11.6	11.0±8.7	30.7±12.4	18.3±14.4
14-18	0.3±8.9	1.6±4.5	22.4±8.9	12.0±10.6
18-30	0.0±1.8	6.6±8.1	20.5±8.1	31.4±12.8
30-100	4.5±4.4	0±1.5	2.3±4.1	1.5±4.2
total	56.8±20.9	19.2±15.3	97.9±22.2	85.8±29.3

Table 8.2: Differential rates ($\times 10^{-7}$/ GeV) for pp $\to$ Z $\to \ell\ell$ + J/$\psi \to \mu^+\mu^-$ relative to pp $\to$ Z $\to \ell\ell$ both prompt and nonprompt. Uncertainties are statistical, systematic and due to the unknown polarization of the J/ψ.

$p_{\mathrm{T}}^{\mathrm{J}/\psi}$ GeV	Prompt Prob(Z + J/ψ|Z)	NP Prob(Z + J/ψ|Z)
8.5-10	$10.4 \pm 6.1 \pm 0.5^{+2.8}_{-3.1}$	$14.8 \pm 7.4 \pm 0.6^{+0.4}_{-0.4}$
10-14	$4.9 \pm 1.9 \pm 0.2^{+1.1}_{-1.3}$	$6.4 \pm 2.4 \pm 0.2^{+0.2}_{-0.2}$
14-18	$0.2 \pm 1.4 \pm 0.01^{+0.02}_{-0.03}$	$4.6 \pm 1.7 \pm 0.1^{+0.1}_{-0.1}$
18-30	$0.2 \pm 0.3 \pm 0.01^{+0.03}_{-0.04}$	$2.1 \pm 0.59 \pm 0.07^{+0.03}_{-0.04}$
30-100	$0.038 \pm 0.039 \pm 0.004^{+0.003}_{-0.005}$	$0.029 \pm 0.043 \pm 0.003^{+0.0003}_{-0.0003}$

would anyway drive the associated Z $\to\mu^+\mu^-$ down relative to Z $\to$e$^+$e$^-$. There is also no compelling physics theory to explain the difference, so it is most likely due to a statistical fluctuation. Taking the average of the muon and electron channels by summing the associate productions of the two channels, the Prob(Z $\to\ell$ ℓ + Prompt J/$\psi \to \mu^+\mu^-$|Z $\to\ell$ ℓ) is (41.5 ± 12.0 (stat) ± 1.8 (syst) ± 10.5 (pol)) $\times 10^{-7}$, and for nonprompt J/ψ is (93.0 ± 14.5 (stat) ± 2.5 (syst) ± 2.0 (pol)) $\times 10^{-7}$. The uncertainties come from statistics, systematics and the unknown polarization of the J/ψ.

The $R_{\mathrm{J}/\psi}$ after subtracting the backgrounds and adjusting for the efficiency are shown in Table 8.1 for both Z $\to$ e$^+$e$^-$ and for Z $\to \mu^+\mu^-$. The differential rates combining Z $\to \mu^+\mu^-$ and Z $\to$ e$^+$e$^-$ are shown in Table 8.2. The results are also shown in Figure 8.1.

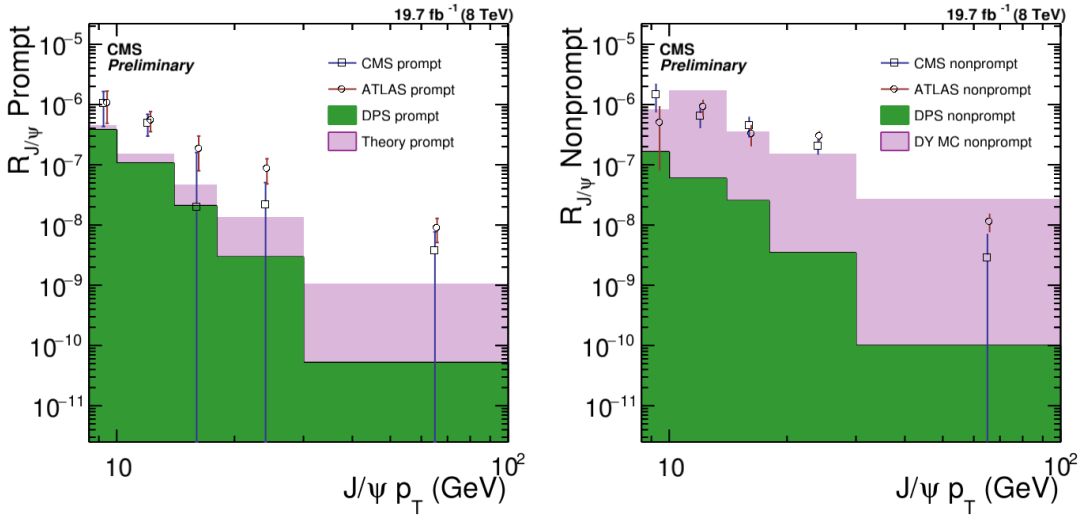

Figure 8.1: Differential rates for Prob(Z $\to \ell\ \ell$ + J/$\psi \to \mu^+\mu^-$|Z $\to \ell\ \ell$) as a function of p_{T}. The nonprompt MC was determined by running the analysis procedure on the DYJetsToLL M-50 TuneZ2Star Madgraph MC (the prompt J/ψ associated production of this MC is consistent with 0).

8.2 Theoretical Comparison

Table 8.3 lists the theoretical predictions made by the authors of Ref. [4, 5] on the product of the cross section for p p $\to$ J/ψ +Z process and the decay branching fractions, Br(J/$\psi \to \mu^+\mu^-$) as well as Br(Z $\to \ell^+\ell^-$) in bins of J/ψ p_{T} [73] at LHC with $\sqrt{s} = 8$ TeV. They assumed that Br(J/$\psi \to \mu^+\mu^-$) =5.93% and Br(Z $\to \ell^+\ell^-$) =6.729%. They used the experimental selection criteria shown in Table 8.4 on the final state particles which are the same as used in Ref. [4, 5]. The sum of columns 1 and 3 gives LO cross sections, while the sum of columns 2 and 4 gives the NLO cross section results (including the LO). Columns 1 and 2 represent the color-octet contribution, while columns 3 and 4 represent the color-singlet contribution. NLO results are larger than LO. The theoretical expectation for the Prob(Z+J/ψ|Z) of 6.06×10^{-7} is obtained by dividing the NLO cross section by the fiducial cross section of the Z $\to \ell\ell$, measured to be 0.41 nb by [74]. The theoretical expectation is about a factor of 5 lower than our experimental measurement if we assume a DPS σ_{eff} of 20.7 mb, but the statistical and polarization uncertainties of our measurement are too large to justify quantitative conclusions. Our results are in

better agreement with the COM than the CSM in the sense that our results are higher than both the COM and the CSM, and predictions from the COM are much higher than for the CSM only.

Table 8.3: Cross sections Ref. [4, 5].

$p_{\mathrm{T}}^{\mathrm{J}/\psi}$ (GeV)	${}^3S_1^{(8)}$ LO(fb)	${}^3S_1^{(8)}$ NLO(fb)	${}^3S_1^{(1)}$ LO(fb)	${}^3S_1^{(1)}$ NLO(fb)
$8.5 \sim 10$	0.0230	0.0857	0.01065	0.00923
$10 \sim 14$	0.0403	0.1419	0.01567	0.01493
$14 \sim 18$	0.0231	0.0783	0.00702	0.005783
$18 \sim 30$	0.0297	0.0964	0.00627	0.00755
$30 \sim 100$	0.0178	0.0543	0.00145	0.00308

Table 8.4: Requirements used in Ref. [4, 5]

J/ψ: $p_{\mathrm{T}} > 8.5\,\mathrm{GeV}$
J/ψ rapidity: $\lvert y\rvert < 2.1$
Muon from J/ψ: $\lvert\eta\rvert < 2.5$
Higher p_{T} lepton from Z: $p_{\mathrm{T}} > 25\,\mathrm{GeV}$
Lower p_{T} lepton from Z: $p_{\mathrm{T}} > 15\,\mathrm{GeV}$
Leptons from Z: $\lvert\eta\rvert < 2.5$
Mass of Z: $\lvert m_{\ell\ell} - 90.2\rvert < 10\,\mathrm{GeV}$

In response to the disagreement between the measurement made by ATLAS and theoretical predictions [6], theorists have proposed that σ_{eff} used to determine the DPS contribution should be different. Perhaps because it is process dependent we cannot use the value extracted from processes which are dominated by gluons for processes which are dominated by quarks [75]. Events from DPS, or pileup, are expected to be uniform in $\Delta\phi$ between the Z and the J/ψ, while SPS events are expected to be predominantly back-to-back. Table 8.6 shows the $R_{\mathrm{J}/\psi}$ with the additional selection criteria that $|\Delta\phi| \leq \pi/3$, a selection which eliminates most of the SPS signal. The distribution of $\Delta\phi$ between the Z and J/ψ, shown in Figure 8.2, is expected to peak at π for SPS because SPS is expected to be back-to-back, while for DPS it is expected to be uniform.

For SPS, we expect the p_{T} of the Z and the J/ψ to be balanced, although this balance

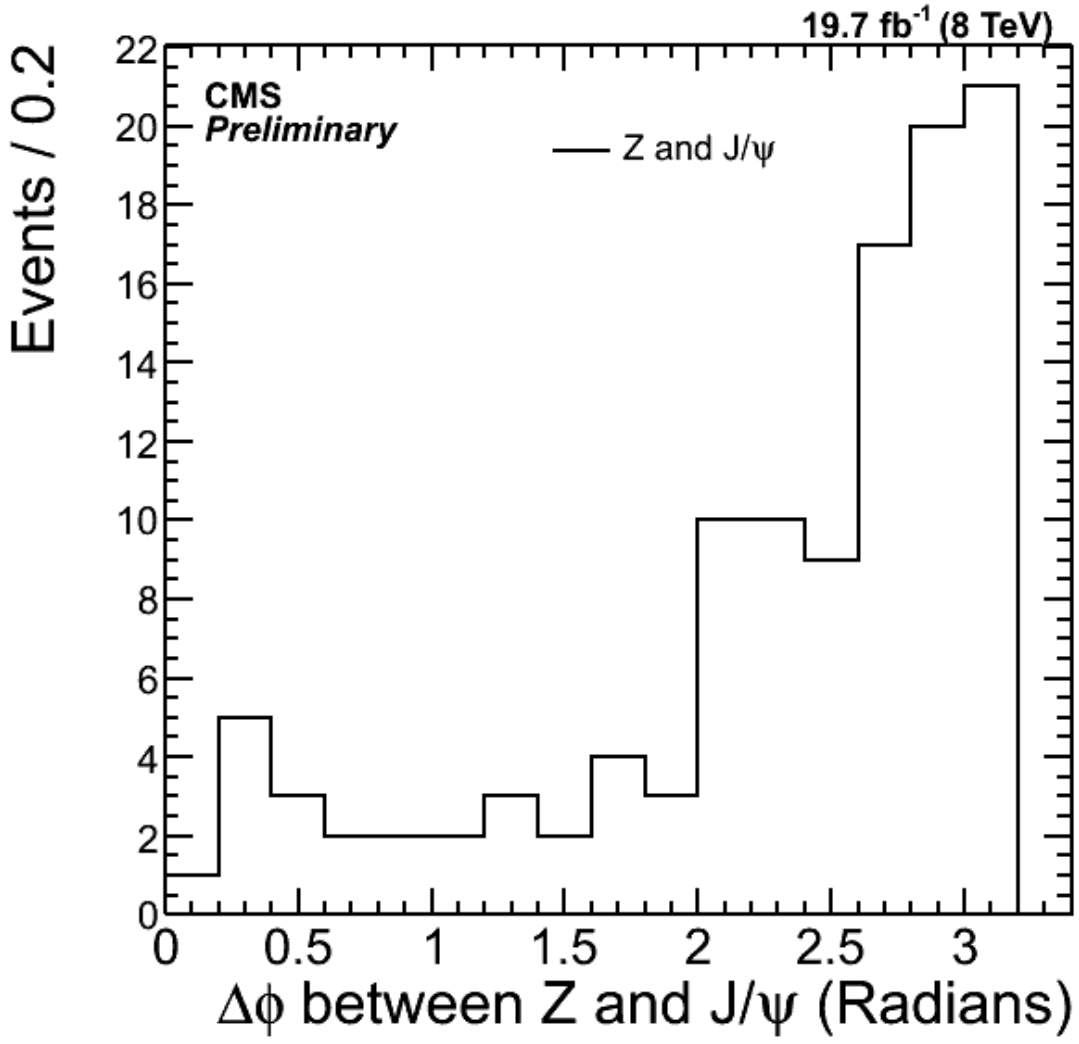

Figure 8.2: The $\Delta\phi$ between the Z and J/ψ candidates. This plot includes nonprompt and continuum backgrounds.

Table 8.5: Comparison of signal between CMS and theoretical predictions from Ref. [4]. In the 5 p_{T} regions, the results are differential rate, dR/dp_{T} in $\times 10^{-7}$/ GeV while the last line is the integral, $R(8.5\,\mathrm{GeV} < p_{\mathrm{T}} < 100\,\mathrm{GeV})$ in $\times 10^{-7}$. The first uncertainty is the statistical, the 2nd, combined systematic and the last, systematic uncertainty due to the unknown polarization of the J/ψ. DPS is calculated under the assumptions described in Section 6.2.

Prompt Prob(Z + J/$\psi \to \mu^+\mu^-$|Z)

p_{T} range (GeV)	CMS (SPS + DPS)	DPS ($\sigma_{eff} = 20.7\,\mathrm{mb}$)	Theory
$8.5 < p_{\mathrm{T}} < 10$	$10.4 \pm 6.1 \pm 0.5 \pm 3.1$	3.8 ± 1.3	0.77 ± 0.08
$10 < p_{\mathrm{T}} < 14$	$4.9 \pm 1.9 \pm 0.2 \pm 1.3$	1.1 ± 0.4	0.48 ± 0.05
$14 < p_{\mathrm{T}} < 18$	$0.2 \pm 1.4 \pm 0.01 \pm 0.03$	0.2 ± 0.07	0.26 ± 0.03
$18 < p_{\mathrm{T}} < 30$	$0.2 \pm 0.3 \pm 0.01 \pm 0.04$	0.03 ± 0.01	0.11 ± 0.01
$30 < p_{\mathrm{T}} < 100$	$0.04 \pm 0.04 \pm 0.004 \pm 0.01$	0.0005 ± 0.0002	0.01 ± 0.001
Integrated	$41.5 \pm 12.0 \pm 1.8 \pm 10.5$	11.2 ± 3.7	6.1 ± 0.6

will be smeared somewhat in the case of nonprompt J/ψ, as the J/ψ does not have the same p_{T} as the b hadron from whence it came. This balance is not expected in the case of DPS or pileup. The scalar difference in p_{T} between the Z and the J/ψ is shown in Figure 8.3. Additionally, the Z in associated production is expected to be harder than the Z in inclusive or DPS production. The Z p_{T} distributions for associated production and inclusive production are shown in Figure 8.4. Although the statistical uncertainty is large, there is probably both SPS and DPS in our measurement.

8.3 Comparison with ATLAS

ATLAS [6] recently published the result of an analysis similar to the measurement we make. Their results are shown in Table 3 of Ref. [6], and their selection criteria are in Table 1, Namely, ATLAS observed 16.15 million Z $\to \ell\ell$ events, of which 8.20 million were Z $\to \mu^+\mu^-$ and 7.95 million were Z $\to$ e$^+$e$^-$. ATLAS selected in total 290 candidate signal events, of which 139 are observed with $Z \to \mu^+\mu^-$ decays and 151 with $Z \to e^+e^-$ decays. ATLAS presents their results with the Z $\to \mu^+\mu^-$ and Z $\to$ e$^+$e$^-$ channels combined. In comparison, with our selection we select a total of 11.6 million Z $\to \ell\ell$ events, of which 6.9 million were Z $\to \mu^+\mu^-$ and 4.6 million were Z $\to$ e$^+$e$^-$. We select 109 candidate signal events, of which 70 are observed with Z $\to \mu^+\mu^-$ and 39

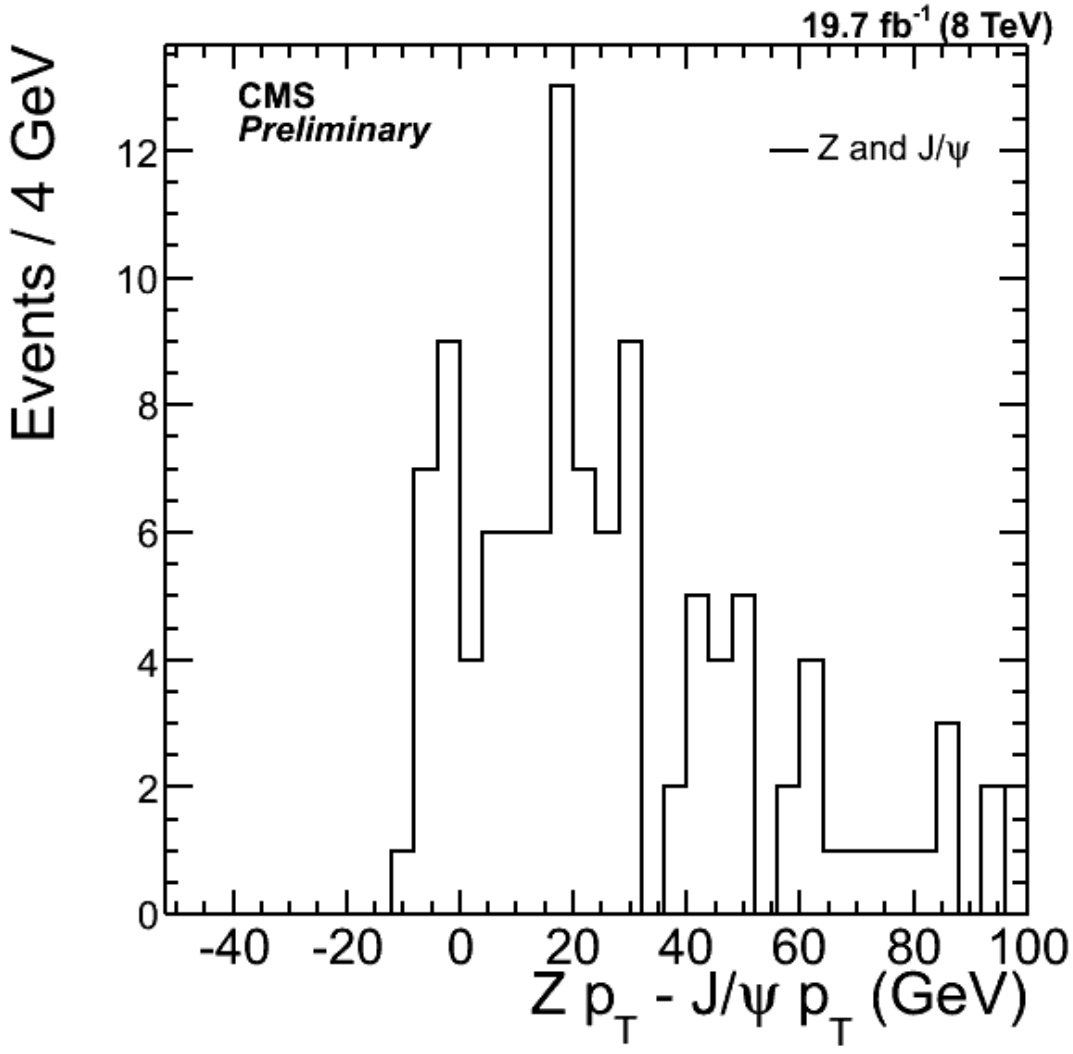

Figure 8.3: The difference between Z and J/ψ p_{T}. The SPS will on average have a more balanced p_{T} between the Z and J/ψ than the DPS.

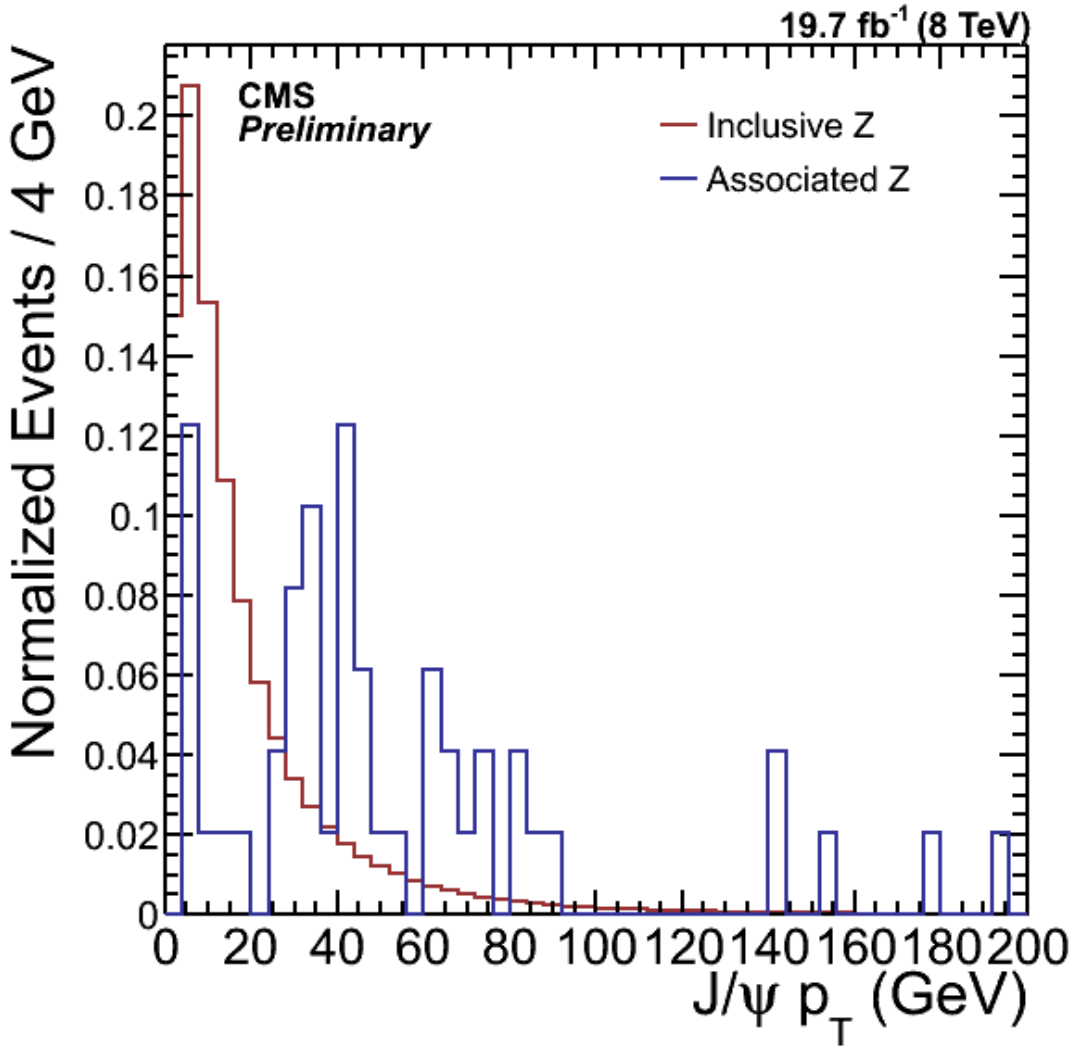

Figure 8.4: Associated and inclusive Z p_{T} distributions. A tighter selection criteria of J/ψ mass between 3.0 and 3.2 GeV and $|t_{xy}| \leq 0.3ps$ was applied to select out more prompt J/ψ. However, of the 50 events which pass all selection criteria, from the two-dimensional fit we expect only about 20 prompt J/ψ events. For associated SPS the rate of Z production with p_{T} below 5 GeV is very small [75].

Table 8.6: Rates ($\times 10^{-7}$) for p p $\to$Z $\to \ell\ \ell$ + J/$\psi \to \mu^+\mu^-$ relative to p p $\to$Z $\to \ell\ \ell$ both prompt and nonprompt for events with $|\Delta\phi| < \pi/3$. The amount of expected pileup is subtracted from the event yield when determining the rate, so the measured rate can be negative. The rate of DPS is determined with $\sigma_{eff} = 20.7\,\text{mb}$.

	Prompt $R_{J/\psi} \times 10^7$		Nonprompt $R_{J/\psi} \times 10^7$	
$p_T^{J/\psi}$ GeV	CMS	DPS	CMS	DPS
8.5-10	4.2±5.8	1.9±0.6	5.5 ± 6.0	0.8 ± 0.3
10-14	3.2±3.1	1.4±0.5	6.7 ± 4.4	0.8 ± 0.3
14-18	0.5±2.4	0.3±0.1	7.8 ± 3.7	0.3 ± 0.1
18-30	-0.04±0.05	0.1±0.04	-0.05 ± 0.06	0.1 ± 0.05
30-100	0±0	0.012±0.004	0 ± 0	0.02 ± 0.01
total	7.9±7.0	3.7±1.2	20.0 ± 8.3	2.1 ± 0.5

were observed with Z $\to e^+e^-$.

A comparison between CMS results and ATLAS results is shown in Table 8.7. ATLAS results were obtained from Table 5 of Ref. [6]. When integrated over J/ψ p_T, our results are in agreement within uncertainty of ATLAS's results.

8.4 Statistical Significance

I determine the statistical significance of our measurement by comparing the likelihood of the results I measured under the hypothesis of signal and background to the likelihood of the results under the background only hypothesis. Wilks' theorem provides a simple way to determine the significance from the difference in likelihood between the signal and background hypothesis and the signal only hypothesis [76]. From Wilks' theorem the distribution of the likelihood ratio test statistic follows the χ^2 distribution:

$$\chi^2 = 2[\ln \mathcal{L}(S+B) - \ln \mathcal{L}(B)] \tag{8.1}$$

where $\ln \mathcal{L}(S+B)$ is the likelihood of the signal plus background hypothesis and $\ln \mathcal{L}(B)$ is the likelihood of the background only hypothesis

I determine the likelihood of the data when fixing the amount of prompt (or nonprompt) signal to the amount expected from pileup and then repeating the fit procedure. The statistical significance of the observed data does not depend on the efficiency of the

Table 8.7: Comparison of signal between CMS and ATLAS [6]. In the 5 p_{T} regions, the results are differential rate, dR/dp_{T} in $\times 10^{-7}$/ GeV while the last line is the integral, $R(8.5\,\mathrm{GeV} < p_{\mathrm{T}} < 100\,\mathrm{GeV})$ in $\times 10^{-7}$. The first uncertainty is the statistical, the 2nd, combined systematic and the last, systematic uncertainty due to the unknown polarization of the J/ψ. The polarization uncertainty is common between the two experiments and can be ignored in the comparison.

Prompt Prob(Z + J/$\psi \to \mu^+\mu^-$|Z)

p_{T} range (GeV)	CMS	ATLAS
$8.5 < p_{\mathrm{T}} < 10$	$10.4 \pm 6.1 \pm 0.5 \pm 3.1$	$10.8 \pm 5.6 \pm 1.9 \pm 3.1$
$10 < p_{\mathrm{T}} < 14$	$4.9 \pm 1.9 \pm 0.2 \pm 1.3$	$5.6 \pm 1.9 \pm 0.8 \pm 1.2$
$14 < p_{\mathrm{T}} < 18$	$0.2 \pm 1.4 \pm 0.01 \pm 0.03$	$1.9 \pm 1.1 \pm 0.1 \pm 0.3$
$18 < p_{\mathrm{T}} < 30$	$0.22 \pm 0.3 \pm 0.011 \pm 0.04$	$0.9 \pm 0.4 \pm 0.12 \pm 0.09$
$30 < p_{\mathrm{T}} < 100$	$0.038 \pm 0.039 \pm 0.004 \pm 0.005$	$0.09 \pm 0.04 \pm 0.012 \pm 0.006$
Integrated	$41.5 \pm 12.0 \pm 1.8 \pm 10.5$	$63 \pm 13 \pm 5 \pm 10$

Nonprompt Prob(Z + J/$\psi \to \mu^+\mu^-$|Z)

p_{T} range (GeV)	CMS	ATLAS
$8.5 < p_{\mathrm{T}} < 10$	$14.8 \pm 7.4 \pm 0.6 \pm 0.4$	$5.1 \pm 4.2 \pm 0.9 \pm 0.3$
$10 < p_{\mathrm{T}} < 14$	$6.4 \pm 2.4 \pm 0.2 \pm 0.16$	$9.2 \pm 2.5 \pm 1.2 \pm 0.3$
$14 < p_{\mathrm{T}} < 18$	$4.6 \pm 1.7 \pm 0.1 \pm 0.1$	$3.3 \pm 1.2 \pm 0.4 \pm 0.1$
$18 < p_{\mathrm{T}} < 30$	$2.1 \pm 0.6 \pm 0.1 \pm 0.04$	$3.0 \pm 0.6 \pm 0.04 \pm 0.04$
$30 < p_{\mathrm{T}} < 100$	$0.029 \pm 0.043 \pm 0.003 \pm 0.0004$	$0.12 \pm 0.04 \pm 0.002 \pm 0.001$
Integrated	$93.0 \pm 14.5 \pm 2.5 \pm 2.0$	$102 \pm 15 \pm 5 \pm 3$

J/ψ (or the efficiency of the Z), so the fit is not weighted by the efficiency. In the signal and background scenario, there are 21.6 ± 6.6 prompt events and 52.7 ± 8.6 nonprompt events. Of these events, 1.1 prompt events are expected to come from pileup, and 1.7 nonprompt events are expected to come from pileup, as determined in Section 6.1. Figure 8.6 and Figure 8.7 show the results of the fit performed with the alternative hypothesis of background and prompt (nonprompt) signal fixed to the amount of expected pileup. Using the likelihood ratio test statistic I find that the statistical significance of observing the combination of SPS and DPS prompt J/ψ is 3.8σ and of nonprompt J/ψ is 8.7σ. This is similar to the significance claimed in [6], although ATLAS observed enough prompt signal to claim 5σ significance for prompt and 9σ significance for nonprompt associated production.

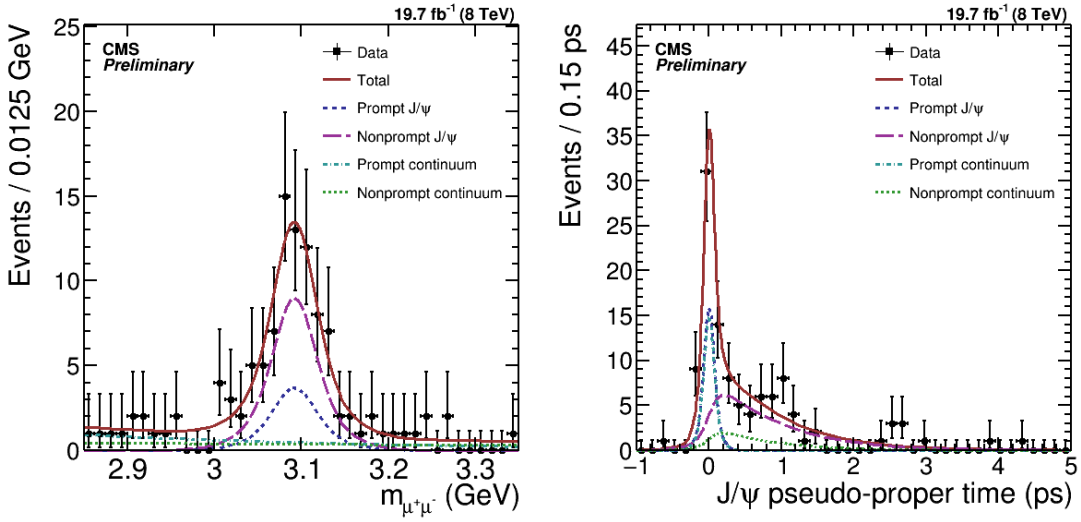

Figure 8.5: Associated production of a Z and a J/ψ, for $Z \to \ell\ell$.

I evaluate the significance of SPS events under different assumptions about the DPS cross section, as shown in Table 8.8. The rate of DPS has a large impact on the statistical significance of our results, and on the rate of SPS associated production.

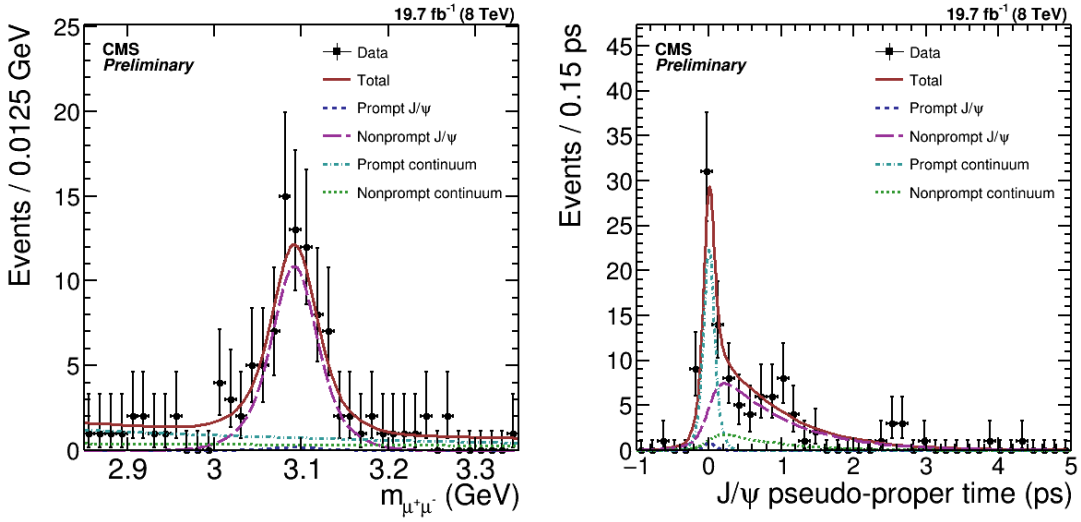

Figure 8.6: Associated production of a Z and a J/ψ, for Z $\to \ell\ell$. The prompt J/ψ signal is fixed to the expectation from pileup.

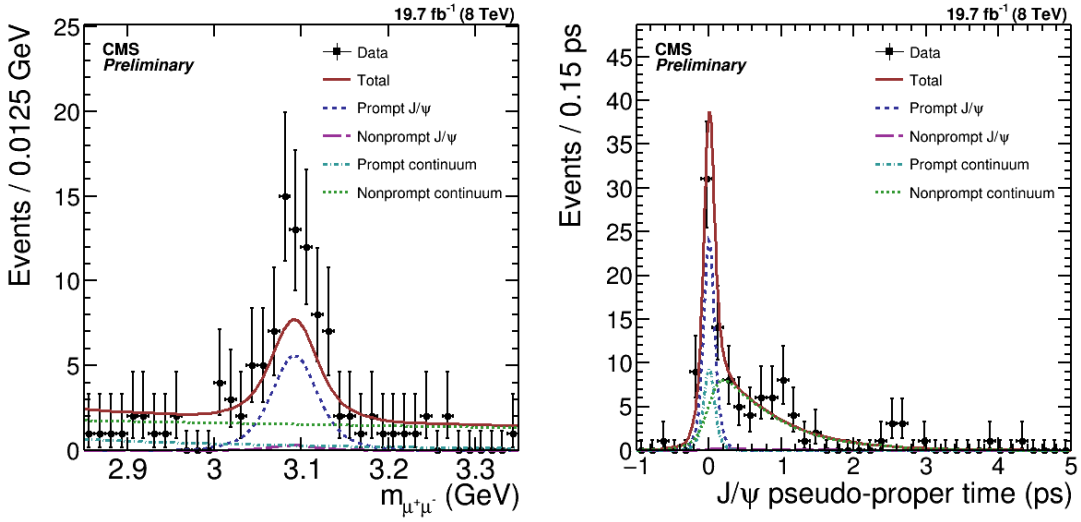

Figure 8.7: Associated production of a Z and a J/ψ, for Z $\to \ell\ell$. The nonprompt J/ψ signal is fixed to the expectation from pileup.

Table 8.8: The SPS significance for associated prompt J/ψ under different assumptions about DPS.

DPS σ_{eff} mb	SPS Significance
20.7	2.9
15	2.6
10	2.1
5	0.6

Chapter 9

Conclusions

I measured the rate of associated production of a Z $\to \ell\ \ell$ and a J/ψ $\to \mu^+\mu^-$ relative to the rate of inclusive production of a Z $\to \ell\ \ell$ using the full 19.7 fb^{-1} of proton-proton collisions recorded with the CMS detector at a center-of-mass energy of 8 TeV. This rate was measured both for prompt and nonprompt J/ψ, and presented in 5 bins of J/ψ p_{T}, as well as integrated over a J/ψ p_{T} between 8.5 GeV and 100 GeV. I observed the production of associated prompt J/ψ, including both SPS and DPS, with a statistical significance of 3.8σ and nonprompt J/ψ with a statistical significance of 8.7σ. The measured rate of associated nonprompt J/ψ was statistically compatible with the measurement made by the ATLAS experiment. Although there is currently no quantitative theoretical prediction for this process, theorists are currently attempting to make these predictions. The measured rate of nonprompt associated production was in reasonable agreement with the rate predicted from MC.

The measured rate of prompt J/ψ production was higher than the theoretical expectation by a factor of about 3. The ATLAS experiment measured a rate of associated prompt J/ψ about a factor of 5 higher than theoretically expected, and statistically compatible with our measurement. These results suggest that certain theoretical assumptions may not be justified, for example the assumption that the rate of DPS is process independent, or the assumption that higher-order terms are not important in the NRQCD calculation. However, the statistical uncertainties and the polarization uncertainty are large, so more data is needed to conclusively understand this process. The LHC is currently collecting a large amount of data at 13 TeV, so this process can

be studied with higher statistics in the near future.

References

[1] Baseline muon selections for run-1. `https://twiki.cern.ch/twiki/bin/view/CMSPublic/SWGuideMuonId`. Accessed: 2016-08-11.

[2] L. K Saini, I Kravchenko, and Y. Maravin. A study of efficiencies and scale factors for cut-based electron identification at CMS experiment using data from proton-proton collisions at $\sqrt{s} = 8$ tev. CMS Note 2014/055, 2014.

[3] Serguei Chatrchyan et al. Study of double parton scattering using W + 2-jet events in proton-proton collisions at $\sqrt{s} = 7$ TeV. *JHEP*, 1403:032, 2014, 1312.5729.

[4] S. Mao, M. Ma, Wen-Gan, L. Gang, Z. Ren-You, and G. Lei. QCD corrections to J/ψ plus Z0-boson production at the LHC. *JHEP*, 1102:071, 2011.

[5] Song Mao, Ma Wen-Gan, Li Gang, Zhang Ren-You, and Guo Lei. Erratum: Qcd corrections to j/ψ plus z0-boson production at the lhc. *Journal of High Energy Physics*, 2012(12):1–2, 2012.

[6] Georges Aad et al. Observation and measurements of the production of prompt and non-prompt J/ψ mesons in association with a Z boson in pp collisions at $\sqrt{s}$ = 8 TeV with the ATLAS detector. *Eur.Phys.J.*, C75(5):229, 2015, 1412.6428.

[7] Michael Kramer, 1. J/ψ and psi_{2S} production and polarization at the Tevatron. *Nucl. Phys. Proc. Suppl.*, 93:176–181, 2001, hep-ph/0010137. [,176(2000)].

[8] N. Brambilla et al. Heavy quarkonium: progress, puzzles, and opportunities. *Eur. Phys. J.*, C71:1534, 2011, 1010.5827.

[9] J. F. Amundson, Oscar J. P. Eboli, E. M. Gregores, and F. Halzen. Quantitative tests of color evaporation: Charmonium production. *Phys. Lett.*, B390:323–328, 1997, hep-ph/9605295.

[10] Cheuk-Yin Wong. The soft gluon emission process in the color octet model for heavy quarkonium production. *Phys. Rev.*, D60:114025, 1999, hep-ph/9906291.

[11] Bin Gong, Lu-Ping Wan, Jian-Xiong Wang, and Hong-Fei Zhang. Polarization for Prompt J/ψ and $\psi(2s)$ Production at the Tevatron and LHC. *Phys. Rev. Lett.*, 110(4):042002, 2013, 1205.6682.

[12] Serguei Chatrchyan et al. Measurement of the prompt J/ψ and ψ(2S) polarizations in pp collisions at $\sqrt{s} = 7$ TeV. *Phys. Lett.*, B727:381–402, 2013, 1307.6070.

[13] T. Alexopoulos and S. Leontsinis. Estimates of Z Boson and J/ψ Production Cross Sections At the Large Hadron Collider. *JETP*, 147 (5):937, 2015.

[14] Cern accelerator complex. `http://www.lhc-closer.es/taking_a_closer_look_at_lhc/0.cern_accelerator_complex`. Accessed: 2016-08-06.

[15] CMS collaboration et al. Energy calibration and resolution of the cms electromagnetic calorimeter in pp collisions at sqrt (s)= 7 tev. *arXiv preprint arXiv:1306.2016*, 2013.

[16] Vardan Khachatryan et al. Performance of Electron Reconstruction and Selection with the CMS Detector in Proton-Proton Collisions at sqrt(s) = 8 TeV. *JINST*, 10(06):P06005, 2015, 1502.02701.

[17] *The CMS electromagnetic calorimeter project: Technical Design Report.* Technical Design Report CMS. CERN, Geneva, 1997. `http://cds.cern.ch/record/349375`.

[18] Georges Aad et al. Measurement of the differential cross-sections of inclusive, prompt and non-prompt J/ψ production in proton-proton collisions at $\sqrt{s} = 7$ TeV. *Nucl.Phys.*, B850:387, 2011, 1104.3038.

[19] Georges Aad et al. Measurement of hard double-parton interactions in $W(\rightarrow l\nu)+$ 2 jet events at $\sqrt{s}$=7 TeV with the ATLAS detector. *New J. Phys.*, 15:033038, 2013, 1301.6872.

[20] J. Alitti et al. A Study of multi - jet events at the CERN anti-p p collider and a search for double parton scattering. *Phys. Lett.*, B268:145–154, 1991.

[21] Jonathan R. Gaunt, Chun-Hay Kom, Anna Kulesza, and W. James Stirling. Same-sign W pair production as a probe of double parton scattering at the LHC. *Eur. Phys. J.*, C69:53–65, 2010, 1003.3953.

[22] F. Abe et al. Study of four-jet events and evidence for double parton interactions in $p\overline{p}$ collisions at $\sqrt{s} = 1.8$ tev. *Phys. Rev. D*, 47:4857–4871, Jun 1993.

[23] F. Abe et al. Double parton scattering in $\overline{p}p$ collisions at $\sqrt{s} = 1.8$TeV. *Phys. Rev. D*, 56:3811–3832, Oct 1997.

[24] V. M. Abazov et al. Double parton interactions in $\gamma + 3$ jet events in $p\overline{p}$ collisions at $\sqrt{s} = 1.96$ TeV. *Phys. Rev. D*, 81:052012, Mar 2010.

[25] Steven Weinberg. A model of leptons. *Phys. Rev. Lett.*, 19:1264–1266, Nov 1967.

[26] Serguei Chatrchyan et al. Observation of a new boson at a mass of 125 GeV with the CMS experiment at the LHC. *Phys. Lett.*, B716:30–61, 2012, 1207.7235.

[27] CDF Collaboration. Observation of top quark production in $\overline{p}p$ collisions with the collider detector at fermilab. *Phys. Rev. Lett.*, 74:2626–2631, Apr 1995.

[28] G. Arnison et al. Experimental Observation of Events with Large Missing Transverse Energy Accompanied by a Jet Or a Photon(s) in p anti-p Collisions at s**(1/2)=540-GeV. *Phys. Lett.*, B139:115, 1984.

[29] Stephen P. Martin. A Supersymmetry primer. 1997, hep-ph/9709356. [Adv. Ser. Direct. High Energy Phys.18,1(1998)].

[30] Y. Fukuda et al. Evidence for oscillation of atmospheric neutrinos. *Phys. Rev. Lett.*, 81:1562–1567, 1998, hep-ex/9807003.

[31] John C. Baez and John Huerta. The Algebra of Grand Unified Theories. *Bull. Am. Math. Soc.*, 47:483–552, 2010, 0904.1556.

[32] W. Buchmuller and C. Ludeling. Field Theory and Standard Model. In *High-energy physics. Proceedings, European School, Kitzbuehel, Austria, August 21-September, 2005*, 2006, hep-ph/0609174.

[33] Guido ALTARELLI. The Standard model of particle physics. 2005, hep-ph/0510281.

[34] N. Brambilla et al. QCD and Strongly Coupled Gauge Theories: Challenges and Perspectives. *Eur. Phys. J.*, C74(10):2981, 2014, 1404.3723.

[35] Nora Brambilla, Antonio Pineda, Joan Soto, and Antonio Vairo. Potential NRQCD: An Effective theory for heavy quarkonium. *Nucl. Phys.*, B566:275, 2000, hep-ph/9907240.

[36] Peter Skands. Introduction to QCD. In *Proceedings, Theoretical Advanced Study Institute in Elementary Particle Physics: Searching for New Physics at Small and Large Scales (TASI 2012): Boulder, Colorado, June 4-29, 2012*, pages 341–420, 2013, 1207.2389.

[37] G. M. Prosperi, M. Raciti, and C. Simolo. On the running coupling constant in QCD. *Prog. Part. Nucl. Phys.*, 58:387–438, 2007, hep-ph/0607209.

[38] Rajan Gupta. Introduction to lattice QCD: Course. In *Probing the standard model of particle interactions. Proceedings, Summer School in Theoretical Physics, NATO Advanced Study Institute, 68th session, Les Houches, France, July 28-September 5, 1997. Pt. 1, 2*, pages 83–219, 1997, hep-lat/9807028.

[39] Thomas Schäfer. Phases of QCD. In *20th Annual Hampton University Graduate Studies Program (HUGS 2005) Newport News, Virginia, May 31-June 17, 2005*, 2005, hep-ph/0509068.

[40] John C. Collins, Davison E. Soper, and George F. Sterman. Factorization of Hard Processes in QCD. *Adv. Ser. Direct. High Energy Phys.*, 5:1–91, 1989, hep-ph/0409313.

[41] Vardan Khachatryan et al. Measurement of the inclusive 3-jet production differential cross section in proton–proton collisions at 7 TeV and determination of

the strong coupling constant in the TeV range. *Eur. Phys. J.*, C75(5):186, 2015, 1412.1633.

[42] K. A. Olive et al. Review of Particle Physics. *Chin. Phys.*, C38:090001, 2014.

[43] Geoffrey T. Bodwin. NRQCD Factorization and Quarkonium Production at Hadron-Hadron and ep Colliders. *Int. J. Mod. Phys. Conf. Ser.*, 02:9–14, 2011, 1012.4215.

[44] J. P. Lansberg and C. Lorce. Reassessing the importance of the colour-singlet contributions to direct $J/\psi + W$ production at the LHC and the Tevatron. *Phys. Lett.*, B726:218–222, 2013, 1303.5327. [Erratum: Phys. Lett.B738,529(2014)].

[45] Geoffrey T. Bodwin, Eric Braaten, and Jungil Lee. Comparison of the color-evaporation model and the NRQCD factorization approach in charmonium production. *Phys. Rev.*, D72:014004, 2005, hep-ph/0504014.

[46] B. Gong, J.-P. Lansberg, C. Lorce, and Wang J. Next-to-leading-order QCD corrections to the yields and polarisations of J/ψ and Y directly produced in association with a Z boson at the LHC. *JHEP*, 1303:115, 2013.

[47] Georges Aad et al. Measurement of the production cross section of prompt J/ψ mesons in association with a $W^{\pm}$ boson in pp collisions at $\sqrt{s} = 7$ TeV with the ATLAS detector. *JHEP*, 04:172, 2014, 1401.2831.

[48] CERN. The accelerator complex, 2015 (Online; accessed 8-December-2015). `http://home.cern/about/accelerators`.

[49] S. Chatrchyan et al. The CMS experiment at the CERN LHC. *JINST*, 3:S08004, 2008.

[50] Serguei Chatrchyan et al. Description and performance of track and primary-vertex reconstruction with the CMS tracker. *JINST*, 9(10):P10009, 2014, 1405.6569.

[51] Serguei Chatrchyan et al. Energy Calibration and Resolution of the CMS Electromagnetic Calorimeter in pp Collisions at $\sqrt{s} = 7$ TeV. *JINST*, 8:P09009, 2013, 1306.2016. [JINST8,9009(2013)].

[52] D A Petyt and the CMS collaboration). Mitigation of anomalous apd signals in the cms electromagnetic calorimeter. *Journal of Physics: Conference Series*, 404(1):012043, 2012.

[53] Electromagnetic calorimeter commissioning and first results with 7 TeV data. Technical Report CMS-NOTE-2010-012, CERN, Geneva, Jul 2010.

[54] Serguei Chatrchyan et al. Performance of CMS muon reconstruction in pp collision events at $\sqrt{s} = 7$ tev. *JINST*, 7:P10002, 2012, 1206.4071.

[55] J. Brooke. Performance of the CMS Level-1 Trigger. *PoS*, ICHEP2012:508, 2013, 1302.2469.

[56] W. Adam et al. The CMS high level trigger. *Eur. Phys. J.*, C46:605–667, 2006, hep-ex/0512077.

[57] CMS Luminosity Based on Pixel Cluster Counting - Summer 2013 Update. Technical Report CMS-PAS-LUM-13-001, CERN, Geneva, 2013.

[58] Vardan Khachatryan et al. Performance of Photon Reconstruction and Identification with the CMS Detector in Proton-Proton Collisions at sqrt(s) = 8 TeV. *JINST*, 10(08):P08010, 2015, 1502.02702.

[59] Alexander Gude. Measurement of the phistar distribution of z bosons decaying to electron pairs with the cms experiment at a center-of-mass energy of 8 tev. `http://hdl.handle.net/11299/175445`, 2015.

[60] Final tracks selector algorithms. `https://twiki.cern.ch/twiki/bin/view/CMSPublic/SWGuideFinalTrackSelectors`. Accessed: 2016-08-30.

[61] Johan Alwall, Michel Herquet, Fabio Maltoni, Olivier Mattelaer, and Tim Stelzer. MadGraph 5 : Going Beyond. *JHEP*, 06:128, 2011, 1106.0522.

[62] CMS Collaboration. Muon ID performance: low-p_{T} muon efficiencies. CMS Note 2014/020, 2014.

[63] Measuring Electron Efficiencies at CMS with Early Data. 2008.

[64] Roger Barlow. Extended maximum likelihood. *Nuclear Instruments and Methods in Physics Research Section A: Accelerators, Spectrometers, Detectors and Associated Equipment*, 297(3):496–506, 1990.

[65] G. Antchev et al. Luminosity-independent measurement of the proton-proton total cross section at $\sqrt{s} = 8$ TeV. *Phys. Rev. Lett.*, 111:012001, Jul 2013.

[66] T. Sjostrand and Peter Z. Skands. Multiple interactions and the structure of beam remnants. *JHEP*, 03:053, 2004, hep-ph/0402078.

[67] V. M. Abazov et al. Observation and studies of double j/ψ production at the tevatron. *Phys. Rev. D*, 90:111101, Dec 2014.

[68] V. M. Abazov et al. Evidence for simultaneous production of j/ψ and Υ mesons. *Phys. Rev. Lett.*, 116:082002, Feb 2016.

[69] Georges Aad et al. Measurement of the differential cross-sections of prompt and non-prompt production of J/ψ and ψ(2S) in pp collisions at $\sqrt{s} = 7$ and 8 TeV with the ATLAS detector. 2015, 1512.03657.

[70] F. Bossu, Z. Conesa del Valle, A. de Falco, M. Gagliardi, S. Grigoryan, and M. Garcia. Phenomenological interpolation of the inclusive j/ψ cross section to proton-proton collisions at 2.76 tev and 5.5 tev. 2011, 1103.2394.

[71] A. Abulencia et al. Polarization of J/ψ and ψ_{2S} mesons produced in $p\bar{p}$ collisions at $\sqrt{s} = 1.96$-TeV. *Phys. Rev. Lett.*, 99:132001, 2007, 0704.0638.

[72] Tag and probe. `https://twiki.cern.ch/twiki/bin/view/CMS/MuonTagAndProbe`. Accessed: 2016-08-06.

[73] S. Mao, M. Ma, Wen-Gan, L. Gang, Z. Ren-You, and G. Lei. Private communication. these numbers were calculated by the authors of ref. [4, 5] for the specific selection criteria listed in table 8.4. 2015.

[74] Serguei Chatrchyan et al. Measurement of inclusive W and Z boson production cross sections in pp collisions at $\sqrt{s} = 8$ TeV. *Phys. Rev. Lett.*, 112:191802, 2014, 1402.0923.

[75] Jean-Philippe Lansberg and Hua-Sheng Shao. Associated production of a quarkonium and a Z boson at one loop in a quark-hadron-duality approach. 2016, 1608.03198.

[76] Jianqing Fan, Chunming Zhang, and Jian Zhang. Generalized likelihood ratio statistics and wilks phenomenon. *Ann. Statist.*, 29(1):153–193, 02 2001.